GA-A22816
UC-712

INERTIAL CONFINEMENT FUSION TARGET COMPONENT FABRICATION AND TECHNOLOGY DEVELOPMENT SUPPORT

ANNUAL REPORT TO THE U.S. DEPARTMENT OF ENERGY

OCTOBER 1, 1996 THROUGH SEPTEMBER 30, 1997

by
PROJECT STAFF
Jane Gibson, Editor

Work prepared under
Department of Energy
Contract No. DE-AC03-95SF20732

GENERAL ATOMICS PROJECT 3748
DATE PUBLISHED: MARCH 1998

GENERAL ATOMICS

DISCLAIMER

Portions of this document may be illegible electronic image products. Images are produced from the best available original document.

The FY1997 Target Fabrication and Target Technology Development Team

General Atomics
San Diego, California

Neil Alexander, Wes Baugh, Chuck Beal, Gary Bentley, Dave Bernat, Gottfried Besenbruch, Karl Boline, Lloyd Brown, Sharon Considine, Don Czechowicz, Walt Egli, Fred Elsner, Chuck Gibson, Jane Gibson, Kett Gifford, Dan Goodin, Steve Grant, Annette Greenwood, Eric Hoffman, Martin Hoppe, Dave Husband, Jim Kaae, Barry McQuillan, Wayne Miller, Abbas Nikroo, Joe Pontelandolfo, John Ruppe, Chuck Schneidmuller, Ken Schultz, Clyde Shearer, John Sheliak, Joe Smith, Rich Stephens, Dave Steinman, Bob Stemke, John Vanderzanden, Don Wall, Jason Wall, David Woodhouse.

Schafer Corporation
Livermore, California

Tom Alberts, Thom Bahrs, Don Bittner, John Burmann, Frank Carey, Derrick Coker, Steve Dropinski, Illges Faron, Scott Faulk, Chuck Hendricks, Ephraim Hipolito, Derek Mathews, Michael McClellan, Eric Monsler, Michael Monsler, Brian Motta, Craig Rivers, Jim Sater, Diana Schroen-Carey, Keith Shillito, Cheryl Spencer, Katie Strube,Tom Walsh.

ABSTRACT

On December 30, 1990, the U.S. Department of Energy entered into a contract with General Atomics (GA) to be the Inertial Confinement Fusion (ICF) Target Component Fabrication and Technology Development Support contractor. In September 1995 this contract ended and a second contract was issued for us to continue this ICF target support work. This report documents the technical activities of the period October 1, 1996 through September 30, 1997. During this period, GA and our partner Schafer Corporation were assigned 13 formal tasks in support of the ICF program and its five laboratories. A portion of the effort on these tasks included providing direct "Onsite Support" at Lawrence Livermore National Laboratory (LLNL), Los Alamos National Laboratory (LANL), and Sandia National Laboratory Albuquerque (SNLA). We fabricated and delivered over 700 gold-plated hohlraum mandrels to LLNL, LANL and SNLA. We produced more than 1,600 glass and plastic target capsules for LLNL, LANL, SNLA and University of Rochester/Laboratory for Laser Energetics (UR/LLE). We also delivered nearly 2000 various target foils and films for Naval Research Lab (NRL) and UR/LLE in FY97. This report describes these target fabrication activities and the target fabrication and characterization development activities that made the deliveries possible.

The ICF program is anticipating experiments at the OMEGA laser and the National Ignition Facility (NIF) which will require targets containing cryogenic layered D_2 or deuterium-tritium (DT) fuel. We are part of the National Cryogenic Target Program and support experiments at LLNL and LANL to generate and characterize cryogenic layers for these targets.

During FY97, significant progress was made in the design and component testing of the OMEGA Cryogenic Target System that will field cryogenic targets on OMEGA. This included major design changes, reduction in equipment, and process simplifications.

This report summarizes and documents the technical progress made on these tasks.

TABLE OF CONTENTS

LIST OF FIGURES

LIST OF TABLES

1. TARGET FABRICATION PROGRAM OVERVIEW

On December 30, 1990, the U.S. Department of Energy entered into a contract with General Atomics (GA) to be the Inertial Confinement Fusion (ICF) Target Component Fabrication and Technology Development Support contractor. In September 1995 this contract ended and a second contract was issued for us to continue this ICF target support work. This report documents the technical activities of the period October 1, 1996 through September 30, 1997. GA was assisted by Schafer Corporation and we have carried out the ICF Target Fabrication tasks as a fully integrated team effort.

During FY97, the GA/Schafer team was assigned 13 formal tasks, as shown in Table 1-1. These tasks are described briefly here (Section 1). Additional technical detail on selected topics is given in Sections 2 through 6 of this report.

TABLE 1-1
FY97 TARGET FABRICATION TASKS

Task No.	Task Title Description	Total $K	Task Leader
LL01	On-Site Support for LLNL	616	Miller/Shillito
LL02	Micromachined Target Components	1,142	Kaae
LL03	Composite Polymer Capsules for LLNL	647	Miller
LA01	On-Site Support for LANL	330	Shillito
LA02	Composite Polymer Capsules	600	Miller
NR01	NRL Target Development and Deliveries	795	Hendricks
SL01	Fabrication of Targets for SNL	1,028	Kaae/Schroen-Cary
UR01	Polymer Capsules for LLE	1,210	Miller
UR02	Shell Characterization Development	114	Stephens
UR03	Flat Foils	200	Hendricks
CR/LL1	Cryogenic Target Fielding Development	440	Sater/Bittner
CR/LA1	Beta Layering Support at LANL	225	Sheliak
CR/UR1	OMEGA Target Systems Engineering	4,046	Besenbruch
	Total	11,393	

1.1. LL01 ON-SITE SUPPORT FOR LLNL

Our on-site team at Lawrence Livermore Laboratory (LLNL) was composed of Derek Coker, Derrick Mathews, Craig Rivers, and John Ruppe and Diana Schroen-Carey (part-time). They provided support in micromachining of target components, assembling target components into complete targets, and characterizing target components and capsules for use in NOVA and OMEGA ICF experiments.

1.2. LL02 MICROMACHINED TARGET COMPONENTS

In FY97, this task was divided between LLNL and Los Alamos National Laboratory (LANL) although the major effort was directed toward production of components for LLNL.

For LLNL the effort was to:

1. Produce precision machined mandrels for use as coating substrates.
2. Produce precision machined target components.
3. Provide supporting technologies such as electroplating, PVD, sub-component assembly, characterization and metrology.
4. Supply production drawings and documentation.

In FY97, we responded to 55 separate requests from LLNL for:

1. 634 gold-plated copper hohlraum mandrels.
2. 113 profiled plates (sine wave plates, dimpled plates, top hat plates).
3. 83 aluminum witness plates.
4. 4 gold and silver plated copper cylinders.

For LANL, the effort was to:

1. Fabricate target components by micromachining.

In FY97, we responded to 6 separate requests from LANL for:

1. 110 gold-plated copper hohlraum mandrels.
2. 36 aluminum witness plates.

We responded to all of these requests promptly and produced components that met specification.

In the micromachining laboratory, the Precitech 2000 Lathe 1 (DOE-owned) and Lathe 2 (GA-owned) were operational over the FY97 period with only occasional down times of a few

days. The Rocky Flats No. 3 Lathe was upgraded with modern encoders and controllers, and was brought into production, operating with no down time.

The micromachining laboratory is being expanded to accommodate a new Precitech 2400 Lathe which has been ordered and is expected in December 1997.

In FY98 we intend to upgrade the air conditioning system for the laboratory to maintain better temperature control. Small temperature variations can produce dimensional drift in the micromachining lathes. At the present time, we correct for the drift by measuring the dimensions of every part produced, but often even this does not allow total compensation for the drift. Thus, better temperature control in the laboratory will be implemented.

1.3. LL03 / LA02 / UR01 / UR02 COMPOSITE POLYMER CAPSULES

Flexibility, productivity, and rapid response were the guiding principles for the capsule delivery tasks. This was especially true for polymer targets needed by UR/LLE for experiments on OMEGA. OMEGA targets consisted of up to four layers and could be doped with titanium, chlorine, germanium, or deuterium (Fig. 1-1). Frequently, a series of targets was required, each differing only slightly from the others (Fig. 1-2). At times, target requirements for one set of OMEGA experiments were not known until another series of experiments was completed and analyzed. Since the next series of experiments could be scheduled shortly after the first series, productivity and rapid response to target requests were critical. Usually target specifications were known only three to four weeks before delivery was required.

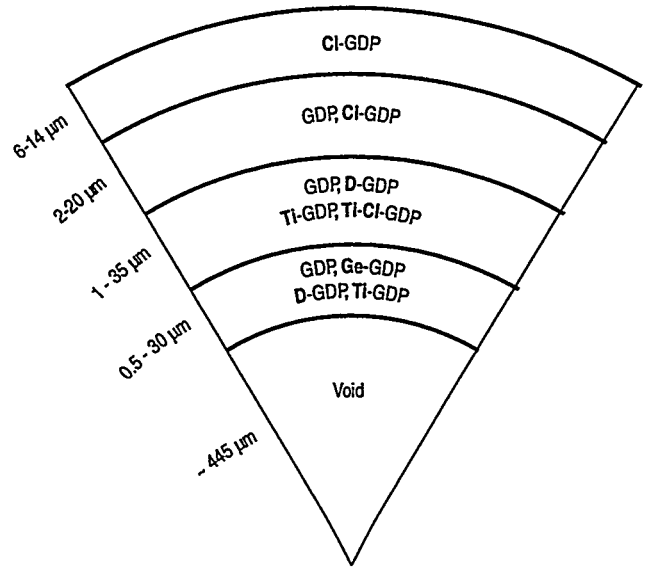

Fig. 1-1. Targets for UR/LLE experiments on OMEGA may have several layers, each layer differing from the others by the type of dopant and the layer thickness. The layer thicknesses shown are the range of thickness that were requested, not the tolerances, e.g., a specific request for the third layer thickness could be 9 ± 1 μm. The total wall thickness was typically 20 μm.

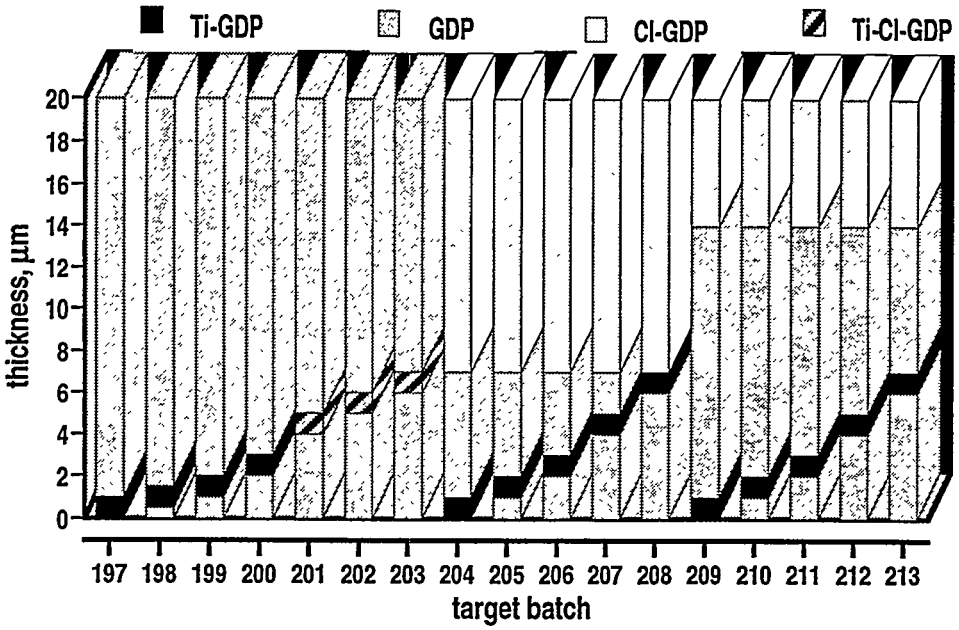

Fig. 1-2. This is a typical series of targets that differ slightly from one another for experiments on OMEGA. Although all have a total thickness of 20 μm, the targets differ by number of layers, layer thicknesses, and the dopants in each layer.

Glass shells were also required in several varieties (Fig. 1-3). The largest shells survived a burst test using helium to reduce the probability of breakage during a deuterium-tritium (DT) fill at LANL. The smallest shells, the ones with 23 μm walls, are a new development. Previously the thickest glass shells delivered in the program were about 11 μm. During the development of those shells we discovered ways to make shells with wall thicknesses of over 30 μm and suspect that even thicker walled shells are possible.

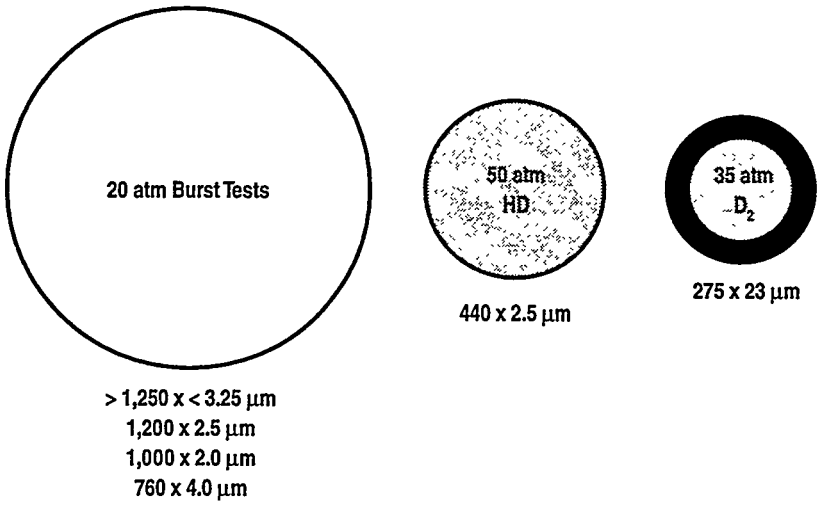

Fig. 1-3. Glass shells were delivered in several sizes. The largest shells were not filled, but survived a burst test at 20 atm. The smaller sizes were filled with HD or D_2. The shells with 23 μm walls are double the thickness of any previously requested glass shells.

Overall, many more capsules were delivered in FY97 than FY96 (Fig. 1-4). However, quantity is not the best measure of our effort. Effort is mostly affected by complexi intensive characterization — the key characteristics of each capsule were measured and reported. The remaining 1/3 consisted of large batches in which only a few capsules were characterized to provide an estimate of the average characteristics of the batch. Although the overall average batch size was about 20 capsules, the average is skewed by several very large batches. Most batches, and especially the ones with the most complex targets, consisted of seven or less.

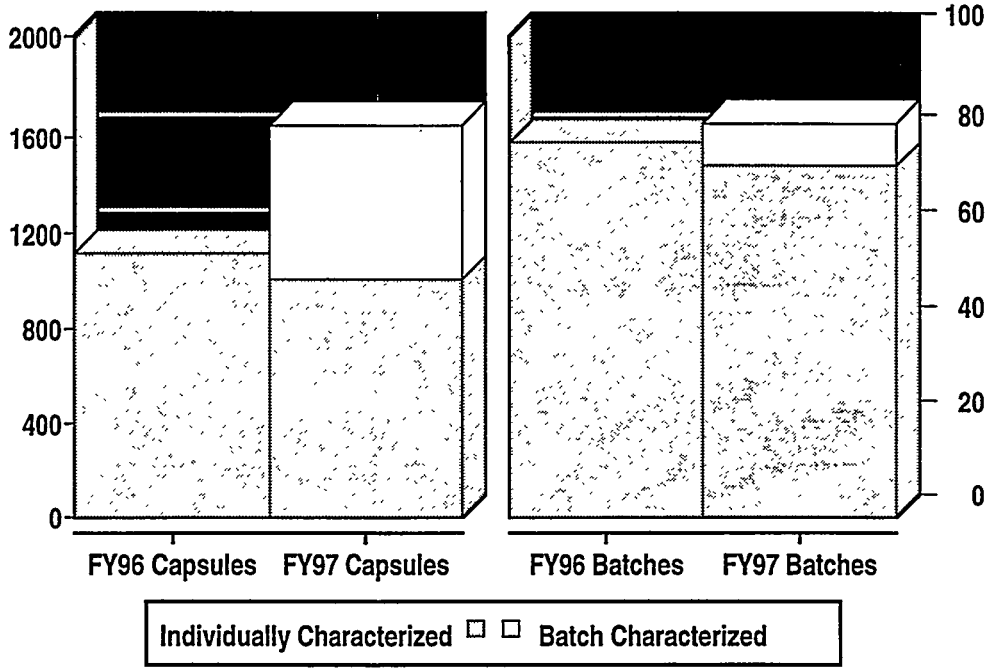

Fig. 1-4. More capsules were delivered in FY97 than FY96. The effort required to make a batch depends on whether every capsule is characterized and on the complexity of the targets. Most batches, and all with complex targets, consisted of seven or less.

Producing the capsules required for ICF experiments was our most important task and the one which required most of our efforts. However, improvements were made in several areas:

NOVA capsules were substantially improved when mandrels produced by glow discharge polymerization (GDP) replaced polystyrene mandrels.

OMEGA targets were improved when we discovered how to eliminate nearly all vacuoles in Poly(alpha-methylstyrene) (PAMS) mandrels.

We made progress in making 2 mm PAMS shells in preparation for the National Ignition Facility (NIF) targets.

The process for doping GDP with titanium was improved and was used for a substantial number of targets.

We found that using a spinning pan during the GDP deposition process allows coating a larger number of shells without degrading the surface finish.

For cryogenic layering experiments, a capsule is desired with a diameter over 1 mm that can hold over 100 atm DT at room temperature. We developed such a capsule by coating a glass shell with GDP.

In characterization, we improved the accuracy of diameter and layer thickness measurements as well as x–ray fluorescence (XRF) elemental determinations.

These developments are described in later sections.

1.4. LA01 ON-SITE SUPPORT FOR LANL

We provided two technicians to give on-site support for LANL under this task. At LLNL, Kett Gifford assembled and characterized numerous LANL targets, plus he provided some micromachining support to the target fabrication effort. At LANL, Steve Dropinski provided on-site support for target machining, assembly, and characterization of targets that were shot at NOVA, Trident, Particle Beam Fusion Accelerator-Z (PBFA-Z), and OMEGA. He also provided assistance during target campaigns at Sandia National Laboratory (SNL) and University of Rochester/Laboratory for Laser Energetics (UR/LLE) when required.

1.5. NR01/UR03 NIKE TARGET PRODUCTION AND OMEGA FLAT FILM DELIVERIES

The NR01 and UR03 tasks are related in that many of the techniques used to produce target foils for the NIKE laser program at Naval Research Lab (NRL) are directly applicable to the production of target films for the OMEGA laser program at LLE. Both programs require flat, smooth, polymeric material films as targets for the lasers. They also require films which are flat and have one smooth surface and have a specified pattern on the obverse surface. Many of the target foils are and may be layers of pure polymeric materials or may be composed of various doped polymers or layers of polymers and metals. The layers of materials are formed by several methods including evaporative deposition, liquid casting, precision machining, GDP, reactive chemistry, air brushing, and precision molding.

The quality specifications for both the NRL and LLE target films are dictated by the laser beam quality and diagnostics capabilities. Any random irregularities on the films should be less than any equivalent laser beam irregularities and must not introduce perturbations which will mask the diagnosis of the experiment. The general target film specifications and

limitations for the two tasks include film curvature, surface smoothness, material purity, and volume inclusions such as bubbles or particulates.

Many of the required targets for both LLE and NRL have deliberate surface perturbations. The patterns include randomly rough surfaces, sin(x) and sin(x) sin(y), and various stepped and ramped patterns. Most of the patterned surfaces are produced by casting the polymer films on a substrate whose surface has the pattern ion milled into a fused quartz blank. Other patterned surfaces are produced by precision machining the pattern into a thin film of polymer or metal.

Several types of multilayered targets are produced for the laser programs. We produce a target with circular symmetry for NRL which consists of a circular truncated conical aluminum base on which is mounted in succession, a layer of Kapton film, a layer of aluminum, a layer of low density foam, and finally, another layer of aluminum about 120 nanometers thick.

In the FY97 year, we have produced and delivered almost 2000 of the various target foils and films, some mounted on target frames and some as free-standing films, to both NRL and LLE.

1.6. SL01 FABRICATION OF TARGETS FOR SNL

In FY97 this task was divided into five subtasks: (1) on-site support; (2) fabrication of hohlraums, (3) fabrication of physics packages; (4) fabrication and machining of low-density foams; (5) fabrication of capsules and microshells.

On-site support was supplied by Tom Alberts who was assigned to SNL Albuquerque for the whole year. Tom led the effort in fabricating a variety of targets from components fabricated at GA and Schafer.

A total of 132 hohlraums of eight different kinds were fabricated to specifications supplied by SNL in the hohlraum subtask. These were relatively large hohlraums with diameters ranging up to 10 mm and lengths ranging up to 20 mm.

A total of 59 witness plates of 3 different kinds were fabricated in the physics package subtask. Two different witness-plate materials were employed: aluminum and polycarbonate. As with the hohlraums, the witness plates were relatively large with dimensions ranging up to 11 mm.

The foam subtask required the development of fabrication techniques for low-density foams which marked the beginning of a new production capability for the ICF contract. Sandia requested the production of low-density foams, 40 mg/cm^3 or less, fabricated into precision

geometries. There were three foam systems of interest, resorcinol-formaldehyde, polystyrene and TPX. (TPX is the registered trademark of the polymer produced from 4-methyl-1-pentene by Mitsui Petrochemical Industries, Ltd., Tokyo, Japan.) The exact geometries were obtained by either direct machining of the foam, or by molding the foam precursor. Twenty-two TPX foam cylinders 4 to 8 mm in diameter, 10 mm long with densities in the range 7 to 10 mg/cm^3 were produced and delivered. Also, 25 polystyrene foam annuli with outside diameters of 4 to 5 mm, wall thicknesses of about 0.5 mm and densities of 40 to 50 mg/cm^3 were produced and delivered. The technical report in Section 3.3 describes the variety of components produced and the techniques used in production.

For the microshell substask, more than 900 glass microshells were sorted from existing stock and delivered. Also, 15 large (1 to 1.6 mm diameter) GDP shells were produced and delivered.

1.7. CR/LL1 CRYOGENIC LAYERING DEVELOPMENT

High gain cryogenic targets for ICF are spherical shells which contain a layer of DT ice surrounding a volume of DT gas in thermal equilibrium with the solid. The roughness of the inner surface of the cryogenic fuel layer inside of these targets is one of the sources of imperfections which cause implosions to deviate from perfect one-dimensional performance. Reductions in the surface roughness of this fuel layer improve the ability of NIF to achieve ignition. We have worked closely during the past year with the cryogenic group at LLNL in developing two techniques to smooth the DT ice layer.

One of the ways to smooth an ice layer is to cause heat to flow across the gas-solid interface. We generate this heat flux by applying an electric field to the deuterium tritium (DT) vapor in the center of a shell. This technique is called joule heating. The DT vapor has a small but significant conductivity due to ionization caused by beta decay of tritium in the vapor and the solid. Our experiments use a 10 GHz spherical microwave cavity to apply the electric field. A 1 mm diameter spherical plastic shell with a fill tube serves as the sample cell. The shell and cavity geometry closely mimic that of University of Rochester's cold transfer cryostat layering shroud. Because some of the microwave power is deposited in the plastic capsule, progress on joule heating has been limited by capsule imperfections and perturbations of the layer due to the fill tube. We have quantified the perturbations as a function of electrical field strength. Thermal modeling has been performed for a hollow sphere with a fill tube inside a one inch diameter spherical isothermal boundary. The adverse effects of the fill tube on layering symmetry have been identified and quantified.

The second technique, infrared (IR) heating, uses monochromatic infrared radiation to selectively excite rotational-vibrational bands of specific molecular hydrogen isotopes (HD in

recent experiments). This technique causes volumetric heating of the ice layer and is an analogue of the ß layering smoothing technique. The amount of IR heating in the bulk ice layer is controllable. The only way to adjust the ß heating due to decay of tritium is change the tritium concentration. This is not practical. Additionally, IR heating is the only known solid layering technique for non-tritiated hydrogen. With this technique, DT ice layers in 1 mm OD plastic capsules have been generated with layers as smooth as 2 microns rms. Again, the layering geometry has been purposely chosen to closely adhere to University of Rochester design constraints for the cold transfer cryostat.

A way has been discovered to make repeatably smooth ß layers in a spherical plastic shell. We find that the layer smoothness is dependent upon the cooling rate of the DT through the triple point. If the DT is cooled slowly enough, very good beta layers are produced. For one particular sample cell we consistently produced layers with 1.2 microns rms smoothness.

We have developed a novel technique to manufacture shells with small integral fill tubes. Fill tubes have been made with 20 μm outside diameters.

Optical characterization of DT layers in spherical plastic shells is a challenge due to the lens effects of the shell and the ice layers. Ray tracing analysis has been done for a plastic shell with a DT ice layer. We have verified the bright ring that corresponds to the ice layer and correlated the measured layer thickness to the actual layer thickness.

1.8. CR/LA1 BETA LAYERING SUPPORT AT LANL

The beta-layering work at LANL during FY97 has included a modal analysis of D_2 solid layering experiments performed in a 2 mm heated torus; a re-examination of DT solid layering data for which the evolution of the P1 defect can be observed; DT solid layering experiments inside 2 mm heated tori; DT solid layer experiments inside a 2 mm beryllium torus; and DT solid layering experiments in which the tritium fraction was lowered for each experiment. Additionally, the image reduction/analysis software was revised to allow real-time image processing and analysis, which allowed a significant improvement in productivity.

Surface RMS modal dependencies for D_2 solid layers formed inside a 2 mm torus with an internal heater were examined for very low heater powers. This examination showed that most of the D_2 solid surface roughness occurs in mode 10 and under, although some smoothing was observed in the higher modes. These low power de-faceting experiments also showed that very little heater power (2 μW or less) will turn the D_2 faceting process into smoothing.

The DT solid layering experiments performed in a hemispherical sapphire cell, for which the evolution of the P1 mode could be observed, was re-examined. Under these circumstances, the bottom section of the layer is grown from liquid, whereas the top section is grown

from vapor. This examination showed that after equilibration, the section of the layer at the top of the cell was measurably rougher than the bottom section layer, even though the upper layer was often more free of optical defects There were significant uncertainties in these measurements, but the results suggest that further investigation of the phenomenon could be more revealing.

A number of freeze/thaw cycling experiments were performed inside a 2 mm beryllium torus to investigate the surface roughness stochastics of DT solid layers on beryllium surfaces. Several of these experiments also included sudden temperature changes, to examine temperature stressing effects on the DT solid layer. Slow freezing experiments were also performed to examine the impact on DT surface roughness. Sudden temperature changes, either increasing or decreasing, nearly always produced layer smoothing and never resulted in layer roughening or cracking. Slow freezing did not improve layer surface smoothness and often resulted in rougher DT solid layers.

Experiments were also performed to examine the surface roughness impact of varying tritium fraction in the DT charge. These experiments were performed at progressively lower tritium fractions, beginning at 99% tritium, and consisting of freeze/thaw equilibrations at 0.4 K below the DT mixture triple point. Results show that tritium fractions above 50% do not produce smoother solid layers than the 50% fraction, and that the layer begins to roughen measurably at 40%. Experiments will be continued at 30%, 20%, and perhaps 10%.

1.9. CR/UR1 OMEGA CRYOGENIC TARGET SYSTEM ENGINEERING

During the past year, significant progress was made in the design of the OMEGA Cryogenic Target System. In February 1996 a decision had been made to locate the Transfer Station from under ''La Cave'' to room 157 and place it into the same glove box as the Fill Station, using the Moving Cryostats to transfer individual targets from Room-157 to La Cave. At that time there were still three separate cryostats: the Permeation Cryostat, the Cold Transfer Cryostat, and the Transfer Station, all housed in the same glove box. This system was greatly simplified in 1997 by combining the functions of these three units into one unit: the Fill/ Transfer Station (FTS) and its preliminary and final designs were completed.

Great progress was also made toward completing the Cryogenic Target Positioning System (CTPS) design. This system consists of four subunits: the Moving Cryostat (MC), the Moving Cryostat Transfer Cart (MCTC), the Lower Pylon (LP), and the Upper Pylon (UP). The preliminary design phase was completed, and preliminary design reviews were held for the four major subsystems. Final design work is nearly complete.

A significant amount of effort was spent on thermal analyses of the final design of the MC, both for steady state and transient conditions. This effort was strongly supported by Ido

Anteby from UR/LLE. Extensive effort was devoted to minimizing the size of the MCTC. The volume envelope of the final design is now approximately a 5 ft cube with an estimated weight of about 4000 lb. A detailed LP design was developed, including the "drawbridge" area that positions the MC for the Characterization process. However, UR/LLE decided that initial characterization will take place in the target fill room and no further work was done on the lower pylon. The upper pylon design was developed, and then significantly revised to reduce capital cost.

The integrated control system design progressed from the conceptual design phase to the preliminary design phase. During that time, a control system architecture was developed and the functions and requirements of these control system hardware components were developed. The Balance of Plant (electrical supply, process air, process water, cooling water) defining the utilities required for the OMEGA Cryogenic Target System (OCTS) was completed. Because of the high cost of an integrated control system and UR/LLE's requirements for integrated control they decided to take the lead in designing, fabricating, installing, and testing the control system. GA is assisting UR/LLE during this design phase on an as-needed basis.

Work began this year on designing the Cryogenic Target Characterization System (CTCS) based on University of Rochester's design of a convergent beam interferometer. The CTCS is composed of three systems plus the optical tables which will hold the optical components at the lower pylon windows. A layout of the CTCS was completed this year and provided to the University of Rochester. UR/LLE has taken over the final design of the CTCS.

Last year, the prototype fill equipment was used to demonstrate the feasibility of high pressure filling, cooling, and transporting of cryogenic polymer targets with the UR/LLE C-mount design. In FY97, prototype equipment and target filling operations were directed at the filling of shells with even thinner walls. While the equipment was designed to operate with wall thicknesses down to 5 μm, successful demonstration fills and cryogenic verification with wall thicknesses as low as 3.3 μm were accomplished.

During FY97, LANL, in addition to providing design support on issues related to tritium handling, took on responsibility for the design of the OCTS glove boxes, vacuum systems, and tritium removal systems. A preliminary design for two glove boxes was developed, specifications were written, and a contract for construction of the glove boxes was placed in September 1997. The design for the vacuum systems for the OCTS was completed in FY97 and orders for the major vacuum system components was initiated.

2. COMPOSITE POLYMER CAPSULE DEVELOPMENT AND PRODUCTION

A major element of the ICF target fabrication activity is development of new techniques for production of improved targets for future deliveries. Some of these activities are described here.

2.1. CAPSULE DEVELOPMENT

We have made substantial progress in improving the specification envelope of our shells. GDP on glass shells can contain more than 100 atm of gas. PAMS/GDP process NOVA shells are much rounder and more uniform than their drop tower predecessors, and OMEGA shells are being made with better dimensional control and reliability than before.

2.1.1. POLY(ALPHA-METHYLSTYRENE) (PAMS) MANDREL PRODUCTION DEVELOPMENT

The basic PAMS mandrel production process was developed at LLNL, and then transferred to GA in FY96. By the end of last year, we were delivering target quality OMEGA and NOVA GDP shells built on our PAMS mandrels. The process was not completely reliable, and production of satisfactory batches of mandrels was intermittent. We spent much of FY97 establishing tighter controls on the production process so that we could meet target specifications more reliably. By the end of FY97, we had developed a better understanding of the shell production process, and instituted process modifications which resulted in a majority of mandrel batches meeting specifications for wall thickness, diameter, and wall uniformity. That was accomplished with improved controls on diameter, and an improved understanding of vacuoles formation and the curing process. Details of those developments are described below after a quick review of the PAMS production process (see GA's ICF Annual Report for FY96 for a more detailed discussion of the process).

Overview of PAMS Production Process. The liquid preforms of the mandrels are composite oil/water drops produced in a droplet generator modeled after the device used at Osaka University (Fig. 2-1). A dual orifice needle is used to inject the water inside an oil stream (11 wt% PAMS in fluoro-benzene). The oil is stripped off the needle to form the composite drop by the

flow of external water solution past the needle. The relative flow of the inner water (W1) and the oil (O1) phases controls the final wall thickness. The flow of the outer water phase (W2) controls the droplet size. The droplets are collected in a beaker which is then heated and stirred for 3-4 hours to evaporate the fluoro-benzene from O1 and produce solid, water-filled shells. The shells are put in ethanol to create an osmotic pressure to allow extraction of inner water phase by diffusion. When a bubble has formed (sonication is used to help this process) the drying is completed in a vacuum oven at ~60°C.

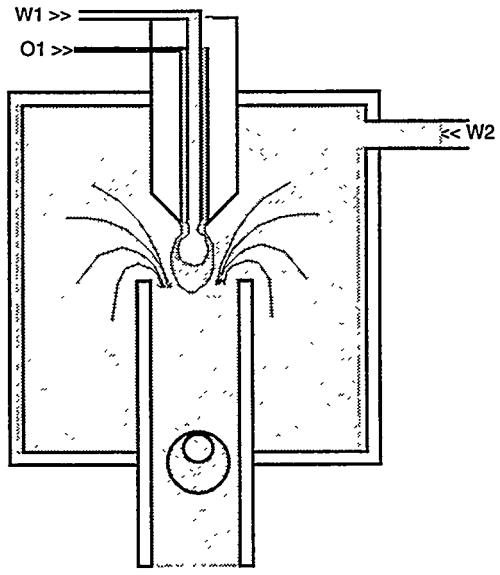

Fig. 2-1. Schematic of shell preform production using a droplet generator. The droplet size is predominantly controlled by the W2 flow rate; the wall thickness by the ratio of O1 to W1. The droplets are collected in a stirred, heated bath where W1 is centered in O1, and then the O1 solvent is removed to produce solid plastic water filled shells. The water is removed by permeation.

Improved Diameter Control. The droplet generator readily makes shells with a very narrow diameter distribution (o.d. ~±1 %). At the beginning of FY97, this precision was not matched by an equivalent accuracy. As a consequence, we could produce a batch of thousands of shells, 100% of which could miss meeting the required o.d. by a small amount. ("Shake-and-toss," an earlier microencapsulation technique, naturally produced a wide range of sizes, so we could sieve to get a small number of the desired o.d.) One of the efforts this year was to improve process controls so that the accuracy of our diameter control matched its precision. Currently the accuracy and precision are ±1.5% and ±1.0%, respectively (Fig. 2-2).

That was accomplished by using a stroboscope to measure the frequency of droplet generation. In combination with the syringe pump settings for W1 and O1, we could determine the average volume of W1 and O1 in each drop. We can measure shell generation rate to

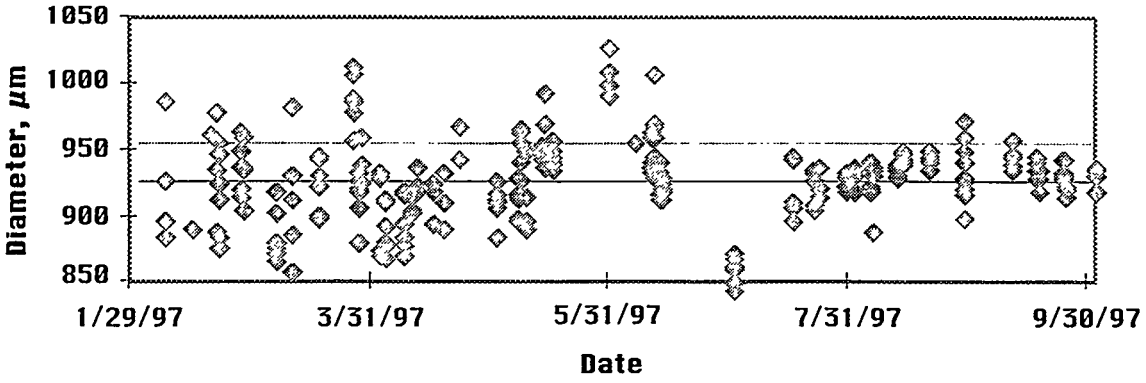

Fig. 2-2. Average shell batch diameter versus run date for OMEGA shell mandrels. The horizontal lines are the o.d. limits for acceptable shells. Typically, six batches are produced in every run. The variation of batch o.d.s within a run is ~10 µm. After implementing the precision stroboscopic stripping rate measurement this summer, the run-to-run variation of batch o.d.s was reduced to ~30 µm.

within ±1 shell/minute (±0.016 shell/s) and find that >70% of the shells are produced within the o.d. specifications (940±15 µm for typical OMEGA shells).

Improved Surface Smoothness — Vacuole Control. The microencapsulation process has been plagued by bubbles in the walls from its inception. The bubbles are thought to arise from the diminishing solubility of water in the oil solution as the solvent is removed. At some point, the walls are supersaturated in water, and water droplets precipitate in the oil phase. These droplets appear as vacuoles when the shell is dried. With optimization, the vacuoles could be reduced to insignificance for polystyrene shells (see GA's ICF Annual Reports for FY94, 95). Vacuoles were far worse in PAMS; they were present at high concentrations and large sizes. At first we did not consider that a problem, since with the PAMS/GDP process we decompose the PAMS mandrel, and there are no vacuoles in GDP. During this year, we came to realize that these vacuoles were perturbing the surface of the mandrel, and that added roughness was replicated in the GDP shell.

A new insight — that O1 could be kept sufficiently dry to prevent vacuole formation during the curing process — allowed us to substantially eliminate the vacuoles in the PAMS mandrels, resulting in substantially smoother GDP shells. We proposed to eliminate the vacuoles by reducing the tendency for water to enter the PAMS/fluorobenzene phase. More specifically, we wanted to lower the thermodynamic activity of the exterior water (W2) relative to the activity of the water precipitated in the oil phase (O1).

One can alter the relative activities by adding solutes, but the additive must meet several constraints: (1) it must not get into the interior water drops in the oil phase (eliminating the differential activity), and (2) it must not adversely affect the polyvinyl alcohol (PVA) in the external water phase. We settled on the salt $CaCl_2$. Salts in general do not dissolve in fluorobenzene (the solvent in O1), and $CaCl_2$ in particular is compatible with the PVA we use

in W2 (to prevent shell agglomeration). Studies showed that the vacuoles were much reduced, by using >1.0 wt% $CaCl_2$•2 H_20 in W2 (Fig. 2-3). We settled on using 1.5 wt% for our routine production. Figure 2-3 also shows, for this comparison, the atomic force microscope (AFM) spheremapper power spectrum. One sees a reduction in amplitude in modes 10-200 as a result of vacuole reduction. Collecting all our AFM spheremapper data, one sees a dramatic consistent reduction at these modes, as soon as $CaCl_2$ became part of the production process (Fig. 2-4). Although the AFM spheremapper plot of shells made with $CaCl_2$ is generally better than those shells made at the same time without $CaCl_2$, there are significant run to run variations. Many runs made with $CaCl_2$ will not have AFM spheremapper traces better than the NIF standard.

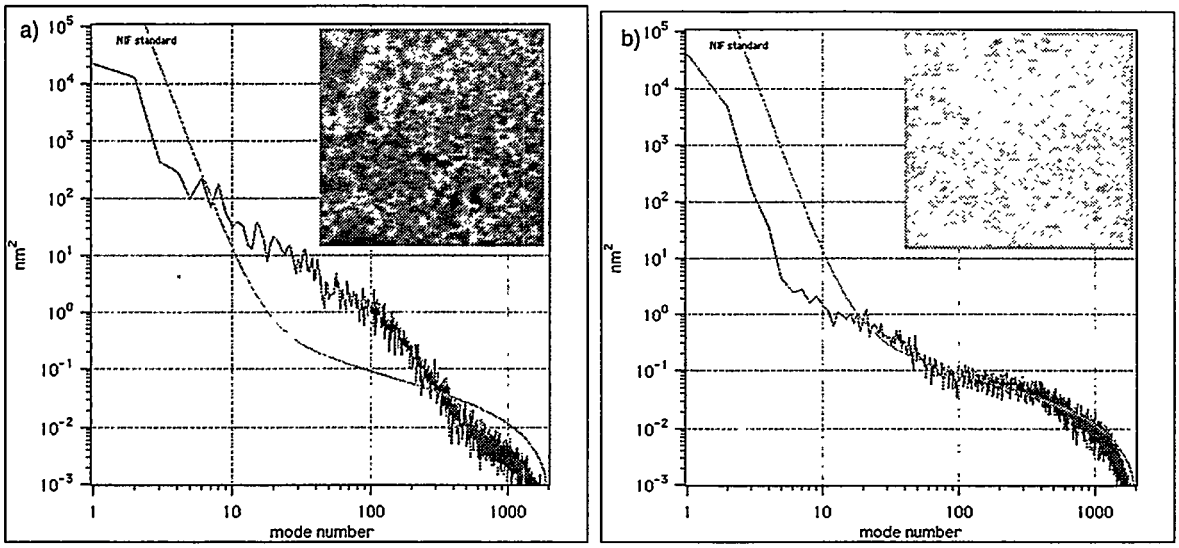

(a) PAMS shell made without $CaCl_2$ (b) PAMS shell made with $CaCl_2$

Fig. 2-3. The existence of vacuoles in the walls of the mandrel perturb the surface in the mode range 10–200. The addition of $CaCl_2$ in the W2 phase nearly eliminates vacuoles and improves the surface finish.

The $CaCl_2$ is added to W2 in the collection beaker, after the shells are made, so that $CaCl_2$ cannot interfere with droplet formation. If the $CaCl_2$ is added too late — a couple hours into the curing — the polymer wall is already firm and vacuoles are fixed in the wall. Typically, the salt is added within 30 minutes after the collection beaker is filled with shells and put into the curing bath. The vacuoles are not reduced to zero. Since the interior water still has pure water, there is an activity gradient set up across the wall and vacuoles can still form near the inner surface of the shell. This activity gradient also results in some osmotic transport of water from W1, the interior pure water phase, to W2, the outside PVA/$CaCl_2$/water solution. This results in a shrinkage of the inner water phase volume, and thus a shrinkage of the resulting shells. We found a shrinkage of ~20 μm in the o.d. of OMEGA mandrels when using $CaCl_2$, compared to the absence of $CaCl_2$ (Fig. 2-5).

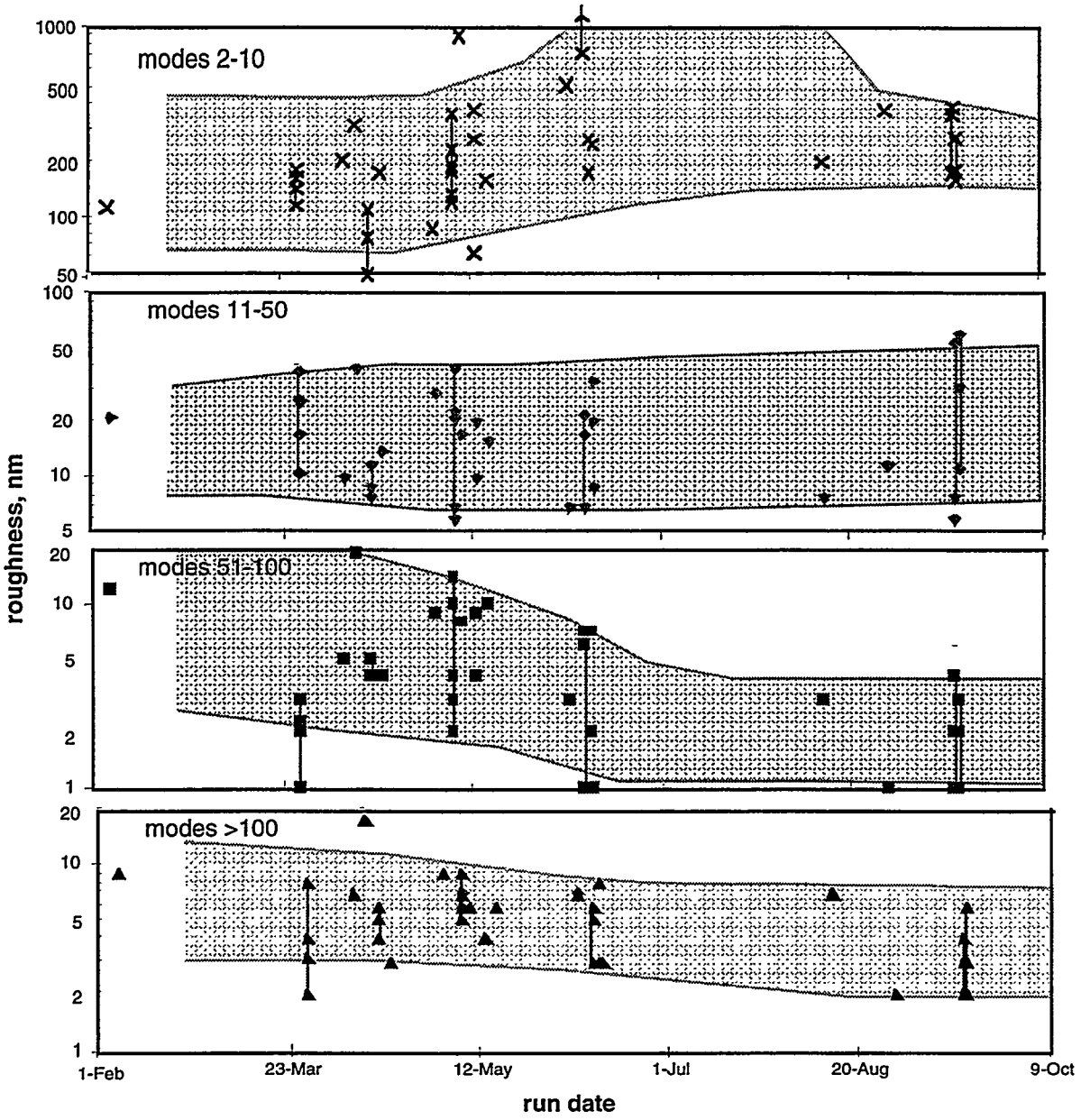

Fig. 2-4. AFM measured roughness amplitude of PAMS mandrels as a function of run date for four ranges of modes. The shaded bands indicate the range of values observed in each of four mode ranges. Modes 2–10 are the low modes dominated by the out of round of the shell. During the summer, we were having difficulty controlling those modes (see also Fig. 2-6). Modes 51–100 are intermediate modes dominated by vacuole perturbations. The amplitude in that band decreased ~5X when we began using $CaCl_2$ to remove vacuoles from the mandrel walls.

Although the surface smoothness of the shell wall has been improved by reducing the number of vacuoles, we unfortunately see features on the interior surface in a fraction of the shells in a batch, (30%–100%). Optically, these features are very obvious as a field of spots over a region (rather like water drops on a waxed surf board). With a scanning electron

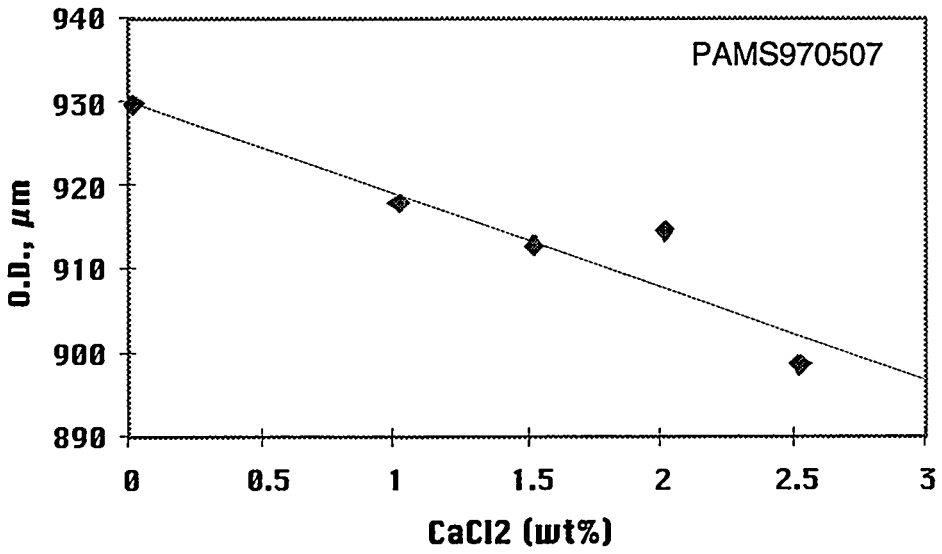

Fig. 2-5. Outside diameter of PAMS mandrels as a function of $CaCl_2$ concentration in W2 (the external water bath) during curing.

microscope (SEM) , these spots are more difficult to observe, as they are very shallow domes less than 1 µm in height. These spots are not crystalline, nor do they have sharp edges or points. Energy dispersive x–ray analysis (EDX) within the SEM shows the presence of O, Ca, and Cl (beyond the typical C and Au of the carbon and background PAMS). Our best guess, given the presence of O, Ca, and Cl, is the presence of $CaCl_2$ and PVA on the inside of the shell. Upon GDP coating and pyrolysis, a similar field of spots results on the inside surface of the GDP shell.

The presence of Ca and Cl on the inside is puzzling, as the $CaCl_2$ is added to the exterior of the shell substantially after the encapsulated droplet is formed. The diffusion of $CaCl_2$ through the PAMS/fluoro-benzene layer is unlikely, based on low solubility alone.

In spite of the occurrence of interior features, these shells appear overall to be as clean or cleaner than those made at the end of last year (Fig. 2-6).

Improved Out-Of-Round (OOR) — Density Control. The spherical perfection of the mandrels is established by the interaction of the spherodizing interfacial tension with distorting shear and gravitational forces. This is not an issue with NOVA shells, but the effectiveness of the interfacial tension diminishes, and that of the distorting forces increases with mandrel diameter, such that we had significant problems with OMEGA shells during FY97, (particularly starting in May — see Figs. 2-4 and 2-7) in achieving the OOR specifications.

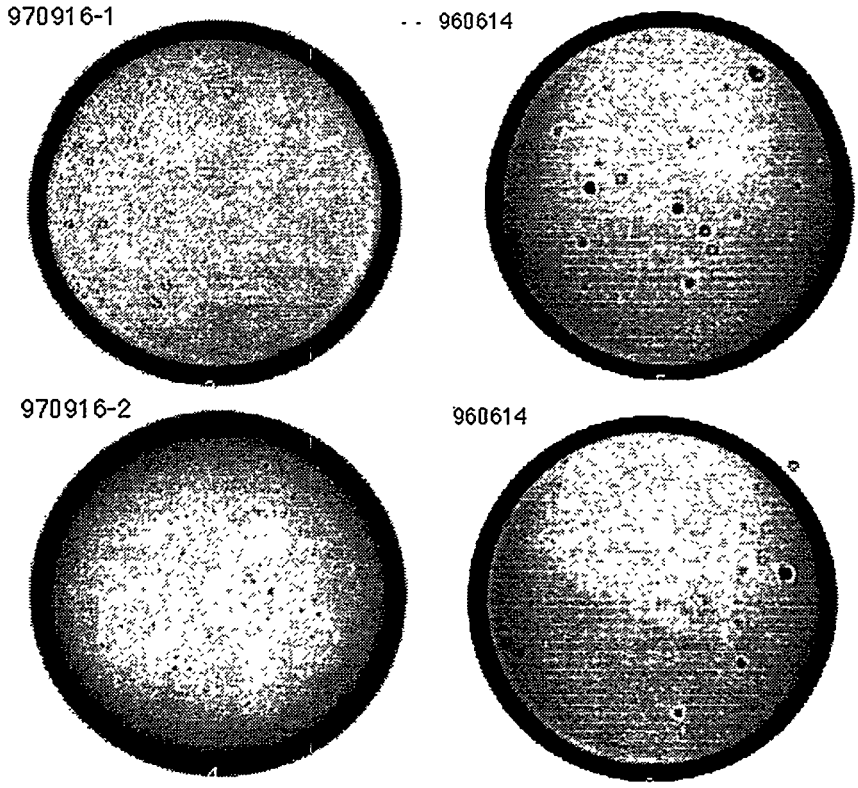

Fig. 2-6. GDP shells made from PAMS mandrels. The shells on the right, labeled 960614 are the best made at the end of FY95. The shells on the left, labeled 970916-x, are typical of shells made at the end of FY96. The shell 970916-1 was made from a PAMS mandrel containing interior features; their resulting marks can be seen as light dots on the left half of the image.

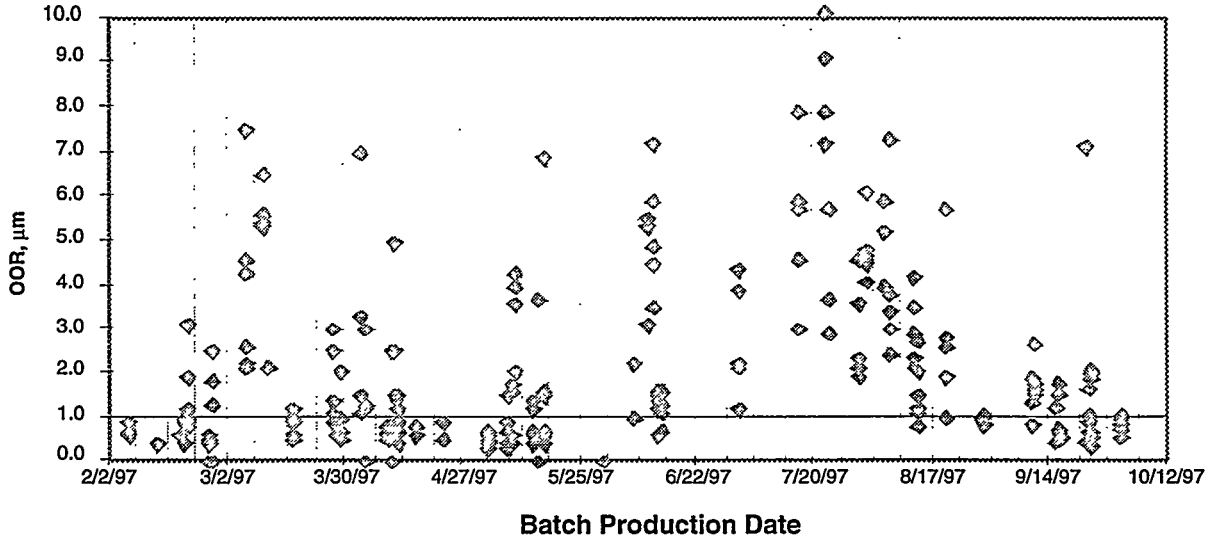

Fig. 2-7. Batch average out of round versus run date for OMEGA PAMS mandrel runs. The horizontal line is the upper limit for acceptable OOR. The cure temperature was reduced to ~40°C at the end of August, and the OOR immediately fell below 2 µm, except for a stirring speed test, and is now predominantly below 1 µm

Ultimately, we returned to some fundamental thinking of what controlled the out-of-roundness. R. Cook of LLNL had done an analysis using the shape of a single phase sessile drop in a fluid, which proposed

$$\max \mathrm{OOR} = 9\,\Delta\rho\, r^3/\gamma \qquad (2\text{–}1)$$

where $\Delta\rho$ is the density mismatch between O1 and W2, γ is the interfacial surface tension, and r is the drop radius. We made rough measurements of the surface tension and found values of $\gamma = 6$–12 dyne/cm, which was smaller than what we had anticipated (the literature value of the fluoro-benzene/water interface is 35 dyne/cm). At this point, we looked at the density mismatch, to see if it could be minimized. In the absence of $CaCl_2$, O2 is density matched with W2 at 60°C, which had been the curing temperature used. Upon using $CaCl_2$, the W2 density increased by about 0.01 g/cc, which led to a density match with O2 at about 40°C rather than 60°C. We reduced the curing temperature from 60°C to 40°C, and promptly got OOR (and NC) down back into the specification range (Fig. 2-7).

For further information, please contact Dr. R. Stephens or Dr. B. McQuillen (GA).

2.1.2. NOVA CAPSULES

NOVA capsules consist of a 450 μm thin polymer shell coated with several microns of PVA and then coated with several tens of microns of GDP. Since the first capsules were made nearly ten years ago, the inner shell, also called a mandrel, was made from polystyrene using the drop tower process [2-1]. All drop tower shells suffer from a significant P1 defect. In capsules, the defect is exacerbated by the addition of PVA although it can be mitigated in the total wall thickness by using "sizzle-coating" to deposit the GDP layer [2-2]. Polymer capsules made by the GDP/PAMS technique have a nearly negligible P1 defect. Substituting GDP mandrels for polystyrene mandrels results in improved complete capsules (Table 2-1).

TABLE 2-1
NOVA CAPSULES CHARACTERISTICS WITH POLYSTYRENE OR GDP MANDRELS

	Polystyrene mandrel	GDP mandrel
noncircularity	1.1 μm	0.3 μm
$\Delta w = t_{max} - t_{min}$	1.7 μm	0.7 μm
fringe wobble	0.5 fringes	0.3 fringes
AFM, modes 2 – 10	274 nm	124 nm
AFM, modes 11 – 50	5 nm	10 nm
AFM, modes 51 – 100	1 nm	1 nm
Small optical features (2–5 μm width)	few	≥ few

NOVA capsules made with GDP mandrels are superior to capsules made with polystyrene mandrels for noncircularity, Δw, fringe wobble, and lowest order AFM modes. Fringe wobble is a measurement of how interferometry fringes shift as a capsule is rotated, and is an indication of higher modes. The AFM modes are the power modes from an AFM sphere-mapper. In the middle AFM power modes, capsules made with a polystyrene mandrel are slightly better (Fig. 2-8).

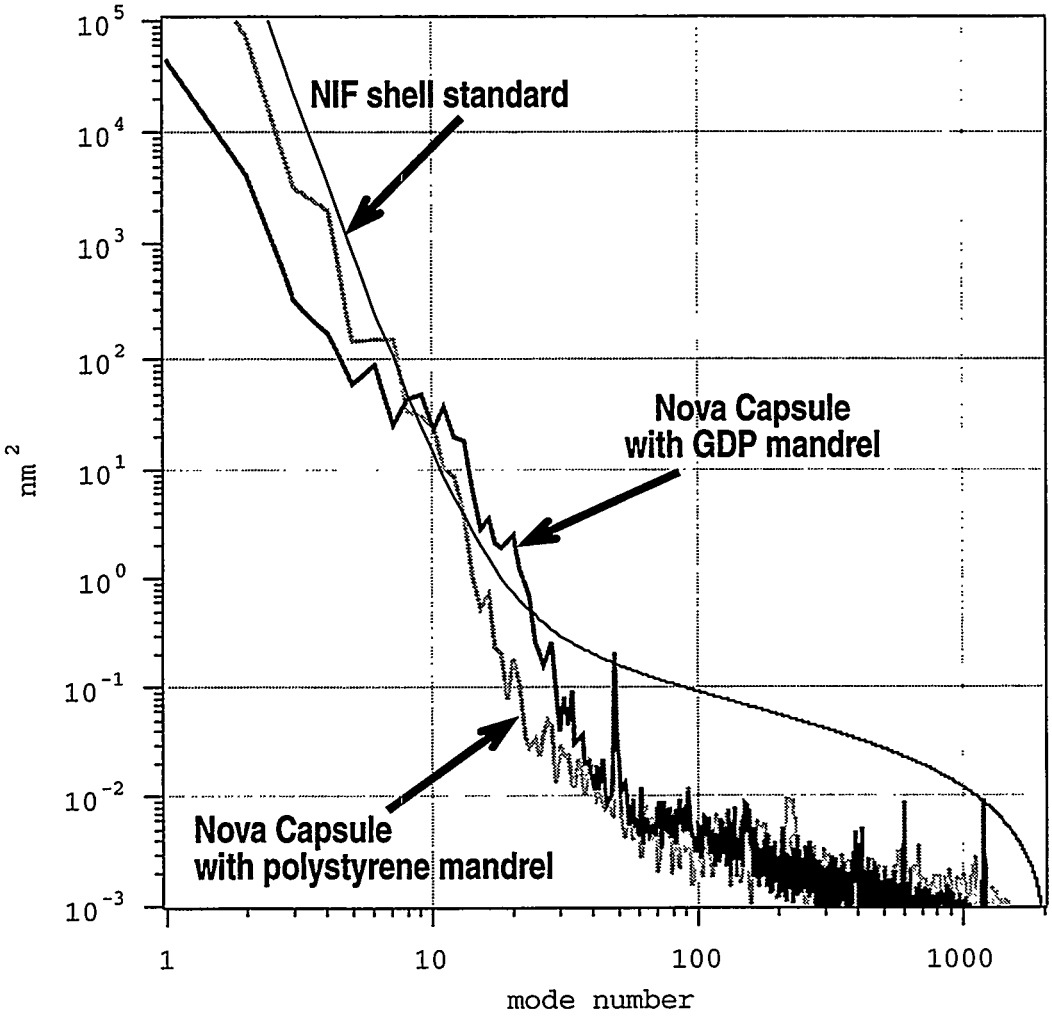

Fig. 2-8. Nova capsules whether made with a GDP mandrel or with a polystyrene mandrel compare favorably with the "NIF standard." Capsules with the GDP mandrel are superior in low order modes while capsules with a polystyrene mandrel are better in the middle modes.

NOVA capsules are now much improved over the capsules made in 1995. At that time the Δw of some capsules was as high as 5 μm while most capsules had a Δw of 2 μm or more. Now most shells have a Δw below 1 μm. Further improvements in NOVA capsules will require a more uniform permeation barrier.

For further information, please contact W. Miller (GA).

2.1.3. GDP ON GLASS CAPSULES

Cryogenic layering experiments using free-standing two millimeter DT-filled capsules must be conducted to give the ICF community the knowledge needed to field targets for the NIF. To date, cryogenic experiments have used capsules and hemi-shells fitted with fill tubes because capsules able to hold over 100 atm of DT gas at room temperature were not available. We have developed one type of capsule capable of holding high pressure helium or deuterium. It consists of a large glass shell (~1300 O.D. x 3 μm wall) over-coated with a thick layer (~100 μm) of GDP. LANL scientists plan to soon fill capsules of this type with over 100 atm of DT and learn if they are suitable for NIF cryogenic layering experiments.

Glass Shell Selection. The glass shells selected for this task were made in GA's high temperature (1650°C) vertical drop tower. The shells were selected for the following characteristics:

(1) Wrinkle-free appearance
(2) Wall thickness of 2.5-3.5 μm
(3) Diameters of 1200-1500 μm
(4) Wall Non-Concentricity (NC) ≤ 20%

GDP-coating. The glass shells were bounce-GDP-coated. A total of 50 capsules were prepared in four batches. After GDP coating, the capsules' centered interferometric fringe patterns indicated that the overall non-concentricity of the coated shells was ≤2%.

Burst Experiments. To determine how much internal gas pressure these capsules could hold, we conducted burst test experiments using helium as the fill gas. Helium has the advantage that it will permeate through glass at least an order of magnitude faster than will hydrogen. Thus, by using helium, we could conduct more burst test experiments in a given period of time.

We lowered the usual fill temperature from 360°C to 280°C, to minimize GDP degradation, and took 25 atm steps holding the shells at each step for 20 minutes. After conducting a series of tests with helium, we filled the shells with deuterium to confirm that several day-long fills with a hydrogen isotope were viable. In this fill, we used 20 atm steps and held the shells at 280°C for an average of 4 hours per step.

Table 2-2 below shows the results of the burst test experiments. Almost every capsule coated with 100 μm of GDP withstood 200 atm of helium fill. Only capsules overcoated with less than 90 μm of GDP consistently burst when filled to 200 atm.

TABLE 2-2
BURST TEST RESULTS

Fill	Fill Gas & Pressure	Fill Protocol	Results / Observations
1	Helium 130 atm	280°C; 25 atm steps 20 min. per step	4 of 4 shells survived
2	Helium 160 atm	same	10 of 10 shells survived 4 shells had been previously filled
3	Helium 200 atm	same	6 of 6 shells survived 4 shells had been previously filled
4	Helium 200 atm	same	5 of 15 shells survived All 9 shells of < 90 μm GDP failed 5 of 6 100 μm GDP shells survived
5	DD 90 atm	280°C; 20 atm steps 2 hours per step	6 of 6 shells survived Shells were slightly darker than shorter fills

Gas Fill Confirmation and Characterization Techniques. We found weighing was the best way to quantify the helium gas fill for multiple capsules. Several factors complicated this approach including: (1) the mass loss of GDP due to the high temperature fill and (2) oxygen and water vapor uptake by the GDP coating.

Because of the uncertainty of the mass loss of the GDP coating during the fill, we could not weigh the shells before and after the fill to accurately determine the mass of the fill gas. Rather, we determined the fill gas mass by weighing the shells immediately after the fill and again, several days later, when the shell had emptied. For deuterium fills, this approach is impractical as the deuterium fill half-life at room temperature is months long.

We addressed the problem of oxygen and water vapor uptake by first storing the capsules in a vacuum desiccator between weighings. Later, we used shells that had "aged" in air for several weeks before filling, and were no longer gaining weight.

Cryo Testing. We were concerned that the capsules might not survive cryogenic cycling in future DT experiments. To address this concern we tested both helium- and DD-filled shells by immersing them in liquid nitrogen. After overnight storage in a liquid nitrogen dewar, the shells were thawed in a vacuum desiccator. Optical inspection and weighing confirmed that the shells had survived the temperature cycling and had not lost any gas. Subsequent shell weight loss verified that the shells' out-gassing rate at room temperature was unaffected by the cryogenic cycling.

Summary. We have fabricated GDP-coated glass capsules that can be filled to over 100 atm with helium or deuterium. We used a fill temperature of 280°C that caused only a slight

darkening of the GDP layer. In a few months, we will learn if these shells can withstand a high pressure DT fill and be useful in cryogenic layering experiments.

For further information, please contact D. Steinman (GA).

2.2. COATINGS FABRICATION

Ti-GDP Coatings. The titanium-doped GDP (Ti-GDP) effort that was started near the end of last year was continued this year. Sample targets had been delivered to LLE in FY96. These contained approximately 0.5 atomic percent (atom %) titanium (Ti) as measured by x–ray microfluorescence. The results of OMEGA shots on these targets indicated that higher doping levels were needed to obtain a clear spectroscopic signal. Therefore, the emphasis of the project was shifted to making Ti-GDP coatings containing 2% or more Ti instead of the previously requested 1%. Using the traditional method of dopant introduction into the coating process, the highest concentration of Ti in films that had reasonable stability was only 0.7%. A new scheme was needed to make stable films with higher Ti concentrations. The films in the glass coating tube itself provided a clue to a possible solution to the problem. As mentioned in last year's annual report, the coatings in the plasma tube itself appeared to be far more stable than the coatings on the substrates. Qualitatively, this seemed to indicate that the dopant molecules that were dissociated and incorporated into the final film in the radio frequency (RF) region were bound more stably. To simulate this situation for the shells, the dopant introduction scheme was modified as shown in Fig. 2-9. The dopant ($TiCl_4$) was brought into the system directly over the substrates and into the plasma plume exiting the coating tube. The flow of the other gases in the coating process, hydrogen and trans-2-butene, were left unchanged. With this change, thin stable coatings (≤ 5 μm) containing as much as 5% Ti were made. The coatings were mechanically stable enough to be characterized without the need for any special sample handling or storage equipment. This allowed rather routine characterization of the shells and coatings. However, exposure to oxygen was kept at a minimum. All films also contained chlorine at about a 1:1 atomic ratio with titanium.

These films normally looked dark gray to black in color immediately after the coating, but then proceeded to become lighter as the coating was exposed to air. This was presumably due to oxidation of the Ti atoms in the film. Coatings with higher than 5% Ti concentrations, however, changed color very quickly, within one minute. They lost their integrity very quickly and turned into an oily looking film. The liquid had a pungent smell and may be HCl. Pyrolysis of films at 300°C removed almost all the chlorine, while there was no measurable loss of titanium. The loss of chlorine and some CH groups during the pyrolysis actually increased the titanium atomic % after pyrolysis.

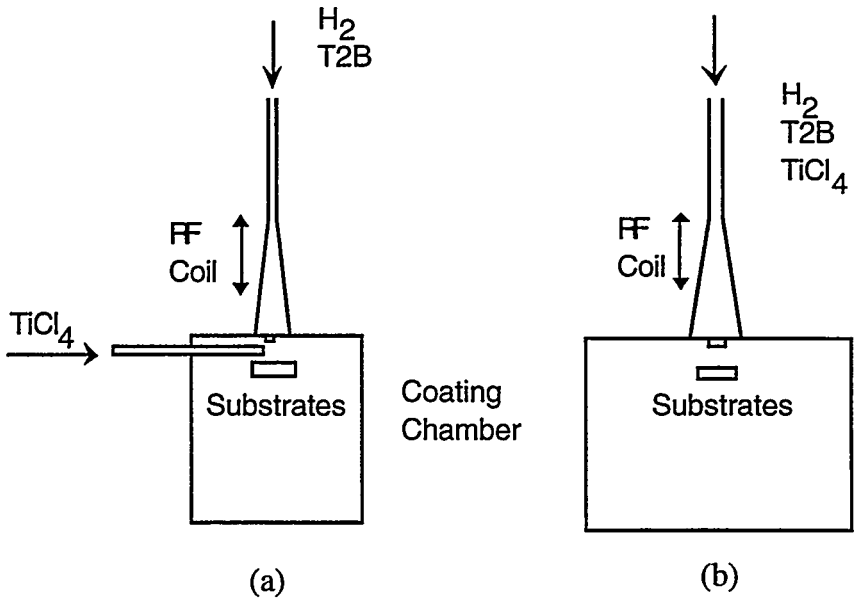

Fig. 2-9. Introducing the dopant from the side over the substrates (a) results in stable coatings with up to about 5 atomic % Ti. The highest Ti concentration that resulted in stable coatings using the traditional dopant introduction method (b) was less than 1 %.

Targets for LLE usually involved a final shell with a thin (≈ 1 μm) Ti-GDP layer sandwiched between undoped layers. The Ti-GDP layer was placed at different positions in a final shell of about 20 μm thick. It was found that the Ti-GDP layer cracked in the composite shell after pyrolysis of the PAMS layer, for Ti layers of concentrations above 4%. The number of cracks increased as the thickness of the GDP layer underneath it decreased. Ti-GDP layers with about 4% or less Ti did not crack in the composite shell after pyrolysis. However, thicker coatings (≥3 μm) with lower Ti concentrations (as low as 2.5%) also exhibited this problem before and after pyrolysis. For experiments at LLE, initially, a number of sample shells with the higher Ti content were made and shot at OMEGA. The results indicated sufficient Ti content in these coatings. Subsequently, it was determined that the concentration of choice was between 2% and 4%. We were able to make good integrity 900 μm diameter Ti-GDP shells with 5 μm thick walls and containing about 3.3% Ti after pyrolysis.

The coating rate was related to the Ti concentration. The higher the Ti concentration the higher the coating rate. Therefore, at a doping level of 4% the coating rate was 0.5 μm/hr, while at 2% Ti, the coating rate dropped to about 0.3 μm/hr. The introduction of the dopant from the side of the coating chamber led to an expected lateral non-homogeneity of the Ti concentration. The Ti concentration in films deposited on flat substrates near the dopant delivery tube exit was much higher than those deposited far away from it. When coating shells, this was less of a problem, since the shells bounced around in the pan and received an average Ti concentration. It did present a problem when thin shells of different wall thicknesses (≈ 6 μm or less) were coated together (Fig. 2-10). The mass difference between these shells caused the heavier shells to bounce closer to the center of the pan, while the lighter

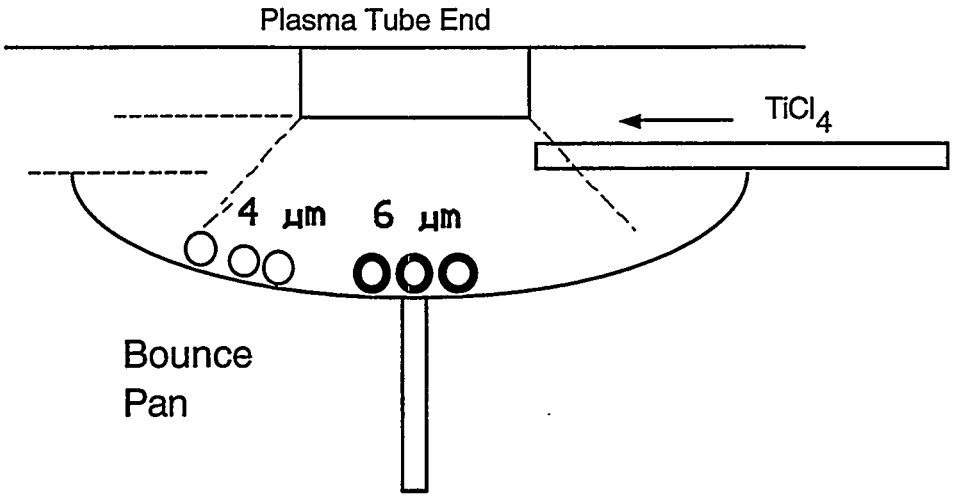

Fig. 2-10. Introducing the dopant from the side of the coating pan results in lateral non-homogeneity of the Ti concentration. Thin walled shells (<≈10 µm) bounce in different positions in the pan as shown. This leads to different Ti concentrations and coating rates for shells of different wall thicknesses. For example, for 4 µm versus 6 µm thick mandrels this leads to ≈ 20%–40% difference in the Ti concentration.

shells mainly bounced away from the center. This led to a higher Ti concentration on the thicker shells. For example, in a batch of 4 µm thick shells coated together with a batch of 6 µm thick shells the difference in the concentrations was between 20% and 40%. The coating rate was also higher on the heavier, thicker shells, as is the case for even undoped GDP coatings. Therefore, the total number of Ti atoms deposited on 6 µm mandrels was about twice as many as that deposited on 4 µm shells in the same run.

The major problem with the deposition system was irreproducibility of the Ti concentration from run to run for the same coating parameters. Run to run variations were initially from 0.1 to 1.0 atomic %. The major cause of this problem was the low flow of the dopant required to make films with the desired Ti concentration. The flow of $TiCl_4$ that resulted in a coating with 4 atomic % of Ti was approximately 0.01 sccm. Good control of such low flow was beyond the limits of the flow control system. The reproducibility was improved to between about 2% to 4% Ti by adding an argon flush line to the dopant line and carefully zeroing the controller before each run. We further improved the reproducibility by the following method. The $TiCl_4$ flow was increased by about four fold through the flow controller. At the same time the flow controller output was split into two paths. One involved a small inner diameter tube that directed the flow into the chamber, while the other path was a tube of twice the inner diameter connected directly to the vacuum pump. In this way, most of the higher flow through the controller was dumped into the pump, while keeping the flow to the chamber the same as before. This allowed better control of the flow, while keeping the Ti concentration the same in the coatings. With this setup, many of the latest coating runs with identical parameters yielded coatings with between 2.5% and 3.0% Ti.

GDP Surface Finish. We encountered a problem in using the piezo bouncing system in coating large numbers of various types of shells. Frequent collisions between the shells during the deposition of the coating resulted in dome-filled surface finishes for the shells and production of small beads during the coating. In particular, we found dome filled-surfaces after GDP coating of pristine OMEGA size PAMS mandrels [Fig. 2-11(a)] when shells were bounced vigorously in a piezo-based bouncer. Coatings of 3 μm or less exhibit very few domes, while once the thickness was above 4 μm the surface became filled with domes. The density of domes increased as the thickness increased. Spherical beads of about 10 μm diameter were usually seen attached to the shells [Fig. 2-11(b)]. The beads could be washed or knocked off and were therefore not integrated into the coating. The background surface finish in areas between domes, however, was the usual ≤1 nm RMS. Optically, the dome filled shells actually appeared to be dirty, with the shell covered with small particulates perhaps left over from a dirty PAMS mandrel. However, the dirty look of the shell was solely due to the high frequency of the domes. The domes result in power increase in the modal spectrum of the shell as examined by the AFM spheremapper. While the main contribution of the domes was to modes greater than 100, there was a significant increase in the power in modes 10–100. In particular, mode 100 power was almost one order of magnitude higher on the GDP coated shells.

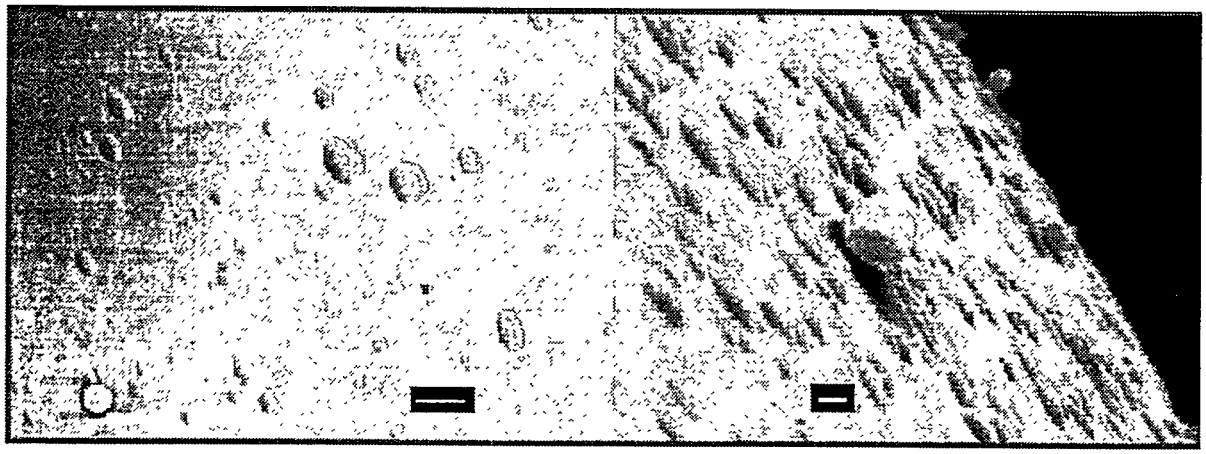

(a) (b)

Fig. 2-11. (a) Scanning electron microscope (SEM) image of the surface of a 12 μm coating of GDP on an OMEGA (900 μm) size PAMs mandrel. The surface contains numerous domes. This shell is one of 120 shells bounced coated together at once. The bouncing action was very vigorous in order to obtain a uniform GDP coating on the non-uniform PAMs mandrel. A bead can be seen near the lower right hand side of the image. The scale bar is 10 μm. (b) A side view of the surface of another shell exhibiting many domes on the surface. The presence of beads along with the domes is clearly seen in this view. The bead is about 10 μm tall.

We set out to determine the cause of such poor surface finishes. These types of surface finishes were found in three different independent coating systems, with the problem occurring intermittently. Uncleanliness of the system or feed gases is usually suspected when such surface finishes are encountered. All systems were carefully cleaned, but the problem persisted. The quartz plasma tubes used in our plasma polymerization systems are usually cleaned and reused. They are also one of the few items that all of our systems have in common. To examine possible contamination because of improper cleaning of the tubes, we performed a set of experiments as follows. The same tube was used repeatedly without cleaning to deposit about 10 μm of GDP on various substrates. The coated surface was dome filled only when a large number of shells (100 or more) were coated together, while coatings on flats or on small number of shell were virtually dome free. The original PAMS mandrels were all chosen to have clean surfaces. Thus, there appeared to be a correlation between the number of shells coated and the surface finish. The shells were bounced very vigorously in all these runs in order to correct for the non-concentricity of the original PAMs mandrels [2-3]. Gentle bouncing of a large number of shells was tried next. The surface had far less domes than when the shells were bounced vigorously. Therefore, vigorous bouncing of large numbers of shells was creating seeds for domes observed on the surface. One final experiment proved this conclusively. Over 100 OMEGA size PAMS were vigorously bounced and coated together in a pan, while a few shells were simply attached to the bottom of the coating tube away from the pan. After the coating, the surfaces of bounced shells had numerous domes and beads, while the shells that were away from the pan had virtually dome free surfaces.

Shells of different diameters were bounce coated both vigorously and gently in large and small batches in separate coating runs to further examine the process. Results similar to coating of OMEGA shells were obtained with Nova size, NIF size and 1.6 mm shells. The difference for each size was the number of shells that can be coated together without having a dome-filled finished surface. This maximum number became smaller as the diameter of the shells increases. The dependence appeared to be cubic. A simplified plausibility argument for this and a discussion on the origin of these domes can be found in Ref. 2-4.

The problem of using a piezo-based shaker to coat larger size PAMS shells had been encountered previously by Letts *et al.* [2-5]. A pan mounted on a swaying rod driven by a mechanical shaker had improved the surface finish in that case. We found a dramatic reduction in the number of domes if the larger (OMEGA size and larger) shells were coated in a spinning tilted pan. A 15 degree tilt angle was enough to cause constant agitation of the shells without any sticking problems when the pan was spun at approximately one RPM. RPMs greater than about 2 RPM resulted in hard collisions between shells while sliding down the tilted pan which knocked some shells out of the pan. A tapper was used to loosen any stubbornly stuck shells. The spinning action of the pan kept the shells agitated while reducing the probability of collisions between shells. The shells in effect kept chasing each other in this configuration instead of running into each other as in the piezo shaker setup. Figure 2-12 illustrates the

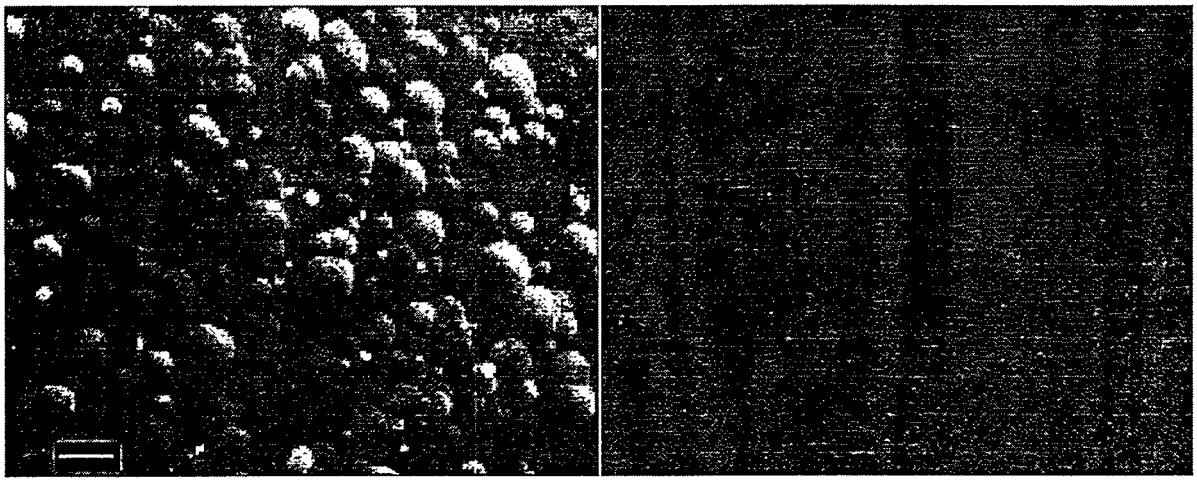

(a) (b)

Fig. 2-12. (a) The surface of a 2 mm PAMs shell coated with 12 μm of GDP in a bounce pan. The surface is covered with domes. (b) A similar PAMs mandrel coated in the rolling pan with 12 μm of GDP. The surface is virtually dome free, while coating thickness was very uniform around the shell. In each case 12 shells were coated together. Scale bar is 10 μm.

marked improvement in the surface finish of rolled shells as compared to gently bounced shells. With the spinning pan agitation scheme we were able to coat over 100 OMEGA size shells with virtually dome free surfaces. The major concern in rolling agitation was the possible non-uniform coating of the shells due to insufficient agitation. We examined this by coating PAMS mandrels with very good average non-concentricity (NC) of less than 5%. The resulting GDP mandrels also had a NC of less than 5% indicating uniform coating of the mandrels in the rolling pan. In addition, when a number of 2.2 mm PAMS shells with a large NC of over 20% were roll coated with 8 μm of GDP, the final GDP shells had a NC of less than 5%. Therefore, the spinning pan agitation did indeed provide sufficient agitation for depositing uniform coatings on shells.

For further information, please contact Dr. A. Nikroo (GA).

2.3. CHARACTERIZATION

Tighter tolerances and increased target delivery rates necessitate the need for new or improved characterization techniques. Some of these development activities are described here.

2.3.1. IMPROVED OUT-OF-ROUND MEASUREMENTS

We have developed a simple way to quickly measure capsule diameter and OOR. We define OOR to be half the difference between the major and minor axes of the best-fit ellipse to a capsule silhouette, *i.e.*,

$$\mathrm{OOR} = (\mathrm{Ellipse}_{\mathrm{major\ axis}} - \mathrm{Ellipse}_{\mathrm{minor\ axis}}) / 2$$

This definition allows us to directly compare our OOR measurements to AFM sphere-mapper traces that measure the variation in capsule radii. Our new method makes use of the NIH (National Institute of Health) free-ware program Image, modified by David Bernat working for GA under a DOE student sponsorship program in FY97.

The Image program measures capsule diameters in two ways. The first way uses a mouse-controlled "line tool." The operator places the computer cursor on one edge of the capsule then stretches a line to the opposing edge. The length of the line is automatically measured and pasted into an Excel spreadsheet. Because the operator has to decide where to place the cursor, measurement precision is set by operator accuracy. Further, the resolution of the line tool is limited by the pixel size of the video camera (~0.5 μm).

Our improved OOR and diameter measurement method makes use of the second tool, the "magic wand." To use this tool, the operator places the wand icon to the left of the capsule image and clicks the mouse. The computer, using image analysis, finds the ellipse that best fits the capsule image. Because the capsule silhouette is two dimensional, the pixel size limitation is greatly reduced. We have improved the resolution further by using a tele-centric, long focal length lens that reduces the focusing error by at least a factor of two.

For Image to accurately measure OOR, it is essential to correct the screen distortion. The Image program does this by using a parameter called the aspect ratio (A.R.) factor, a constant applied to the y-axis measurement to make it agree with the x–axis. Previously, we derived A.R. using a National Institute of Science and Technology (NIST)-traceable micrometer scale. The operator measured a length on the scale with the line tool in the horizontal direction, then in the vertical direction. The ratio between the two measurements gave us A.R., namely,

$$\mathrm{A.R.(old\ method)} = \mathrm{Length}_{\mathrm{vertical}} / \mathrm{Length}_{\mathrm{horizontal}}$$

The accuracy of the old A.R. method was pixel-size limited. We got around this limitation by using the "magic wand" and a NIST-traceable calibration ball certified to have an OOR of <0.1 μm. With the wand tool, the computer measures the ball with the A.R. set to 1.0000. The ratio of the measured minor and major axes gives the true A.R. (a value of 1.0372 is typical for our system).

To measure capsule diameters with our new procedure, we again use the NIST-traceable ball. We set the Image program scale to a previously derived value for the given magnification. This value cannot be exact as the illumination, computer and microscope setup is quite variable. We resolve this problem by keeping the setup conditions constant throughout our measurements.

Maintaining fixed setup conditions, we measure the calibration sphere diameter (D) using the magic wand. To correct for setup variability, the ratio of the computer measured diameter ($D_{measured}$) to the true diameter (D_{true}) is applied to all subsequent measurements on our Excel spreadsheet (*i.e.*, Correction factor = (Cal. Ball Diam.$_{true}$ / Cal. Ball Diam.$_{measured}$). Figure 2-13 below shows the Image Program as it appears on the computer monitor when measuring capsule diameter and OOR.

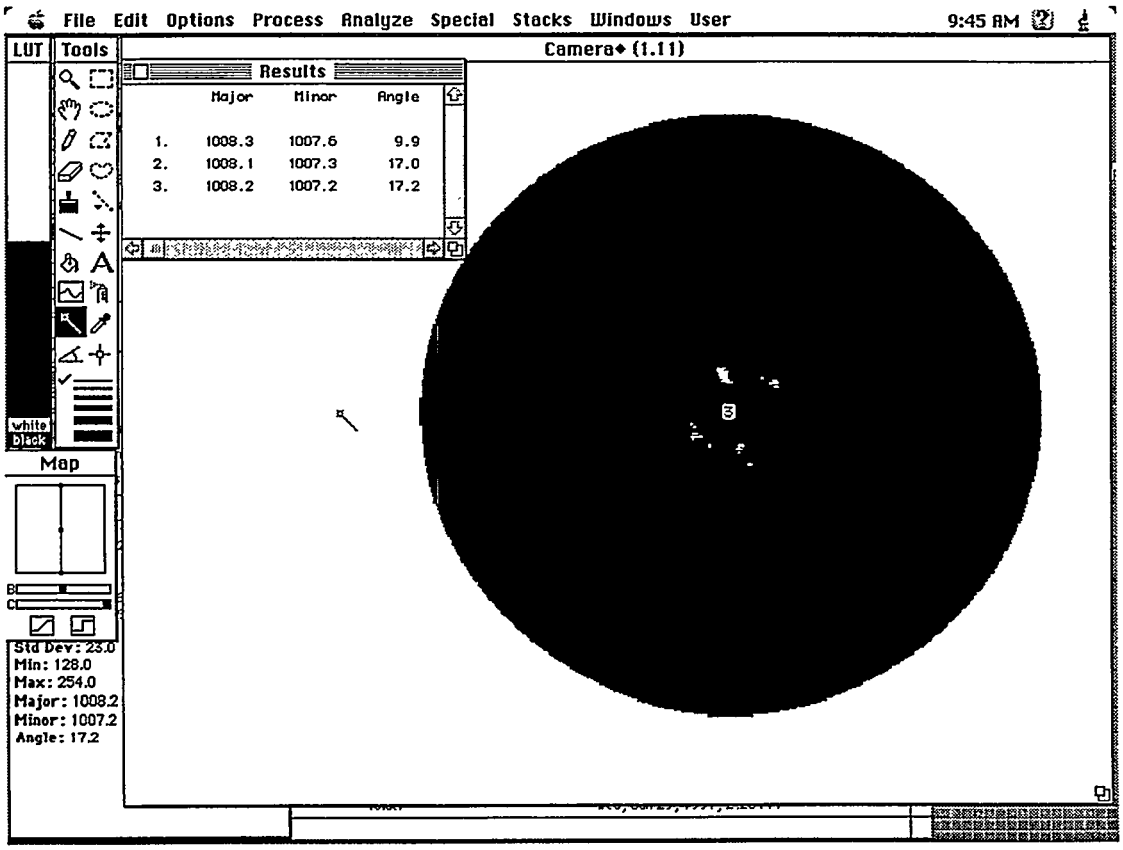

Fig. 2-13. Image program used to measure the diameter of capsules to < 0.1%. and OOR.

To test the efficacy of this technique, a slightly OOR PAMS capsule was secured to a petri dish, then measured in nine orientations. In our nine measurements, the average diameter was 2277.8 μm with a standard deviation of 0.1 μm. The average OOR was 9.4 μm with a standard deviation of 0.3 μm. When measuring capsules of different sizes in a batch, where re-focusing is required for each shell, we find the standard deviation of our diameter

measurement to be consistently under 0.1%. AFM spheremapping confirms that batches of 1 mm capsules measured optically as less than 1 μm OOR are indeed spherical to that degree.

Once the computer and optical systems are set up and calibrated on the NIST-traceable standard, capsule measurements take about ten seconds each. While the computer is measuring one image, the operator can position the next capsule for measurement.

For further information, please contact. D. Steinman (GA).

2.3.2. IMPROVED INTERFEROMETRY

In striving to continually improve the accuracy and efficiency of our interferometric measurement techniques we have tested and adapted a new device for our specific needs. This device is an interferometric z-translation laser stage and is capable of positioning within 0.1 μm over a range of >2 mm. The stage can be translated at speeds in excess of 30 μm per second; slower than 0.1 μm per second; or anywhere in-between. This capability allows for very efficient and precise measurement of capsule diameters and layer thicknesses. Figure 2-14 illustrates the configuration of this interferometric laser stage.

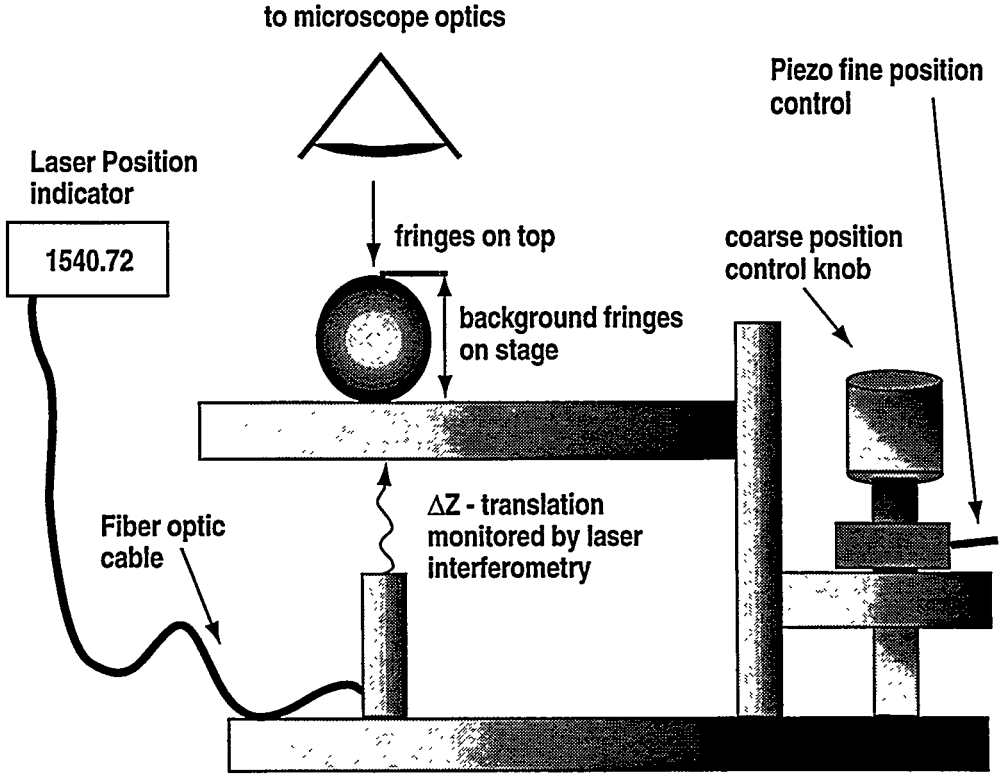

Fig. 2-14. Illustration of laser stage. The z-translation laser stage is capable of positioning within 0.1μm over a range of >2 mm.

Another example of a modification which has allowed us to make measurements more accurately than before is depicted in Fig. 2-15. The image on the left shows the appearance of fringes through a thick-walled (~100 μm) GDP coated glass mandrel which has been filled with helium. In order to determine the fill pressure, one must be able to locate the position of the most intense fringe. This is not readily accomplished when there are a large number of fringes of about equal intensity. However, by modifying the interferometer by inserting a glass coverslip into the reference beam path which results in a closer match between the dispersion in the reference and sample paths, identification of the most intense fringe is made much more easily.

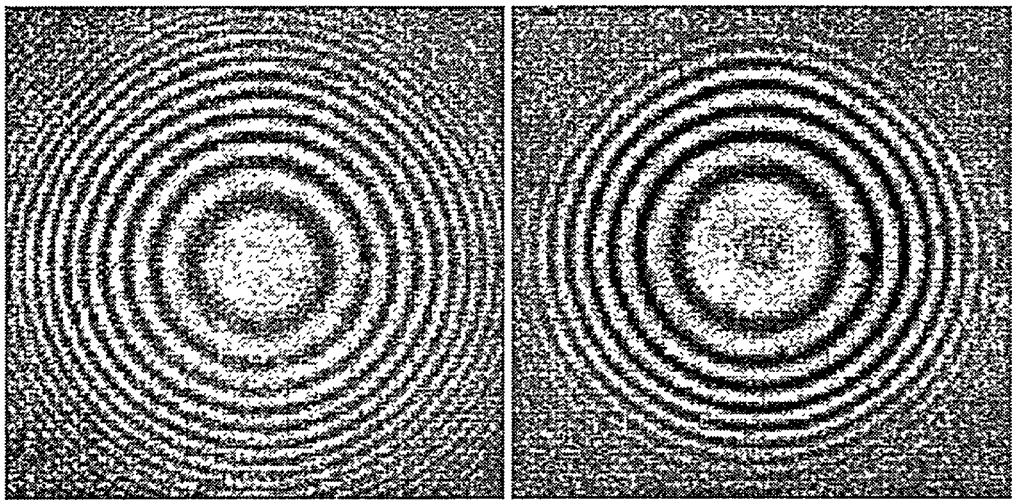

Fig. 2-15. (a) Appearance of fringes through thick-walled GDP coated glass mandrel without addition of coverslips in reference arm of interferometer. (b) Appearance of fringes through thick-walled GDP coated glass mandrel with addition of coverslips in reference arm of interferometer.

For further information, please contact Dr. M. Hoppe (GA).

2.3.3. ADVANCES IN XRF CALIBRATION AND ANALYSIS

The objective of our x–ray fluorescence analyses is to determine dopant concentrations in composite shells to within ~10%. At the beginning of FY96, we had calibrated the XRF carefully for argon, chlorine and, using the Cl in various chlorides as a secondary standard, for Si, Ge, and Ti. For Ar-filled shells and CH-coated Cl-PS shells, we had developed empirical equations to correct for signal attenuation. For all other structures, we corrected for signal attenuation with a program written in PVWave and running on a Sun workstation. The program was rewritten to accommodate every new shell structure. Our accuracy was probably within 10% so long as the shells were not very thick or complicated, and the signals were

strong. In FY97 we began a program of upgrading to give us the capability to handle new dopants, new shell structures, and strong attenuations/weak signals, and to improve our accuracy. To that end, we rewrote our modeling routine into a general purpose program which runs on the laboratory Macintosh computers, we developed more accurate ways to calibrate the system, and we improved signal handling at low levels. At the end of FY97 we can deal with shells doped with multiple high-z elements in arbitrary configurations, we have the calibrations for Si, Ge, Ti, and now Mo on a much more solid basis, and we can add new elements to our roster quickly and accurately. In the next sections we describe the new calibration scheme, the computer modeling application, XRFer, and its reality checks.

Original XRF Calibration. The original calibration of the XRF instrument for chlorine was achieved by using shells manufactured from chlorinated polystyrene which were then chemically analyzed by combustion analysis at Galbraith Labs.

Calibration of the XRF for the remaining dopants was achieved in two steps. A preliminary calibration was obtained by correlating the analyte (A) signal of interest (A = Si, Ge, Ti) to the Cl count ratio obtained in a thin film of material which has a precisely known A/Cl elemental ratio (typically a chloride suspended in plastic).

After the preliminary calibration was complete, the calibration was refined by comparing XRF and combustion analyses of doped capsules. The example below illustrates this procedure:

- PAMS mandrels were coated stepwise with Si doped GDP and characterized at each step for Si content via XRF to confirm that the Si content was not changing during the coating process.

- After the coating process and XRF analyses were complete, the Si-GDP coated mandrels were sent to Desert Analytics for chemical analysis (Table 2-3).

XRF Calibration Using Metal Foils. During the past year we have switched to using flat metals foils whenever possible for calibration: XRFer, with its more precise attenuation correction has allowed accurate calibration with flat films even in the presence of attenuation. As a result we need not prepare a large number of doped capsules for combustion analysis. All that is required experimentally now is the XRF sensitivity factor for an element. The sensitivity factor is defined as the x-ray counts per second per atom of analyte as measured by the XRF system in the absence of attenuation effects. The XRF sensitivity factor is obtained quickly and accurately from pure metal foils (where available). Attenuation corrections are relatively simple for that geometry. The requirement is only that the foil be small enough to be immersed fully within the x–ray beam. For any given excitation energy, the detected fluorescence is given by:

TABLE 2-3
COMPARISON OF COMBUSTION ANALYSIS WITH XRF RESULTS*

Combustion Analysis:				
%C	%H	%N	%Si*	%O
68.31	9.1	0.88	16.82	4.9
			(*by difference)	
Comparison [Si] (g/cc)				
XRF	Combustion		H/(Si+C)	
0.25±0.025	0.24±0.015		1.56	

*Comparison of Desert Analytic's combustion analysis with XRF results. For combustion analysis, the Si concentration was determined by subtraction, since all the other elements were successfully measured. For XRF, the model used in the calculation included the O and N observed in the combustion analysis. H/(Si+C) is included in the comparison as a reality check.

$$I(E,d) = I_o(E)\frac{\alpha(E)}{\alpha(E)+\beta(E_f)}\left(1-e^{(-(\alpha+\beta)\rho d/\cos\theta)}\right) \qquad (2\text{-}2)$$

where d is the film thickness, $\alpha(E)$, $\beta(E_f)$ are the absorption strengths of the incident and fluorescent x-rays, respectively, ρ is the foil density, and θ is the angle of incidence and emission.

With a Mo filter, the incident spectrum may be approximated as mono-energetic (see Fig. 2-18) and one can fit the fluorescence as a function of film thickness with Eq. (1), and α = 34 cm^2/gm, β = 111.4 cm^2/gm, ρ = 4.507 g/cc (Fig. 2-16).

XRFer Operation. The basic structure of XRFer was described in GA's ICF 1996 Annual Report. At that time it ran only in PVWave on a remote Sun workstation, and had to be substantially rewritten to accommodate every new problem. It became obvious, as we began to use it, that the program had to be much more readily available to the XRF operators, both in running in more convenient locations, and with a more flexible interface. With that in mind, it was rewritten in FY96 as a Macintosh application which could run on a Power PC, and was given a flexible operating interface that did not restrict its power (Fig. 2-17).

In addition, with the adoption of thick flat films for elemental calibration, it became necessary to account for absorption effects in a flat layer geometry, so flat layer capabilities were being added to XRFer at the end of FY97. This new routine uses Eq. (2-2) summed over all the energies in the excitation spectrum.

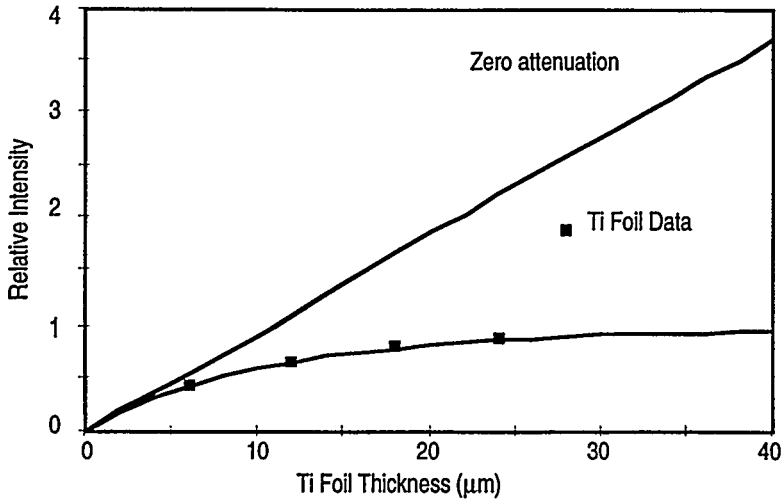

Fig. 2-16. Ti Kα x-ray emission intensity as a function of foil thickness. The straight line is that expected in the absence of attenuation. The data follow a curve defined by Eq. (2-2).

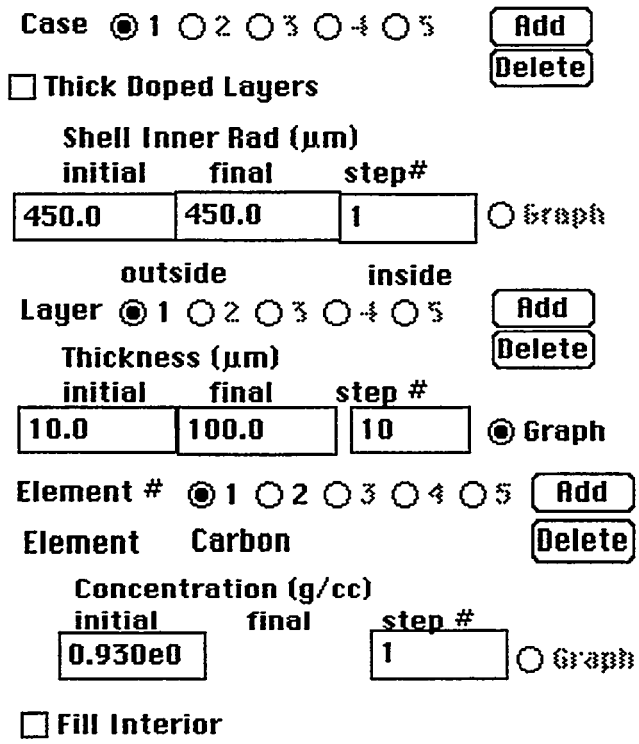

Fig. 2-17. XRFer layer dialog. The user can specify up to five different sets of shells to be calculated in a batch. For each set, the shell can have up to five layers, each layer with up to five elements, and the interior void of the shell can also be filled. Any of those components can be specified to have a range, and the program will calculate the fluorescence counts for every possible combination of the elements specified. The results can be graphed against any of the varying parameters, and the results, and parameters used to calculate them, can be saved to an Excel text file. A separate dialog is used to specify the x-ray tube voltage, tube filters, and fluorescent element choice.

XRFer Checks. We have checked the performance of XRFer in a variety of ways: verified the underlying x–ray absorption data base, experimentally checked the calculated tube emission spectrum, and compared predicted and experimental signal attenuation for our most sensitive cases. At this point we believe that XRFer can be used to calculate the concentration of a fluorescing element to within ~10%, if the shell geometry, and the other elements are properly accounted for.

The data base is the easiest to check. XRFer uses a database of the energy dependent x–ray absorption for each element to calculate the attenuation of the incoming x–ray excitation spectrum and the outgoing fluorescence signal. To save space, analytic fits to the data are stored in the form of coefficients to the equation:

$$\ln(a) = \sum_{i=0}^{4} A_i (\ln E)^i \tag{2-3}$$

Coefficients are determined for every absorption mechanism: elastic and inelastic scattering, and the various shell excitations. These coefficients were derived from a 1969 x–ray absorption study [2-6] which for some elements and energies, did not have much data. Their data is in excellent agreement with the current LLNL data base, but the coefficients used in their fits, it turned out were often poorly chosen. The current version of XRFer uses coefficients which have been modified to fit the data within a few percent, except at complicated band edges.

The tube emission is more complicated, but is also under good control. The emission is the sum of bremsstrahlung and characteristic radiation. Again, to save space, the variation of each with tube energy is calculated analytically. Comparison of calculated and measured tube emission at V = 40 kV shows good agreement (Fig. 2-18). Comparison of predicted and measured Ti counts as a function of tube voltage showed a systematic variation of ~30% (independent of tube filter) in the face of count rates changing nearly 100 times (Fig. 2-19). We virtually always use the XRF at V = 40 kV, so this variation is acceptable.

The algorithm for the attenuation correction is the hardest part to verify. We chose to study the dependence of fluorescence counts on CH overlayer thickness of chlorine and silicon; the two elements we use with the lowest fluorescence energy and thus the largest attenuation correction. For each element, we measured the response to two different excitation spectra: Mo filter, and Mylar filter. The latter has a low energy component in its excitation spectrum which we expect to be substantially attenuated by the CH overlayer. You can see in Fig. 2-20 that the predicted and actual fluorescence counts are nicely proportional. The scatter in the data for the Mo filter and Cl fluorescence is primarily from count uncertainty. The uncertainty for the others is primarily from limitations in measuring shell dimensions.

For further information, please contact Dr. R. Stephens or Dr. M. Hoppe (GA).

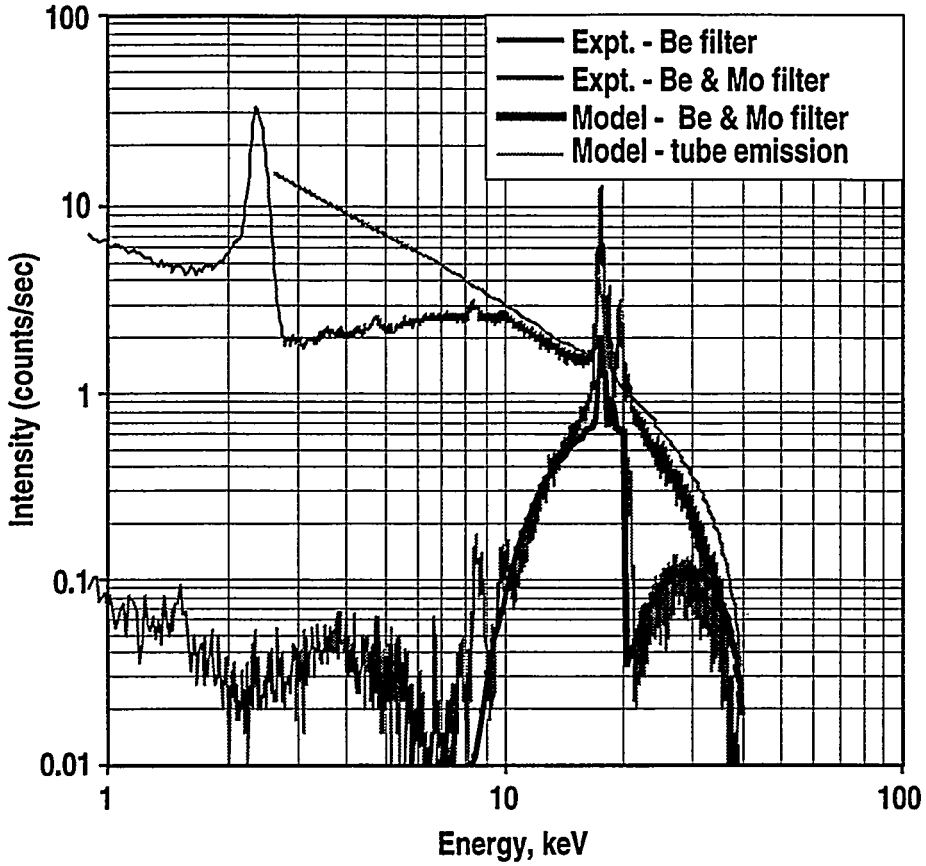

Fig. 2-18. Comparison of calculated and observed excitation spectra as a function of filter, using a Mo anode at 40 kV. The incident spectrum may be considered mono-energetic since nearly all the energy is between 15 and 20 keV.

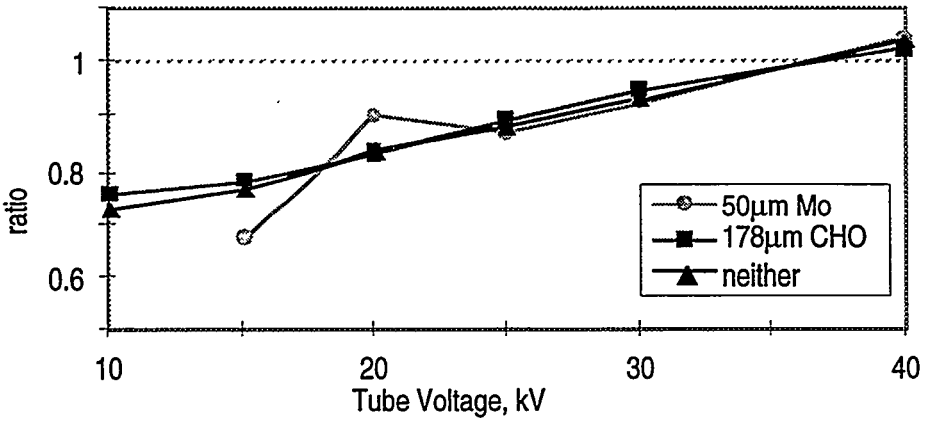

Fig. 2-19. Ratio of predicted to observed Ti fluorescence counts for a single Ti containing target as a function of tube voltage and filter.

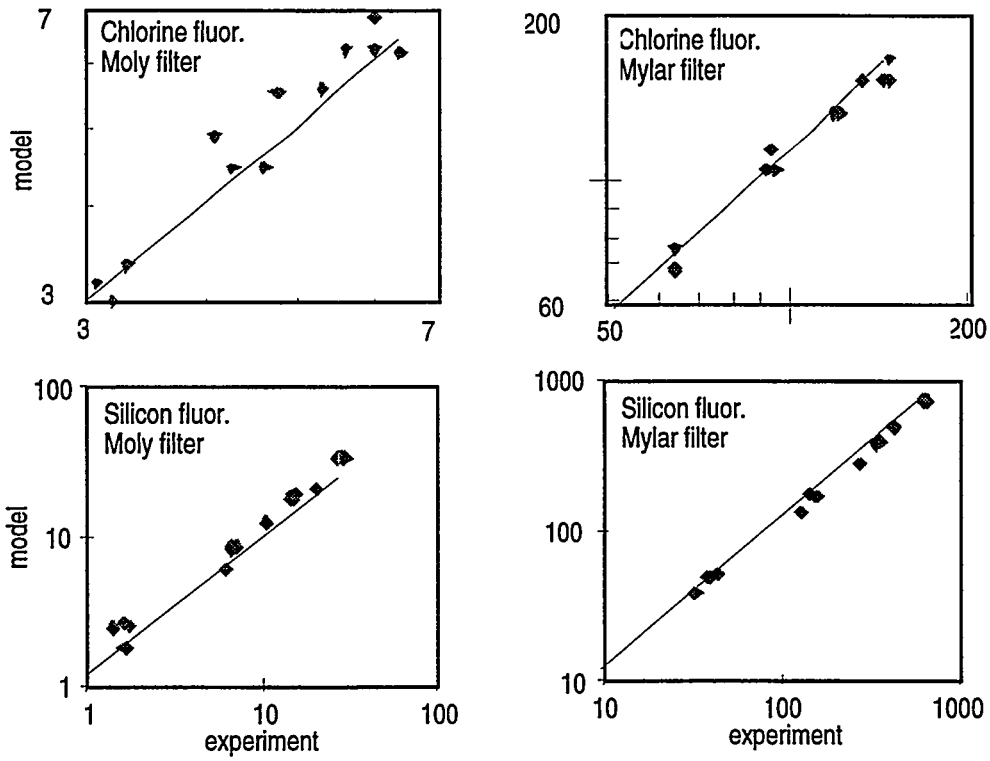

Fig. 2-20. Comparison of fluorescence counts predicted by XRFer and measured experimentally as a function of CH overlayer thickness. The measurements were done with two different tube filters (50 μm thick Moly or 178 μm thick Mylar), and for two different fluorescing elements.

2.4. REFERENCES FOR SECTION 2

[2-1] A. K. Burnham, J. Z. Grens, and E. M. Lilley, J. Vac. Sci. Technol. A **5**, 3417 (1987)

[2-2] ICF Target Support Annual Report, 1996, General Atomics Report GA-A22549 (February 1997), p 1-6.

[2-3] B. W. McQuillan, A. Nikroo, D. A. Steinman, F. H. Elsner, D. G. Czechowicz, M. L. Hoppe, M. Sixtus, and W. J. Miller, Fusion Technol. **31**, 381 (1997)

[2-4] A. Nikroo, D. Woodhouse, "Bounce Coating Induced Domes on Glow Discharge Polymer Coated Shells," to be submitted for publication to Fusion Technology.

[2-5] M. Saculla, S. A. Letts, in Proceedings of the 11th Target Fabrication Specialists' Meeting, Orcas Island, Washington (1996)

[2-6] "Compilations of X–ray Cross Sections," Lawrence Livermore National Laboratory Report UCRL-50174-SEC2-R1 (1969).

3. MICROMACHINED TARGET COMPONENTS

In the micromachining task, more than 700 gold plated hohlraum mandrels and more than 200 other components were produced as described in Section 1.2. Most of these components were similar to those produced in previous years on the two Precitech Lathes in the micromachining laboratory. This year the Rocky Flats #3 Lathe was upgraded and brought on line to add to our capability, and a new type of hohlraum with a very thin gold wall supported by a thicker epoxy coating was produced. These two developments are described below.

3.1. IMPROVEMENTS IN MICROMACHINING CAPABILITIES

GA's micromachining capabilities were expanded and improved by upgrades to the Rocky Flats #3 (RF-3) diamond-turning machine which were completed during this fiscal year. The new capabilities are due primarily to the incorporation of new hardware items into the RF-3 system, but are also the result from the development of new procedures and techniques.

3.1.1. HARDWARE UPGRADES

The following items or subsystems were added to RF-3:

Position Encoders: The former diode laser/glass grating encoders on the x and y–axis drives were replaced with gas (He-Ne) laser/interferometer encoders which are more precise, stable and much less subject to failure due to contamination or noise.

Motion Controller: The former Unidex 31 motion controller was replaced with a Unidex 600 PC-based controller from Aerotech.

Spindle: A vacuum chuck adapter was installed in the block-head spindle. This adapter accepts either a vacuum faceplate which is used for flat-stock, such as witness plates, or a precision three-jaw chuck which is used for round stock, such as hohlraum mandrels.

Tool Holder: The RF-3 system received by GA was a three-axis system, the third axis of which was a block-head spindle fitted with a stepping motor which enabled the orientation of the single cutting tool to be varied. This motion axis was removed and replaced with a fixed-axis table that accommodates two tool holders, as is required for production of mandrels having both front and rear features, *e.g.*, laser entry holes (LEHs).

Coolant Mister: A commercial coolant mister, consisting of a coolant reservoir, air pressure regulator, air and coolant flow jets and gooseneck nozzle was installed to provide a steady, continuous jet of air and coolant mist to the tip of the diamond tools, its purpose being to manage the cutting chips and provide smoother surface finishes.

Television Monitoring: A closed-circuit TV camera with zoom lens and monitor allows the operator to have a close-up, real-time view of the cutting operation despite the smallness of the parts and the cramped quarters of the spindle environment.

The first witness plates were produced with the upgraded system in January 1997 and the first hohlraum mandrels were produced in April 1997. The system has been in a production mode since that time. The upgrades have resulted in increased output, greater precision (±0.3 μm), and better surface finish (less than 100 Å rms).

3.1.2. WITNESS PLATE PRODUCTION METHODS

Witness plates are typically small (1 to 6 mm) rectangles of aluminum with flat, stepped, or tapered profiles. Their thickness can vary from 50 to 500 μm, with a tolerance of ±5 μm. They are produced in two steps: first, a diamond turning machine is used to produce the desired thickness profile in an annular region of an aluminum disc, then a diamond fly-cutter or a small mill cutter is used to dice up the annular regions into rectangles to make the finished witness plates.

Since the diamond turning step is the one that must produce the required thickness accurately, it is crucial that the location of the back surface of the aluminum disc be known precisely when the profiles are cut in the front surface. In machining parlance, this means that the operator must be able to "touch-off" the cutting tool on a reference surface that is precisely indexed to the back surface of the disc, since that latter surface itself will be inaccessible.

The original "Rocky Flats" method of accurately machining the profile of witness plates is to first diamond-turn the front surface of a plastic or polycarbonate disc which is glued to a thicker aluminum disc which is held in the vacuum chuck. The composite disc is then placed in a vacuum coater and aluminum is evaporatively coated onto the plastic through a mask which protects the outermost few millimeters of its surface. When the composite disc is returned to the diamond turning machine, this protected area defines the back surface of the deposit and is used for the subsequent touch-off which establishes the depth-location of the diamond cutting tool. The profile is then machined and the milling operation performed, after which the plastic is dissolved to release the individual witness plates.

The "Rocky Flats" method proved to be cumbersome because of the vacuum deposition step, which was time consuming and unreliable, due to equipment breakdowns. The "GA"

method (outlined in Fig. 3-1) was developed to circumvent the vacuum processing step, while still maintaining a reference surface for the touch-off step. The initial aluminum disc is usually 1 or 2 mm thick and can be any grade of aluminum required by the experiment, *e.g.*, 6061-T6, 1100, or 99.999% Al; it is held on the vacuum faceplate of the diamond turning machine, trued with rough cuts and finished turned to produce a smooth surface of high optical quality. It is then turned over on the face plate and the other side is similarly prepared, as indicated in step 2. The thickness of the resulting disc is measured in a traveling microscope and recorded.

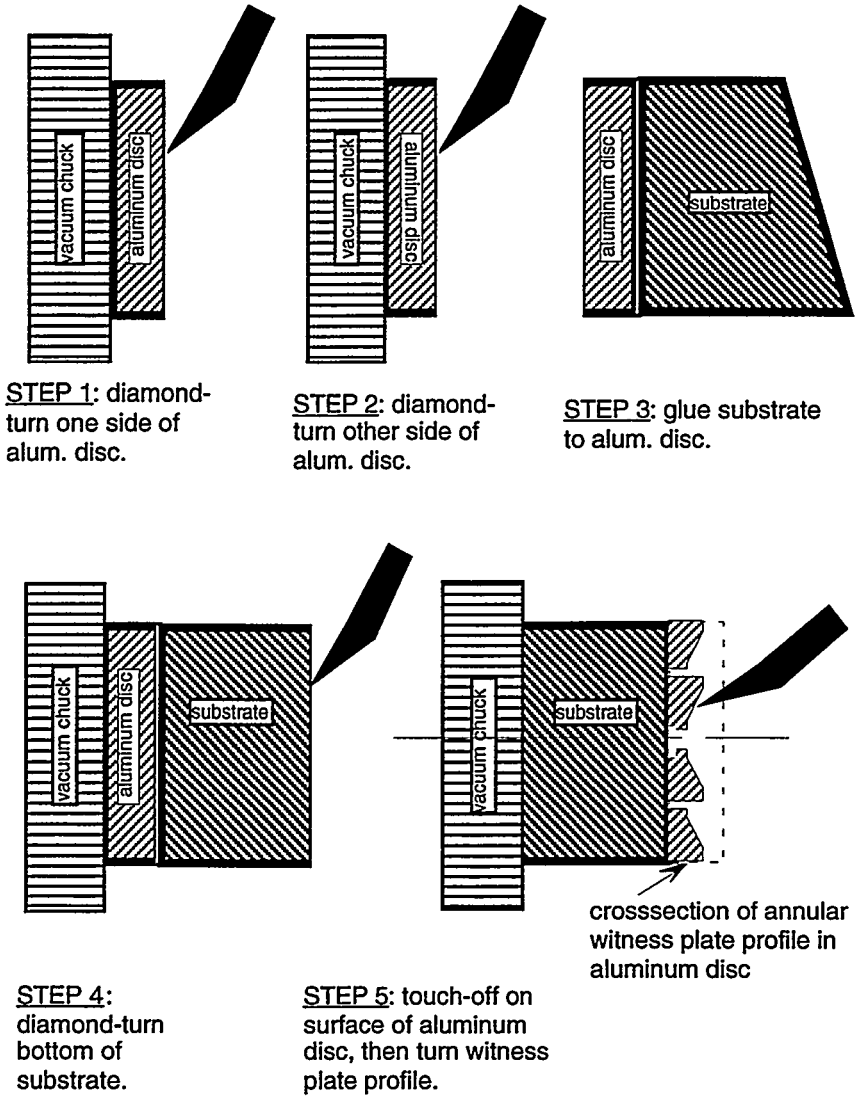

Fig. 3-1. Steps in the "GA" method of witness plate production. The original aluminum disc is 1 to 2 mm thick. Between steps 4 and 5 it is cut down to about 0.5 mm in an ordinary lathe.

In step 3 the disc is glued to a much thicker disc which serves as a substrate; cyanoacrylate, aka "superglue," is the adhesive that is employed. The substrate need not have parallel faces at this stage, as suggested by its trapezoidal shape in the figure, nor does care have to be taken to

assure that the glued surfaces are parallel. The required parallelism between the witness plate surfaces and the vacuum chuck is assured by the cut made in step 4.

Between steps 4 and 5 the composite disc is mounted in a Hardinge lathe and the disc is cut down to about 1/2 mm, taking care to leave a rim of the original thickness measured in step 2 untouched. In step 5 the diamond tool is touched off on this rim and the total depth of cut required to reach the desired witness plate thickness and profile is determined on the basis of the overall thickness measured after step 2.

After step 5, the dicing operation is performed and then the composite disc is soaked in nitromethane with ultrasonic agitation until the individual witness plates float free from the substrate. Each of them is measured for thickness, dimension and optical appearance before acceptance, packaging and shipping.

3.1.3. PARTS PROGRAMS

Several parts programs designed to guide the tool motions during cutting operations were written for the new AEROTECH PC-based motion controller that was one of the upgrade items added to the RF-3 system this fiscal year. The generic mandrel programs are listed in Table 3-1 and the generic witness plate programs are listed in Table 3-2. In addition to controlling the motion of the tool relative to the part, the mandrel programs perform several internal calculations: based on the rough and final dimensions of the part that are manually entered, the program calculates the total amount of material to be removed from each face (the "selvedge"), the number of repetitive cuts to be made based on a specified maximum allowable depth of cut (DOC), and the resultant DOCs on each face of the part. In addition, the SPRCHKR program calculates the taper angle, which is determined only by the linear dimensions specified by SNL, but which must be employed explicitly to define the tool path target points.

TABLE 3-1
GENERIC MANDREL PROGRAMS WRITTEN FOR THE ROCKY FLATS #3 MACHINE.

Program Name	MAND1	MAND2	MAND3&4	SPRCHKR
Basic shape*		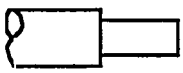	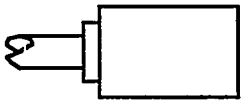	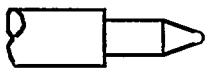
Number of lines	260	92	175	165
Taper correction	no	yes	yes	no
Internal calculations	yes	yes	yes	yes

*In each shape, the left-hand-most cylindrical portion shown is the so-called stem of the mandrel, and is not diamond-turned.

TABLE 3-2
GENERIC WITNESS PLATE PROGRAMS WRITTEN FOR THE ROCKY FLATS #3 MACHINE.

Program name	WITPLT4	TARGPLT
Number of different profiles	4	1
Type of profiles	2-tapered 1 stepped 1 flat	3 steps in single cut
Number of lines	100	45

In addition to the programs shown in the tables, much shorter programs have been written to perform single facing cuts and mandrel cuts, and are used for set-up and diagnostic purposes; they aren't described separately in this report.

For further information, please contact Dr. Joe N. Smith, Jr. (GA).

3.2. THIN-WALLED HOHLRAUMS

Late in FY97, we received a request from LLNL to produce a batch of thin-walled hohlraums. Thin-walled hohlraums are so named because the gold wall is 2 μm thick rather than the usual 25 μm thick. An epoxy coating of differing specified thicknesses on the barrel, the faces and the flat is used to support the 2 μm gold wall. To produce these hohlraum mandrels, it is necessary to:

1. Micromachine the copper mandrel including machining of a flat on the mandrel.
2. Remove the mandrel from the diamond turning machine.
3. Plate the mandrel with the thin gold coating by electroplating.
4. Coat the mandrel with epoxy by dipping.
5. Heat treat the mandrel at 200°C to ensure full hardening of the epoxy.
6. Return the mandrel to the diamond turning machine.
7. Micromachine the coated mandrel to produce the specified epoxy thickness on the barrel, the faces and the flat.

Returning the mandrel to the diamond turning machine and having it run true without any wobble is difficult. In order to do this a special fixture, patterned after an LANL concept, was designed, fabricated and employed. A schematic drawing of this fixture is shown in Fig. 3-2, and a photograph of the fixture is shown in Fig. 3-3. Each mandrel has a small flange attached to it throughout the production sequence This flange is held flat against a machined surface of the fixture by compression of a strong spring. This ensures that the centerline of the mandrel is

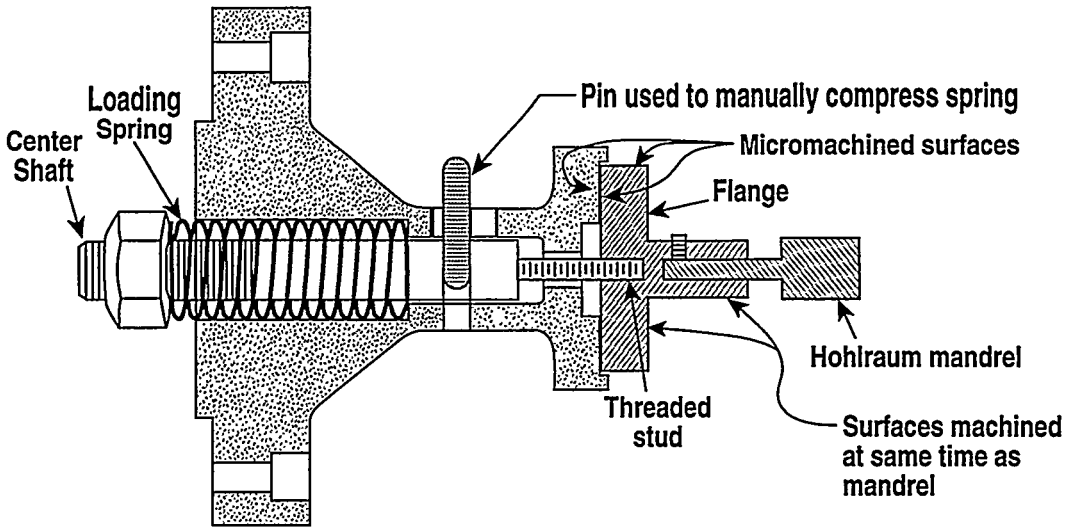

Fig. 3-2. Schematic drawing of the fixture for holding hohlraum mandrels on the diamond turning machine.

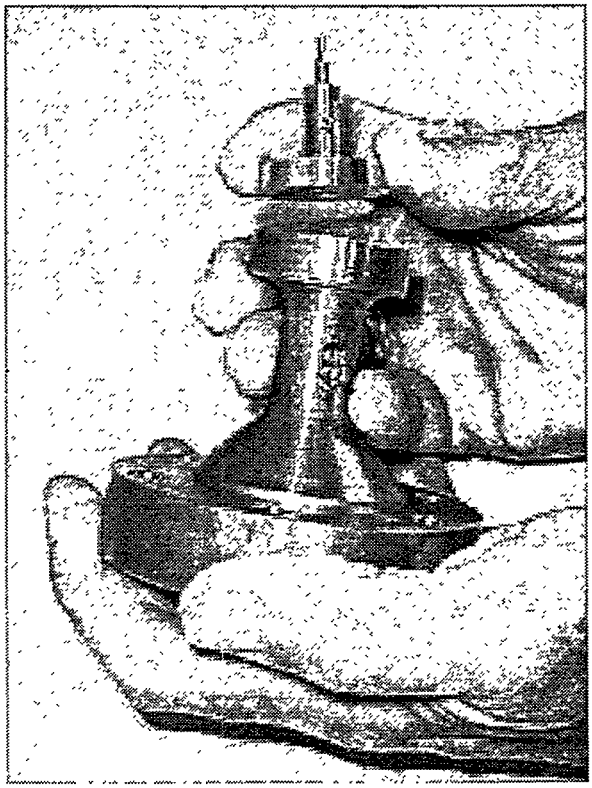

Fig. 3-3. Photograph of the fixture that holds the hohlraum mandrels on the diamond turning machine. A flange remains attached to each mandrel through out the production sequence and allows for very precise realignment of the mandrel when it is returned to the turning machine.

parallel to the centerline of rotation. To make the centerline of the mandrel coincident with the centerline of rotation, a very accurate indicator is placed on a surface of the flange machined at the same time as the mandrel and eccentricity in the rotation is removed by tapping it lightly.

(The center shaft of the fixture is moveable although the spring makes the movement stiff.) The position of the flat on the hohlraum mandrel is recovered by lining a scribed line on the flange with a scribed line on the body of the fixture.

Using this fixture, we were able to fabricate a set of 26 thin walled hohlraum mandrels to satisfy the request by LLNL. The dimensions and coating thicknesses of these mandrels are listed in Table 3-3. Five of these hohlraum mandrels were delivered in the last month of FY97, and the remaining 21 were delivered in the first month of FY98.

TABLE 3-3
DIMENSIONS AND COATING THICKNESSES OF 26 THIN WALLED HOHLRAUM MANDRELS DELIVERED TO LLNL

Mandrel	(mm)
Barrel Diameter	1.6
Barrel Length	3.0
LEH Diameters	1.2
Radii at end of Barrel	0.15
Flat Length	1.1
Flat Width	0.8
Dimensional Tolerances	± 0.005
Gold Coating	
Thickness	0.002
Epoxy Coating	
Thickness on Barrel	0.1
Thickness on Ends	0.025
Thickness on Flat	0.050
Thickness Tolerances	± 0.005

For further information, please contact Dr. J. Kaae (GA).

3.3. LOW-DENSITY FOAMS PRODUCTION AND MACHINING

Subtask D of 97SL01 brought a new production capability to the ICF contract: the production of low density foams in precision geometries. There were three foam systems of interest, resorcinol-formaldehyde (RF), polystyrene (PS) and TPX. (TPX is the commercial designation of the polymer produced by the polymerization of 1-methyl-4-pentene.) All of these foam systems had been developed at the National Laboratories, thus this task was another successful example of technology transfer to the ICF Target Contract. The task statement anticipated the need for approximately forty-six target components, a total of forty seven were delivered (see Table 3-4). Not all of the target components were for actual targets, several

TABLE 3-4
FOAMS DELIVERED ON 97SNL01*

Description	Foam	Density	Geometry	Quantity	Ship Date	Ship to
prototype RF cylinders	RF	50 mg/cc	13 mm o.d., 22 mm length	2	12/24/96	SNL-NM
prototype PS cylinders	PS	40 mg/cc	20 mm o.d., 50 mm length	1	12/24/96	SNL-NM
prototype TPX disks	TPX	***	70 mm o.d., 30 mm length	2	12/24/96	SNL-NM
prototype PS, 1 cylinder 2 annulus	PS	40 mg/cc	4 mm o.d., 0.4 mm wall	3	3/12/97	SNL-CA
prototype TPX cylinder	TPX	15 mg/cc	4 mm o.d.	1	3/19/97	SNL-CA
Mo Doped annuli	PS	45 mg/cc	5 mm o.d., 0.45 mm wall, 10 mm length	4	7/17/97	SNL-NM
Mo Doped cylinders	PS	45 mg/cc	3 mm o.d.	3	7/18/97	SNL-CA
TPX cylinders	TPX	15 mg/cc	5 mm o.d., 10 mm length	4	8/7/97	SNL-NM
TPX cylinders	TPX	10 mg/cc	5 mm o.d., 10 mm length	4	8/7/97	SNL-NM
TPX cylinders, low density prototypes	TPX	7.5, 6.5 mg/cc	5 mm o.d., 10 mm length	4	8/7/97	SNL-NM
TPX cylinders	TPX	10.5 mg/cc	4.7 mm o.d., 9.0 mm length	1	8/13/97	SNL-CA
Mo doped annuli	PS	45 mg/cc	5 mm o.d., 0.45 mm wall, 10 mm length	6	9/4/97	SNL-NM
TPX cylinders	TPX	<10 mg/cc	8 mm o.d., 10 mm length	12	9/16/97	SNL-NM

*Foams delivered to the SNL California facility were characterization samples for ion microtomography analysis.

were validation pieces used to confirm the ability of contract personnel to produce the quality required by SNL. The foams were characterized as to weight, dimensional tolerances and density uniformity. Density uniformity was done by SNL using ion microtomography [3-1].

The first foams listed in Table 3-4 were resorcinol-formaldehyde aerogel cylinders. These foams demonstrated our ability to cast RF to net shape, but we were unable to make the requested target: an annulus 16 mm o.d., 14 mm ID 20 mm length, density of 20-25 mg/cm^3. Using the chemistry developed at LLNL for producing dimensionally stable microencapsulated RF shells [3-2], we were able to cast to dimensions, but the foam densified during the CO_2 supercritical drying. We requested a change in the specifications: double the density but halve the wall thickness to yield the same amount of polymer in the wall. SNL instead canceled the request, partially due the high quality of the foam components made from the TPX and polystyrene systems.

TPX foam was the second type of foam requested by SNL. This foam had been researched by LANL [3-3], and transferred to Oak Ridge National Laboratory (ORNL) for production. However, the Oak Ridge Facility is no longer interested in producing foams. Using the published reports from both facilities, we were able to assume the foam production. TPX foam is produced by dissolving (with heat) the polymer in a solvent, then cooling to precipitate the polymer, cooling further to solidify the solvent, and extracting the solvent by sublimation (freeze drying). The solvent is a blend of durene (1,2,4,5-tetramethlybenzene) and naphthalene. This blend has three very desirable attributes: it has reduced crystalinity, it is a solid at room temperature, and it can be machined. The quality of the foam is determined by the cooling rates. The cooling rate during the polymer precipitation should be slow to yield a small cell foam, and the cooling rate during solvent solidification should be very much faster to prevent crystal formation. SNL was very generous and loaned the GA/Schafer team a computer controlled oven. The first TPX foams we produced had very large cell size, but with adjustments to the temperature program we were able to produce very acceptable foams, as shown in Fig. 3-4. We did institute one change in the published procedures. We are machining precision molds, and then casting the TPX in the molds. As the molds are reusable, this results in considerable labor savings and shortens the lead time needed to produce the required number of foam components.

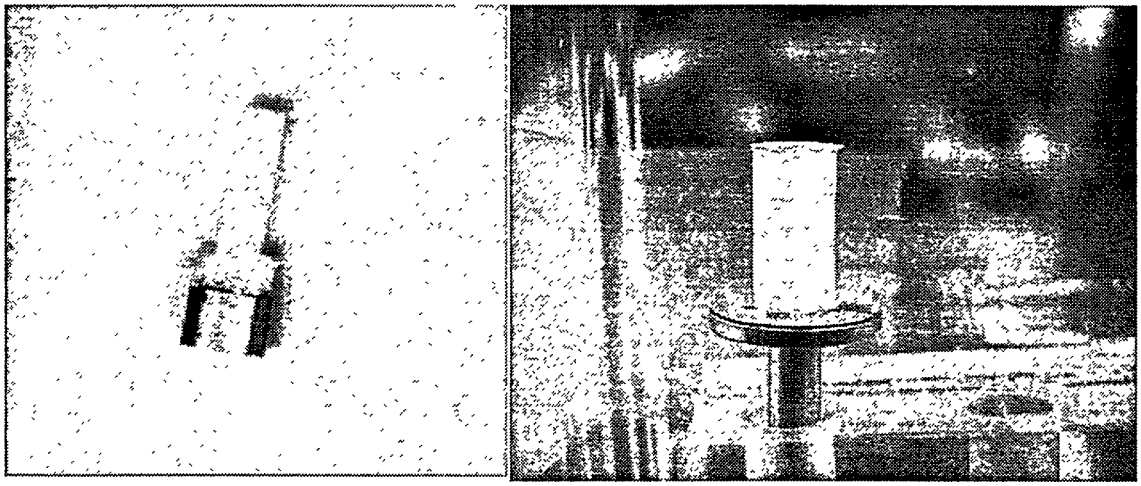

Fig. 3-4. The improvement in TPX foams. The foam on the left was an early TPX foam machined to the proper shape, but the large cell size within the foam caused large density variations. The foam on the right was produced after we adjusted the cooling rate.

The third foam system requested was polystyrene. This foam was originally reported by Unilever Laboratory [4-4], but LANL [4-5] with collaboration from LLNL, was able to optimize the quality of the foam. The foam is produced from an emulsion in which styrene and divinyl benzene are polymerized in the organic phase. The cell size of the foam is set by the emulsion. Results to date indicate the finest emulsion is made by a "push-me-pull-you" syringe pump. We attempted to both mold and machine PS, but the ion microtomography

characterization indicated that machining produced less surface deformation, see Fig. 3-5. This has caused us to produce all target component by machining to tolerances, but we hope in the future to refine the molding technique.

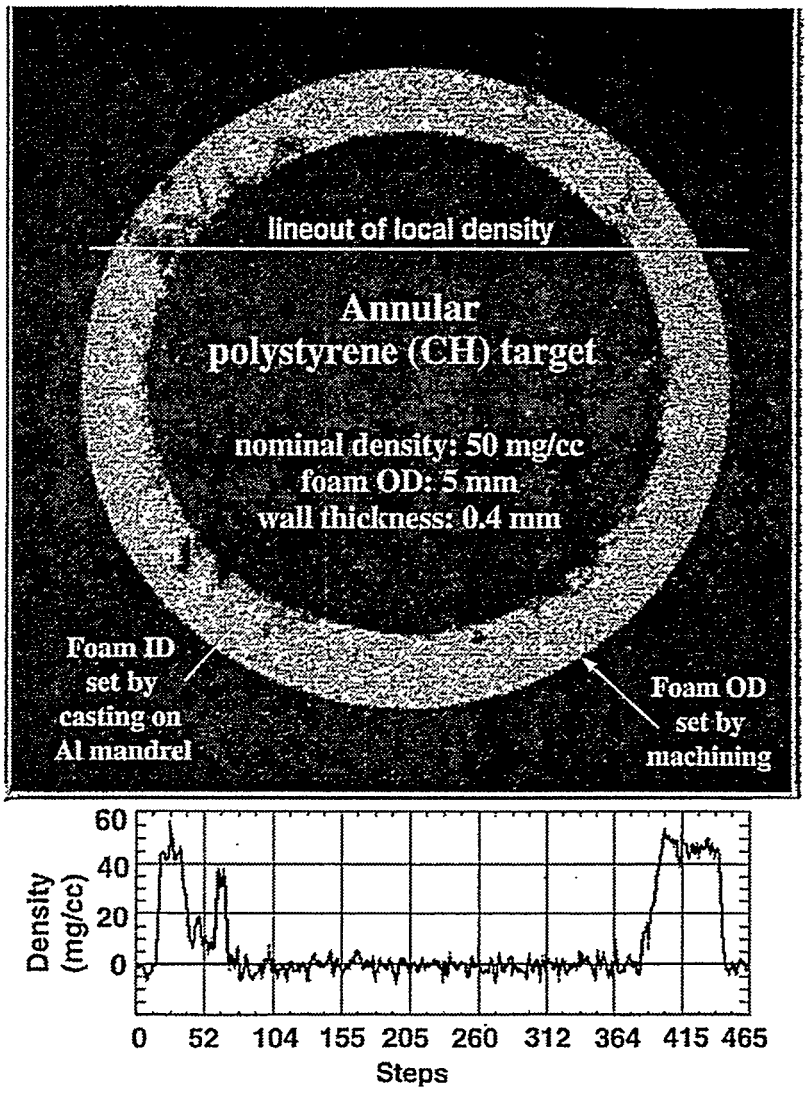

Fig. 3-5. Ion microtomography characterization of a PS annulus. The annulus was formed by casting around an aluminum rod, machining the o.d. to the desired dimension, and dissolving the rod in acid. Analysis clearly showed that machining produced the superior surface finish.

After we had produced PS annuli, SNL made a surprising request. They wanted the foam doped with molybdenum and needed the annuli delivered in five weeks. Since this time frame precluded the synthesis of a molybdenum monomer, we decided to try doping the PS foam by incorporating particles into the organic phase. This method was analogous to the incorporation of pigment in water based paint. The particulate and the surfactant were made into a slurry, the slurry was blended into the organic phase, and the organic phase and the water phase were emulsified as usual. The particles used were Mo2C as it was a more chemically stable form of

molybdenum, and it was available in a small particle size (mean diameter 3.8 μm). The resultant foam was as machinable as the typical PS foam, (see Fig. 3-6 for a machined annulus), and provided a strong Mo x–ray diagnostic.

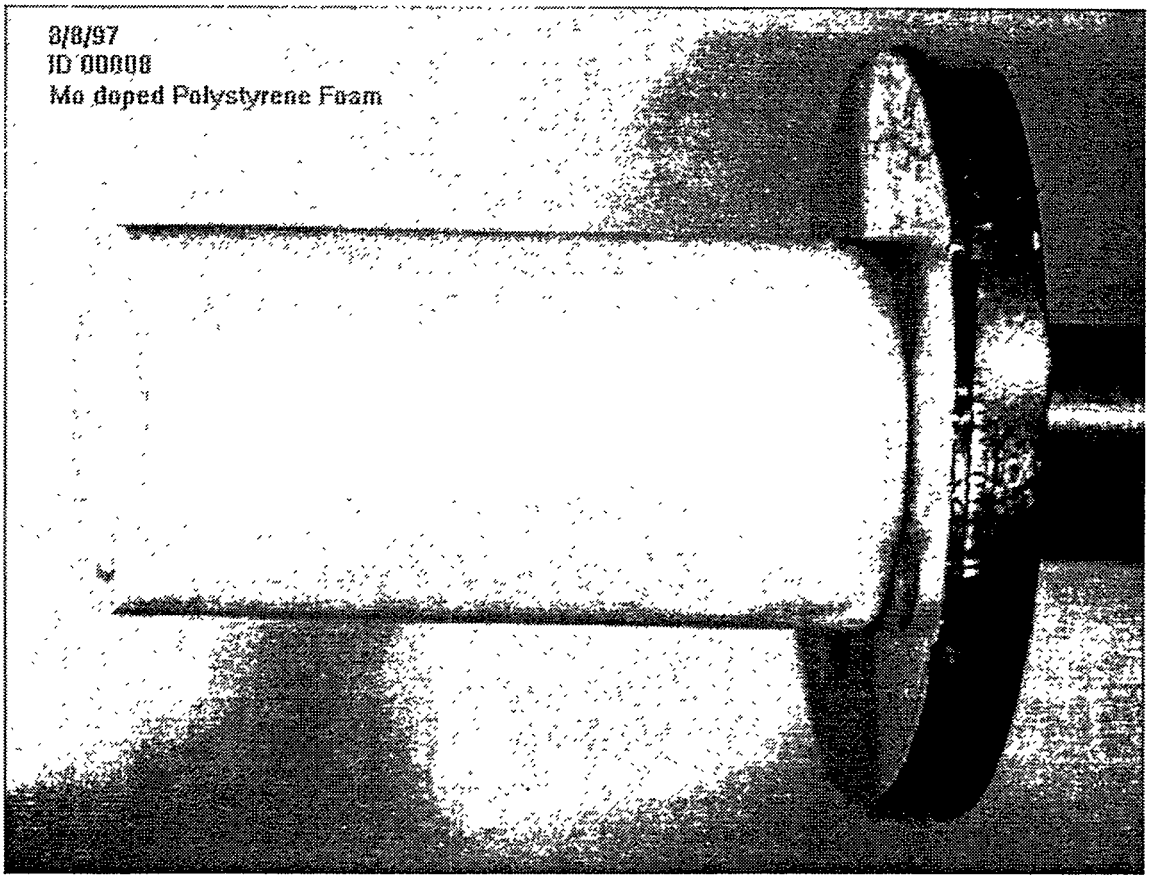

Fig. 3-6. The molybdenum doped foam machined as well as undoped foams. This annulus was 5 mm in o.d., 10 mm in length.

Elemental analysis of the foam, done after the target shot, yielded a disappointing result. The foam had only 1/3 the expected doping level. Density uniformity analysis yielded a very encouraging result, the uniformity was very much better than the particle size would have predicted (see Fig. 3-7). Apparently the technique we used incorporated only the smaller third of the particles. In the future, if SNL requests additional foams of this type, we will simply use an excess of the Mo_2C particles and test the level of doping in the final foam prior to machining the foam to shape.

This task is scheduled to continue in FY98. We expect an increase in the number of foam components, an increase in the complexity of the components, and the possibility of new dopant requirements.

For further information, please contact D. Schroen-Cary (Schafer Corporation).

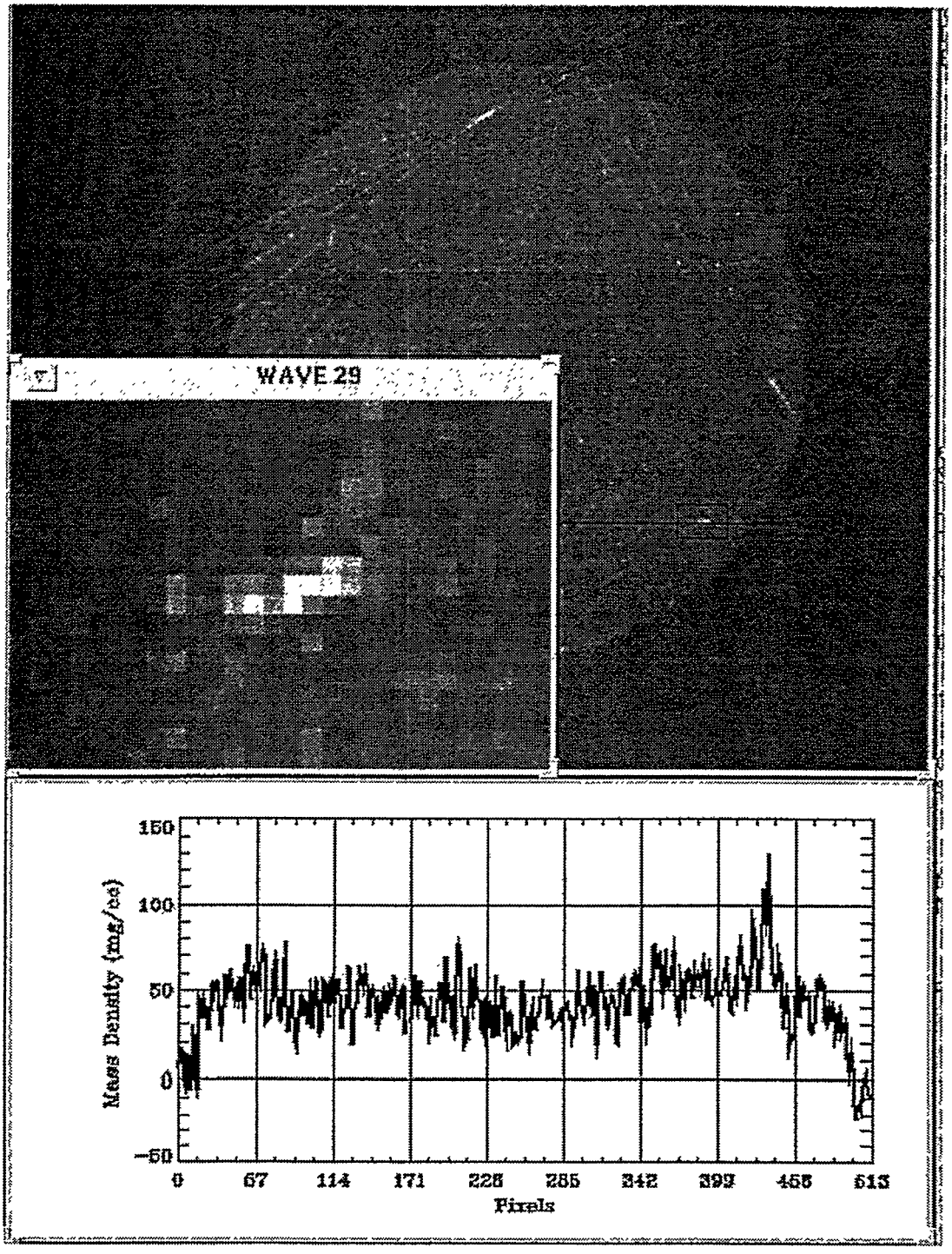

Fig. 3-7. These photos show the results of the ion tomography characterization of a molybdenum doped PS foam cylinder. The large circle is one slice through the cylinder and shows local density variations with high density being represented by a light area. The resolution was set appropriate for particles greater than about 4 μm in diameter. In this scan only one was seen. This high degree of uniformity and absence of large particles supported further characterization which determined we had incorporated only the smaller 1/3 of the Mo_2C particles.

3.4. REFERENCES FOR SECTION 3

[3-1] Ion microtomography done by the Ion Micro-Analysis Group, a joint project of SNL and LLNL in Livermore, CA. The Point of Contact is Arlyn J. Antolak, telephone (510) 294-3363.

[3-2] Schroen-Carey, Robert C. Cook, "Fabrication of Low-Density Foam Shells from Resorcinol-Formaldehyde Aerogel," Journal of Applied Polymer Science, Vol. 65, 2111-2122, (1997).

[3-3] Joel M. Williams, Joyce E. Moore, "Effect of Several Dual Solvents on the Phase Separation of Poly(4-methyl-1-pentene)," Polymer, Vol. 30, 2279-2283, 1989.

[3-4] Unilever Research Laboratory, Emulsion Process for Making Foams, European Patent, 60138 (Sept. 3, 1982).

[3-5] Joel M. Williams and Debra A. Wrobleski, "Spatial Distribution of the Phases in Water-in oil Emulsions. Open and Closed Microcellular Foams from Cross-linked Polystyrene," Langmuir, Vol. 4, No. 3, 656-662, 1988.

4. NR01 AND UR03 TASKS: NIKE TARGET AND OMEGA FLAT FILM IMPROVEMENTS

NR01 Target deliveries to NRL have continued to meet and exceed the rigorous target quality requirements for NIKE Laser research. Over the past year, NIKE target quality specifications have become increasingly stringent as the laser has developed toward full power operation and has achieved unusually high spatial beam quality.

NIKE targets are generally flat polymeric material films mounted on a polycarbonate frame as shown in Fig. 4-1. The film is made by casting a solution of the appropriate polymeric material on a flat or patterned substrate. After the film dries, it is annealed, cut into target-sized pieces, and characterized. The film pieces are then mounted on the frames, characterized again, cleaned, and then shipped to NRL.

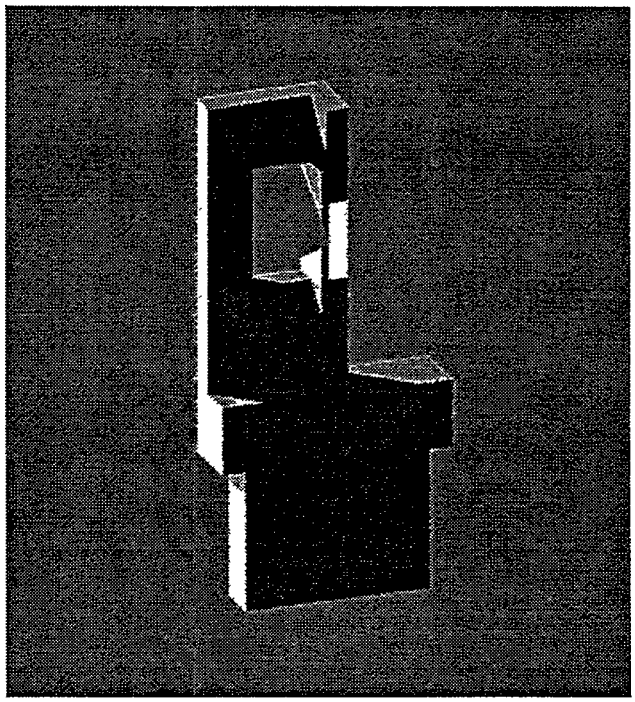

Fig. 4-1. NIKE target mounted on a polymer frame.

Table 4-1 provides a short compendium of some of the general target film specifications for NRL targets:

TABLE 4-1
NIKE TARGET SPECIFICATIONS

Maximum permitted film curvature	1 μm vertical per 1 mm linear horizontal
Surface roughness permitted	5 nm peak-to-valley irregularities
Impurities	Z < 18: As low as possible (less than 0.2%) Z > 18: Less than 0.1% (preferably much lower) Impurities to be characterized to within 5% of impurity level
Volume Quality	Mass integral variations not to exceed equivalent surface variations

While flat targets with two smooth surfaces are still required for the NIKE program, there have been increasing requirements for targets with one flat surface and one perturbed surface. Perturbations include randomly roughened surfaces, sine wave patterns and step-ramp patterns. Usually these patterns are made by casting the film on a fused silica or metal substrate upon which the appropriate pattern has been etched or machined. Figure 4-2 is a photon tunneling micrograph of a sinusoidal surface on a polystyrene target. Some of the most commonly used patterned molds are listed in Table 4-2.

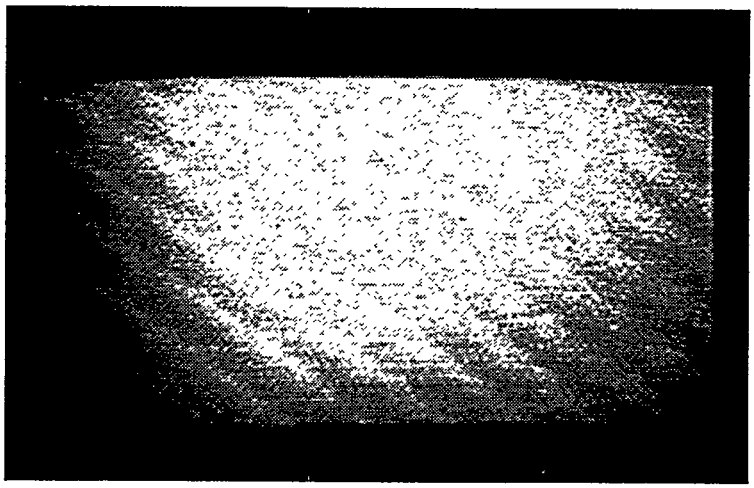

Fig. 4-2. Photon tunneling micrograph of a sinusoidal surface on a polystyrene target. The wavelength of the sine wave is 12.4 μm and the peak-to-valley amplitude is 0.28 μm.

Several types of multilayered targets are produced for the NIKE program. A target with circular symmetry which we produce for NRL is shown in Fig. 4-3. This consists of a circular truncated conical aluminum base on which is mounted in succession, a layer of Kapton film, a layer of aluminum, a layer of low density foam, and finally, another layer of aluminum about 120 nm thick.

TABLE 4-2.
PATTERN MOLDS

Plate Number or Designation	Surface Function	Amplitude (μm)	Wavelength (μm)
2 in. Round Flat	Smooth		
2 in. Square Foil	Flat		
GA1-AL	Sin(r)	1.11	30.0
GA1-Gold	Sin(r)	0.99	61.2
GA2-AL	Sin(r)		
GA2-Gold	Sin(r)	1.00	60.8
GA5	Step-Rmp	14.80	153.0
GA6	Step-Rmp		
GA7	Step-Rmp	10.00	120.0
GA8	Step-Rmp	15.00	122.0
Gentec #01A	Sin(x)	0.25	12.0
Gentec #01B	Sin(x)	0.23	12.0
Gentec #02	Sin(x)	0.14	6.1
Gentec #03	Sin(x)	0.10	60.0
Gentec #04	Sin(x)	0.25	60.0
Gentec #05	Sin(x)	0.10	20.0
Gentec #06	Sin(x)	0.25	20.0
Gentec #07	Sin(x)	0.10	30.0
Gentec #08	Sin(x)	0.25	30.0
Gentec #09	Sin(x)	0.50	30.0
Gentec #10	Sin(x)	0.50	20.0
Gentec #11	Sin(x)	1.00	20.0
Gentec #12	Sin(x)Sin(y)	0.10	30.0
Gentec #13	Sin(x)Sin(y)	0.10	60.0
Glass Plate	Gnd 600 SiC Grit (WJSA)		
Gnd Quartz #3	Ground with 3 mic grit		
Kapton Stretcher	random rough	0.00	0.0
NPL01	Sin(x)	0.94	30.8
Schafer Al#1	Step-Ramp	10.00	60.0
Schafer Al#2	Step-Ramp	10.00	60.0
Wafer, Silicon, Front	Smooth, Flat		
WJSA#1-AL	Sin(r)	0.14	60.0
WJSA#1-Silver	Sin(r)	0.89	64.0
WJSA#2-AL	Sin(r)	0.16	30.0
WJSA#2-Cu	Sin(r)	0.10	15.0
WJSA#3-AL	Sin(r)	0.25	70.0
WJSA#4-AL	Sin(r)	0.22	33.0
WJSA#4-Cu/Au	Sin(r)	0.11	34.2

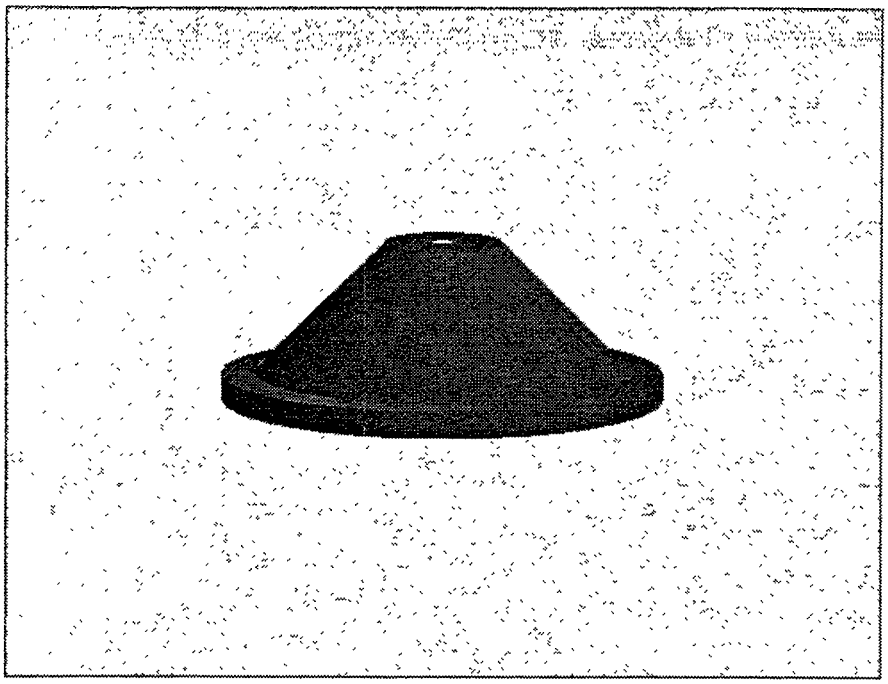

Fig. 4-3. Conical NIKE target.

Additionally, we produced flat targets with layers of pure polymer, aluminum, doped polymer, and aluminum stripes and layers with machined steps.

OMEGA Laser targets are similar in nature and specifications to NIKE targets. The primary difference is that LLE mounts the targets for OMEGA while we mount NIKE targets before we ship them. Consequently, the majority of our deliveries to LLE are unmounted flat foils.

One of our greatest challenges this past year has been finding suitable materials with which to fabricate OMEGA targets. We have no difficulty obtaining high purity, high molecular weight polystyrene used for most of our target films. However, we have been unable to locate a source of highly polymerized silicon-doped polystyrene which is equivalent to the Si-GDP material used to produce spherical shell targets for the OMEGA laser program. The consequence of using a lower molecular weight polymer is brittle or non-cohesive films that crumble into small pieces when they are separated from the casting substrate.

We have experimented with using a sacrificial poly-alpha-methyl-styrene (PAMS) film which replicates the sinusoidal surface pattern of the substrate. Our approach is to make a cast replica of the appropriate pattern using PAMS. We then use the PAMS film as a substrate for forming a Si-PS film. Since our normal method of casting would dissolve the PAMS where it comes in contact with the solvent used to make a solution of Si-PS, we have relied on GA to apply a layer of silicon-doped glow discharge polymer to the patterned surface of the PAMS film. We can then add additional thickness to the polymer film by casting or using an airbrush

technique. After the appropriate thickness is achieved, we decompose the PAMS by heating it. We are left with an intact silicon doped polystyrene film, one surface of which contains the sinusoidal pattern of the original substrate.

In the FY97 year, we have produced and delivered almost 2000 of the various target foils and films, some mounted on target frames and some as free-standing films, to both NRL and LLE.

For further information, please contact C. Hendricks (Schafer Corporation).

5. CRYOGENIC SCIENCE AND TECHNOLOGY DEVELOPMENT

The OMEGA laser at the University of Rochester and the National Ignition Facility will need cryogenic targets. We spent considerable effort in support of the ICF labs in understanding and controlling the various solid fuel layering (smoothing) processes (for both D_2 and DT).

5.1. CRYOGENIC LAYERING DEVELOPMENT

The major effort in 97CR/LL1 has been in the implementation of IR heating and joule heating techniques in spherical geometries. These experiments in spherical geometries closely resemble the UR/LLE cryogenic layering system configuration. Experiments are performed using 1 mm o.d. plasma polymer capsules with an attached fill tube inside a 25 mm i.d. layering shroud. In the case of IR heating, the layering shroud is an optical integrating sphere. IR heating produces HD layers smooth to about 2 μm rms with a volumetric heating rate of 200 mW/cm3.

5.1.1. JOULE HEATING AND BETA LAYERING

Joule heating works by generating a heat flux across the ice surface. It is accomplished by applying an electric field to the DT vapor in the center of a shell. This vapor has a small but significant conductivity due to ionization caused by beta decay of tritium in the vapor and the solid. The electric field creates a current which heats the DT gas. We describe here some results of this past year's experiments using a 10 GHz spherical microwave cavity to apply an electric field to frozen DT inside of a 1 mm plastic shell with a fill tube. Previous results using a cylindrical sapphire sample cell have been reported elsewhere [5-1]. The shell and cavity geometry closely mimic that of University of Rochester's cold transfer cryostat's layering shroud.

Our apparatus is very similar to that shown in Ref. 5-2 except the cavity has been replaced as shown in Fig. 5-1 with the surrounding shroud modified to accommodate the new cavity. This cavity is a hollow sphere 25.4 mm in diameter and has a microwave resonance frequency of 10 GHz. It has a Q of 7500 and we have also implemented an adjustable microwave

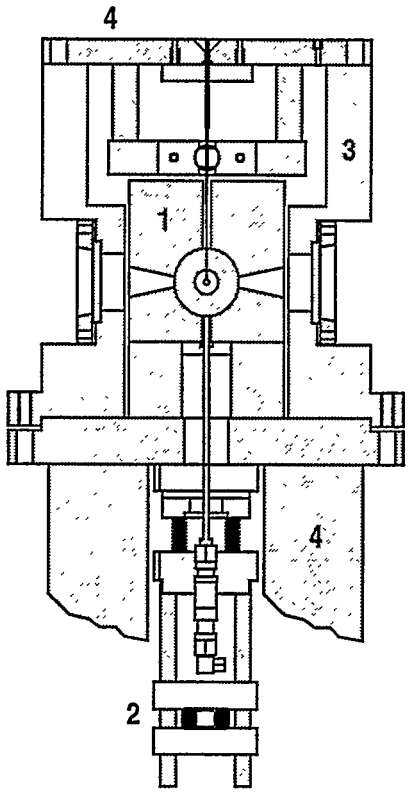

1. Microwave cavity
2. Adjustable microwave coupler
3. Secondary container and thermal shield
4. Links to thermal sinks

Fig. 5-1. The microwave cavity and surrounding vacuum secondary of joule heating experiment.

coupler. This enables us to keep coupling efficiencies high. Our measured power reflected from the cavity is about 1% of the incident power.

Dielectric Loss Measurements in Plasma Polymer Shells. We have been limited in our progress on joule heating by imperfections in our plastic capsules. Our capsule is of the type described in Section 5.1.3. The shell is formed on a mandrel by a bounce coating process. The integral fill tube on the capsule mandrel causes the mandrel to not bounce uniformly over all angles and therefore the capsule tends to be thinner opposite the fill tube. The dielectric loss in our capsule material is not negligible. This means that the microwave field will heat the plastic shell. Since the shell is nonuniform, the heating will be nonuniform as well. The imperfections are enough to create dry spots in the ice as can be seen in Fig. 5-2. To make further progress we will need better shells.

We have measured the dielectric loss coefficient for our capsule. We do this by comparing the known triple point of D_2 with the measured triple point temperature in our apparatus as a function of microwave power. By modeling the thermal conductance between the microwave

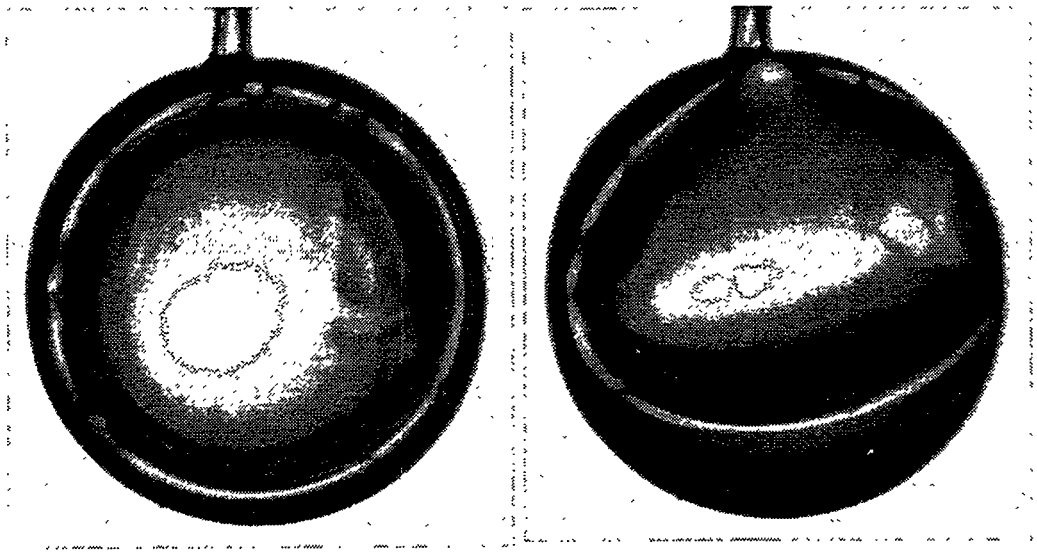

Fig. 5-2. An example of the effects of joule heating with our current plastic shells. We have an initial β layer that is subjected to 52 mW of microwave power for 120 min. The layer moves away from the areas where the plastic is thickest.

cavity wall and the plastic shell we find that for every milliwatt of microwave power applied to the cavity we dissipate 0.8 microwatts of heat in the plastic shell. We expect to layer in this cavity configuration with an input power on the order of 100 mW implying that 80 μW will be dissipated directly into the shell. The power dumped into the ice layer from beta decay is on the order of 13 μW for a 100 μm thick layer in a 1 mm diameter shell. The situation will be less severe with UR/LLE capsules since they are thinner. The current wall thickness is 10 to 15 μm in our sample cells. The Rochester shells are less than 5 μm thick, and should thus dissipate 1/3 to 1/2 as much power.

Beta Layer Roughness as a Function of Cooling Rate. For beta layering, we have discovered a way to make repeatable smooth layers in our spherical geometry. The layer smoothness is dependent upon cooling rate of the DT through the triple point. If we cool slowly we can consistently obtain very good beta layers. In Fig. 5-3 this is illustrated for one particular sample cell at a single fill of DT. There are indications that the required cooling rate may be dependent on the particular sample cell and/or the amount of DT fill in the cell. This is currently being investigated.

For further information, please contact Dr. J. Sater (Schafer Corporation).

5.1.2. IR HEATING SPHERICAL GEOMETRY EXPERIMENTS

Current cryogenic target designs require a uniform cryogenic DT fuel layer. There is also a need for nontritiated cryogenic targets, HD or D_2. However, without the beta-decay heat

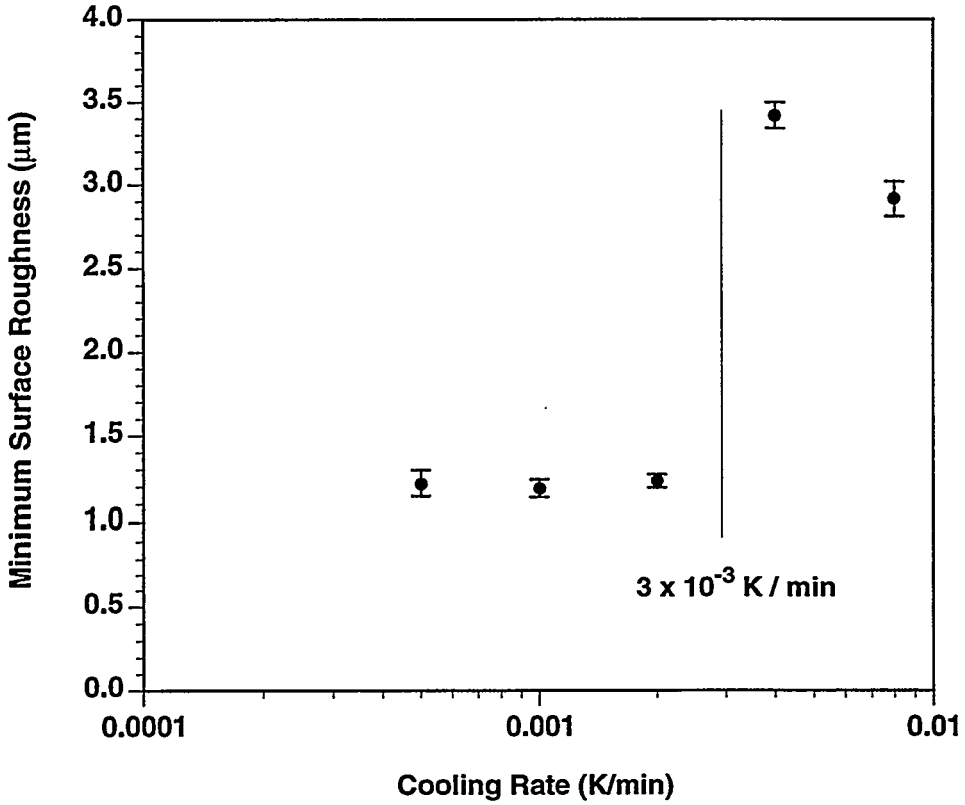

Fig. 5-3. Final layer smoothness as a function of cooling rate through the triple point of DT.

generation no solid redistribution will occur. We are investigating the use of IR radiation to redistribute solid D_2 or HD inside suitable plastic shells by pumping the collision-induced vibration-rotation bands characteristic of the hydrogens. We previously reported proof of principle experiments [5-2,5-3] and surface roughness measurements in a planar geometry [5-4]. This fiscal year's experiments have focused on generating uniform layers inside spherical capsules.

In designing these experiments, several issues need to be addressed. The first issue is the choice of capsule material, CD plasma polymer. The goal is to heat the HD (D_2 or DT) and not the container. Therefore, it is important to minimize the amount of IR absorption (heating) by the capsule wall. CH plasma polymer has strong absorption lines overlapping the hydrogen absorption lines we would be pumping with the IR. Since CD plasma polymer made with deuterated p-Xylene does not have corresponding strong absorption lines in this spectral region, it is the shell material of choice.

A second issue is the technique for generating uniform IR illumination. The surface roughness experiments have shown that diffuse illumination is needed to reduce laser induced coherence effects. The diffuse uniform illumination is achieved by using an integrating sphere as the layering shroud. Calculations show that illumination uniformity to better than 1% can be achieved [5-5]. The integrating sphere used for these experiments is a vacuum tight enclosure

made from aluminum with four window ports and an infragold coating on the inner surface [5-6]. The infragold surface is greater than 96% reflecting at the wavelengths of interest.

Finally, one needs to minimize the effect of the shell fill line. The method developed for attaching the fill line to the shell is discussed in Section 5.1.3. For the IR experiments, the fill line is composed of three sections: a 0.82 mm long CD tube attached to a 5 mm long glass tube which is in turn attached to a stainless steel tube. The stainless tube extends through the integrating sphere wall. To minimize IR absorption in the fill line, the glass tube is gold coated.

Figure 5-4 contains a sketch of the experimental layout. For these experiments a CD shell containing HD is placed in the center of a 25 mm i.d. integrating sphere filled with roughly 0.5 torr of helium exchange gas. An IR laser beam from an F-center laser is injected inside the integrating sphere through a pair of axial window ports. The shell is viewed along an axis orthogonal to the IR injection axis by back lighting the shell and viewing with a CCD camera mounted on a microscope. The integrating sphere is attached to the cold tip of a helium flow cryostat.

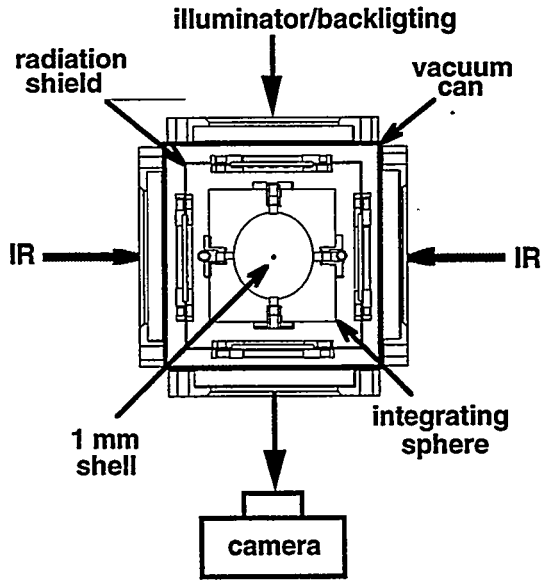

Fig. 5-4. Sketch of the layout for IR heating experiments.

The goal of these experiments is to generate a uniform layer of HD inside a spherical capsule. Initial experiments have used the same techniques as in previous experiments. IR illuminates a shell containing frozen HD. The solid redistributes inside the shell producing an ice layer. Layers generated by this technique are quite rough. Based on the slow freeze results from the joule heating experiments, we have developed a technique for generating smoother layers. In this technique the HD is continually bathed in IR illumination. First, layers are formed by slowly warming frozen HD. Upon observing the disappearance of the last solid remnants [Fig. 5-5(a)], the HD is slowly cooled until solid starts to reform. The temperature is

then held constant as the solid grows, forming a uniform layer [Fig. 5-5(b)]. Figure 5-6 is the power spectrum for the solid layer in Fig. 5-5(b). The layer is approximately 150 μm thick with a resultant rms of 2.24 μm.

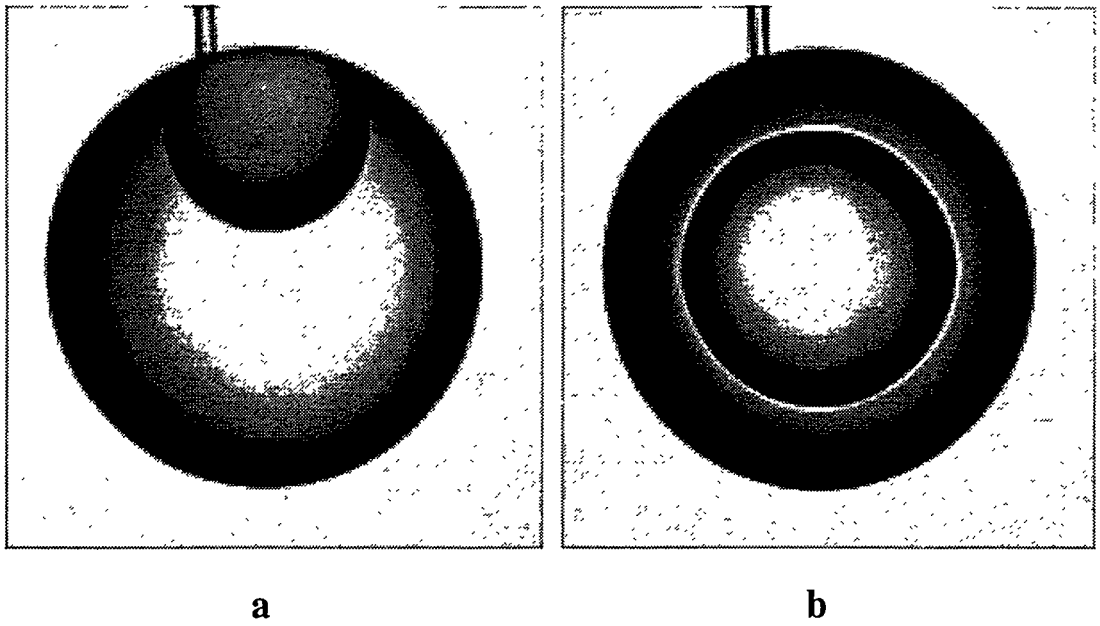

Fig. 5-5. Under constant IR illumination the HD is first (a) warmed to melt the solid, then (b) cooled to form a uniform solid layer.

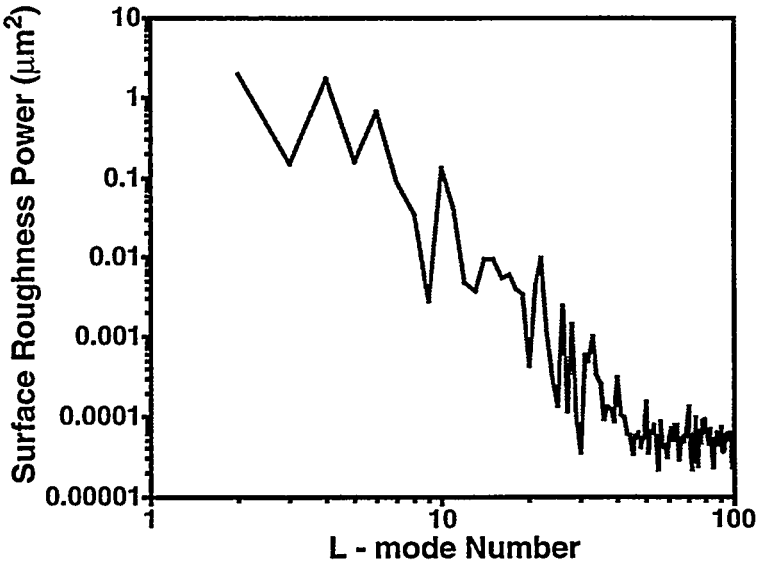

Fig. 5-6. Power spectrum for the solid layer shown in Fig. 5-5. The rms surface roughness is 2.24 μm.

Laser power and temperature stability affect the growth of the solid. Higher quality layers are formed when the temperature can be controlled to within 5 mK under stable laser power.

Large temperature fluctuations cause the HD to melt and freeze too rapidly resulting in rough layers. When both systems are stable, it typically takes about one hour for layer completion.

As can be seen in Fig. 5-5(b), there are features in the layer. A feature seen in all the experiments is a "bump" (or flat spot) near the fill tube. The fill tube has a higher thermal conductivity than the surrounding helium exchange gas. This produces a cold spot at the fill tube/shell junction resulting in a thickening or "bump" in the layer. The only way to remove this feature is to eliminate the fill tube. The second pair of features can be seen at the shell equator. These are due to the IR illumination method. The IR light enters along an axis through the equator of the shell resulting in more intense illumination there than from the rest of the integrating sphere. This causes locally warmer and therefore thinner spots in the layer.

The higher amplitudes at the lower modes shown in Fig. 5-6 are due to these features. They can be removed by alternative injection techniques such as shaping the beam, inserting a beam block in front of the shell, or, perhaps more easily, by initially directing the beam past the shell instead of through it.

For further information, please contact Dr. D. Bittner (Schafer Corporation).

5.1.3. A NOVEL TECHNIQUE TO MAKE PLASTIC CAPSULES WITH SMALL INTEGRAL FILL TUBES

John Burmann, in collaboration with Steve Letts and Mike Saculla (LLNL) has recently developed a technique to make CH shells with small integral fill tubes. The shells are made by the PAMS technique and have been produced in the 1–2 mm size range. The fill tubes have been made as small as 25 μm o.d. with an i.d. of 7 μm. The fill tube and shell are one piece with no glue joint.

Evolution of an idea. Mark Wittman at UR/LLE developed a technique in which a PAMS fiber is solvent welded to a PAMS shell. The shell and fiber are plasma coated with CH and then the mandrel is pyrolized leaving the shell with fill tube. John Burmann initially tried this technique but was unable to produce good results. Steve Letts and Mike Saculla suggested heating a drop of PAMS and drawing fibers by touching a molten drop with a stick. This worked well with lower molecular weight PAMS. John Burmann then came up with the idea of touching a PAMS mandrel onto a small bead of melted PAMS and drawing a fiber that is attached to the bead. After experimenting with different working temperatures and different molecular weight PAMS, this technique proved successful. The composite fiber/mandrel structure is then placed in the GDP coater. The shells produced with this technique have had a very good success. We have leak checked and cryogenically tested the shells successfully and they are currently being used in both the IR and joule heating experiments.

Current recipe. The current layering experiments at LLNL are being done on OMEGA sized targets. Therefore, we started with 1 mm. diameter 100 K molecular weight PAMS shells. These shells are produced for us by GA. 19000 molecular weight PAMS is used to form the fiber. The 19000 PAMS is first crushed into a fine powder and placed on a gold plated microscope slide. Gold is used because PAMS adheres to it better than glass. The slide is placed upon a hot plate that is approximately 150°C which causes the PAMS to melt.

A PAMS mandrel is held with a vacuum chuck and micro-manipulator. The mandrel is brought into contact with one of the small PAMS beads. The mandrel is pulled away, drawing a very small fiber as small as 10 microns in diameter. The fiber is pulled until it breaks naturally. This usually results in a one to 1.5 mm long fiber. Longer fibers are trimmed. An example can be seen in Fig. 5-7a.

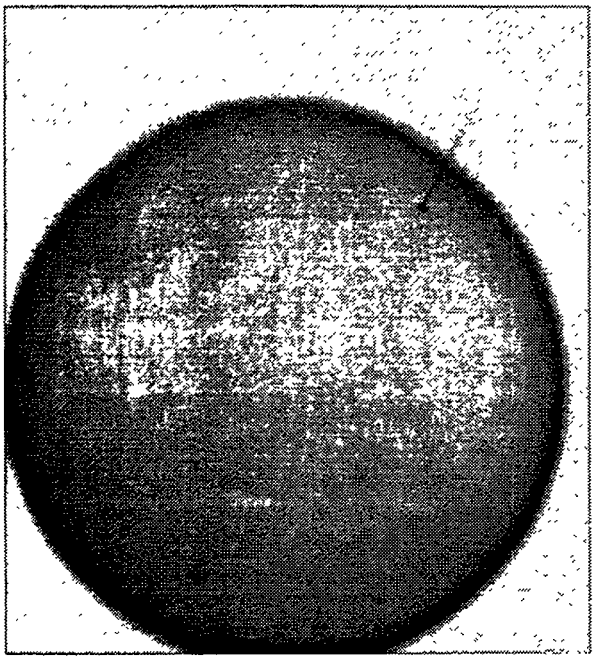

Fig. 5-7a. PAMS shell before being coated with plasma polymer. The shell has a molecular weight of 100,000. The molecular weight of the fiber is 19,000.

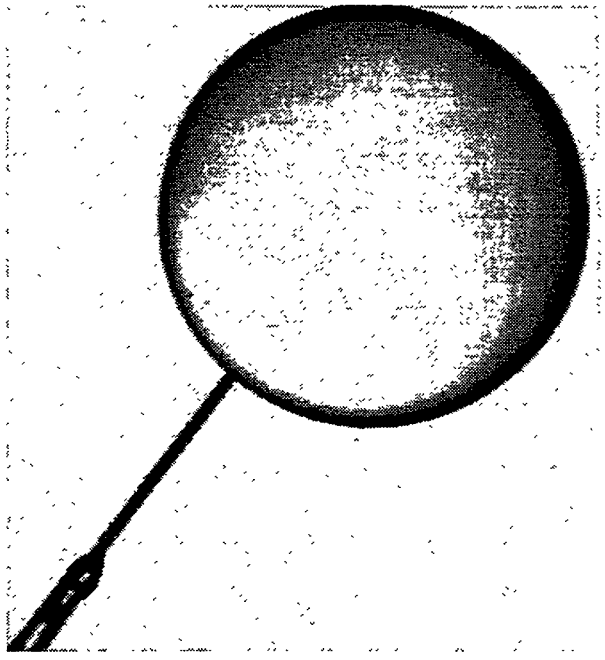

Fig. 5-7b. Completed CD shell. The PAMS has been pyrolized out and the resulting shell mounted on a glass tube. The shell is on the order of 1 mm in diameter and the fill tube30 mm o.d.

A batch of shells are then placed in the GDP bounce coater and 10 μm of CH polymer deposited. Amazingly, the shell and fill tube survive the bounce coating. The presence of the fill tube causes a slight thinning of the CH shell at a point opposite to its attachment. This occurs because the mandrel tends to not bounce on the fill tube. After coating, the end of the fill tube is nipped off and then the shell pyrolized. If we waited until after pyrolisis to trim the tube, the end would be crimped. The shell is then mounted into a longer, thicker glass fill tube with Crest 212 epoxy and tested (Fig. 5-7b).

5.1.4. THERMAL MODELING OF FILL TUBE EFFECTS ON SPHERICAL CAPSULES

Thermal modeling has focused on the problem of a shell suspended on a fill tube in the center of a one inch diameter sphere. This geometry is being used for both IR heating experiments, in which the sphere is used as an integrating sphere for the IR light, and for joule heating experiments, in which the sphere is a microwave resonant cavity.

The initial geometry considered had the shell suspended on a 100 mm glass fill tube. With this setup, the temperature variation on the surface of a uniform 100 μm layer of solid hydrogen would be greater than the temperature drop across the layer. The material would therefore migrate entirely to a location near the fill tube, leaving the bottom of the shell bare. This is due to the fact that the fill tube acts as a cooling fin, projecting from the shell through the relatively cooler helium exchange gas. This cools significantly the hydrogen ice layer at the tube. The cooling effect is evidenced over much of the layer, as is shown below in Fig. 5-8 in which the effect can be seen to be still significant 90° from the fill tube.

The most effective strategy for minimizing this effect proved to be a simple reduction in the heat conduction of the fill tube. This was achieved by using smaller tubes, and by considering fill tubes of materials other than glass. The thermal conductivities of the glass (0.145 W/m*K), shell material (0.06), and hydrogen ice (0.327) are all higher than that of the exchange gas (0.02), and so the heat conduction of both the tube and of the ice inside were important. The temperature deviation along the inner ice surface varied linearly with the thermal conductivity of the tube and ice. Modeling essentially paralleled the search for the smallest possible fill tube, from standard sizes of glass and plastic tube, to drawn down glass tubing, and finally to the construction of a shell with an integrated length of plastic tubing extending 0.5 to 1 mm. The fill tube was 10–15 μm i.d. and ~25 μm o.d. near the shell, and mated to a glass tube extending out of the microwave cavity.

Figure 5-8 shows the temperature variation on the inner ice surface for such a case. The geometry modeled was of the shell and fill tube used for the IR experiments currently underway. The ice layer was fixed at 100 μm thick, and a heating rate of 0.2 mW/mm^3 was assigned in the ice layer inside the shell. The temperature drop across the layer was 2.67 mK, and so the total surface temperature variation was about 13%. The shape of the temperature curve is typical for all cases in which heating occurs only in the shell but not in the fill tube. The curve illustrates a monotonic drop in temperature towards the fill tube and becomes severe within 45° of the tube.

In the case of the electrical (joule) heating experiments, the volumetric heating of the beta decay of DT is a significant source of heat. This heating occurs not only in the shell but also in the DT inside the fill tube. Figure 5-9 shows temperature fluctuations for a one piece shell and tube in three joule heating cases. In the case of heating due to beta decay only, 0.7 mK across

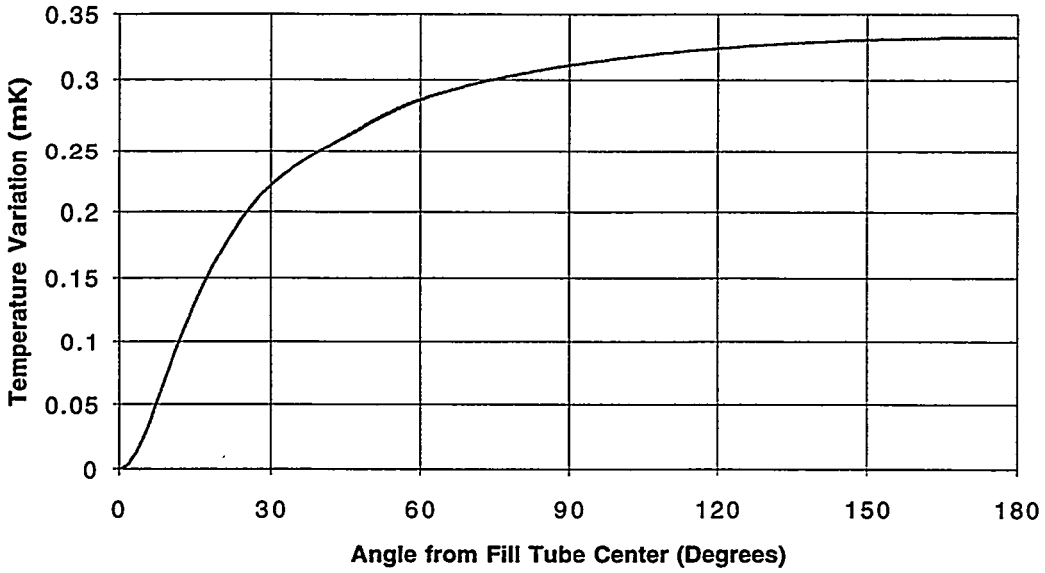

Fig. 5-8 Temperature variations on the surface of a 100 μm ice layer. The total temperature drop is 2.67 mK across the layer, caused by IR heating.

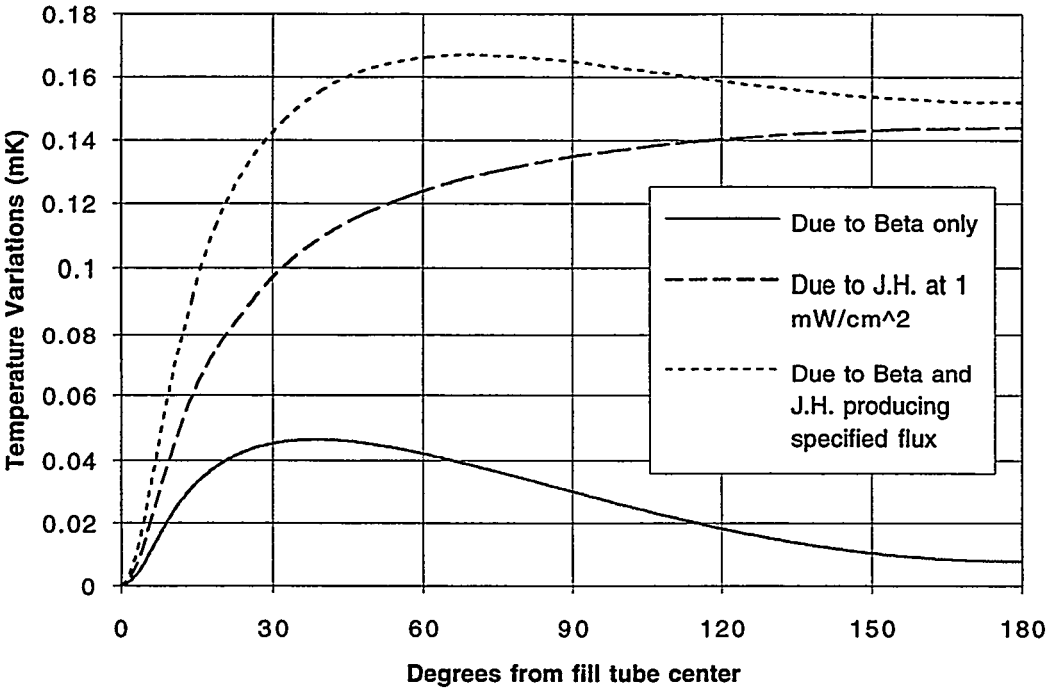

Fig. 5-9. Surface temperature variations for joule heating. Temperature drops of 0.7 mK, 3 mK, and 3.7 mK (respectively) occur across the 100 μm layer.

the 100 μm layer, the temperature on the ice surface has minima both at the fill tube and 180° from the tube. In this case, the heating inside the tube heats the surrounding exchange gas sufficiently to inhibit heat flow radially outward from the shell. The hemisphere of shell near the tube is therefore hotter than the hemisphere away from the tube. The local effect of the

tube, and the fact that there is a port of (higher conductivity) ice through the shell at the tube, cause a sharper local minima at the fill tube. Also shown in Fig. 5-9 is the case in which the RF field heats the DT vapor sufficiently to create a 1 mW/cm^2 flux across the vapor solid interface, but no heating is considered to occur in the solid, either from the RF or from beta decay. Note that this case would not occur, but is an illustrative example. In this case, the drop across the layer would be near 3 mK, and the shape of the temperature variation on the ice surface is similar to the case shown in Fig. 5-8. Finally, the combination of the two heatings is shown. The resulting temperature variations, relative to 3.7 mK across the layer, are quite small (~1%) except within 30° of the fill tube. Since the beta decay heating is fixed, and the rate of joule heating variable, the actual temperature profiles produced could range from the pure beta case, through the combined beta and joule heating case shown, and to cases in which joule heating dominates and the profile is similar to the pure joule heating case shown.

The first of the three cases in Fig. 5-9 above illustrates the difficulty of addressing the fill tube problem by other means. The tube could conceivably be heated somehow, such that the heat flow down the tube produced less of a cooling effect on the ice layer in that region. This also heats the surrounding exchange gas, causing a broad temperature rise of the ice layer. Various heating schemes were considered, including appropriately located point sources, but did not seem promising. At best, the variation could be reduced at locations greater than 30° from the fill tube, as in the third case of Fig. 5-9, but this is at the expense of greater overall variation.

Various other issues relating to this geometry were considered. In the IR experiment, the glass tube (to which the plastic tube/shell is attached) itself terminates inside the 1 in. sphere, joining a larger stainless steel tube. Modeling indicated that stainless tubes projecting 6 mm into the sphere produced temperature variations not significantly worse than 4 mm would, but better than would stainless tubes 8 mm long. Also, as is shown in Fig. 5-10, the displacement of the shell along the fill tube axis produces no significant worsening of the surface temperatures. The displacement of the shell 1 mm lower in the sphere actually compensates some what for the fill tube effect. The temperatures in Fig. 5-10 are plotted above the mean temperature at the ice/shell interface, and so the variations shown are about 10% of the ~2.65 mK temperature drop across the layer.

5.1.5 RAY TRACING RESULTS FOR A 100 μm ICE LAYER IN A 1 mm SPHERE.

Modeling has been performed to understand the ring patterns we see when we take pictures of layered capsules. The images of the shell in IR heating experiments show a bright ring in the shadowed region of the shell. It seemed likely that the bright ring was a result of light striking the solid/vapor interface. Raytracing of a shell with 100 μm ice layer produced intensity maps similar to the images collected from the experiment. Examination of ray histories revealed that a bright band was indeed produced by rays experiencing total internal

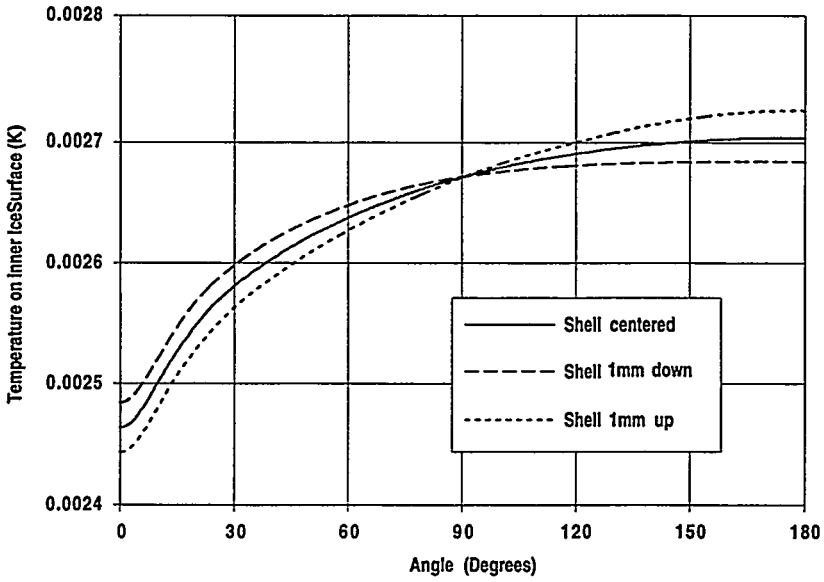

Fig. 5-10. Surface temperature profiles, relative to shell temperature, for the shell centered and displaced 1 mm in the 1 in. diameter sphere.

reflection at the solid/vapor interface. Figure 5-11 below shows (in two dimensions) the set of parallel rays which enter the shell, reflect from the solid/vapor interface, and depart at angles which will exit the integrating sphere through the view port. These rays form the bright ring observed on the image plane. Also visible in the figure are rays of lesser intensity resulting from the same source rays, reflected from various other shell and ice surfaces, and not appearing in the image.

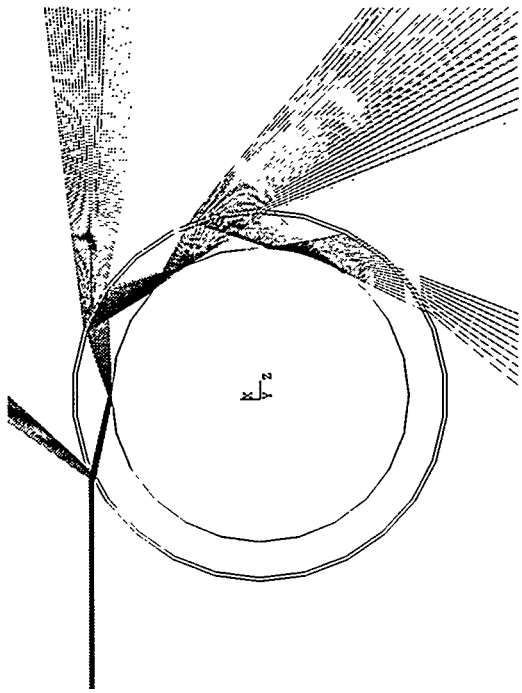

Fig. 5-11. Incoming rays reflected off vapor/solid interface.

In Fig. 5-11, the diverging rays to the right of the figure, if traced back to the image plane through the center of the shell, would converge in an area outside the actual solid/vapor interface due to the magnifying effect of the curved ice and shell layers between the vapor/solid reflections and the imaging optics. The image of the interface (bright ring) has therefore a larger radius than the actual interface. The actual radius of the vapor sphere has been calculated as a function of the apparent radius, and is shown in Fig. 5-12. The calculation was based on the path of the symmetric ray, for which the ray departing from the shell was coplanar with the incident ray. It was assumed for this calculation that the shell had a 0.53 mm outer radius, and was 10 μm thick. The apparent and actual thicknesses are therefore 0.52 mm minus the respective radii. Raytraces of shells with 50 and 150 μm layers of ice have bright rings in the positions predicted by this calculation.

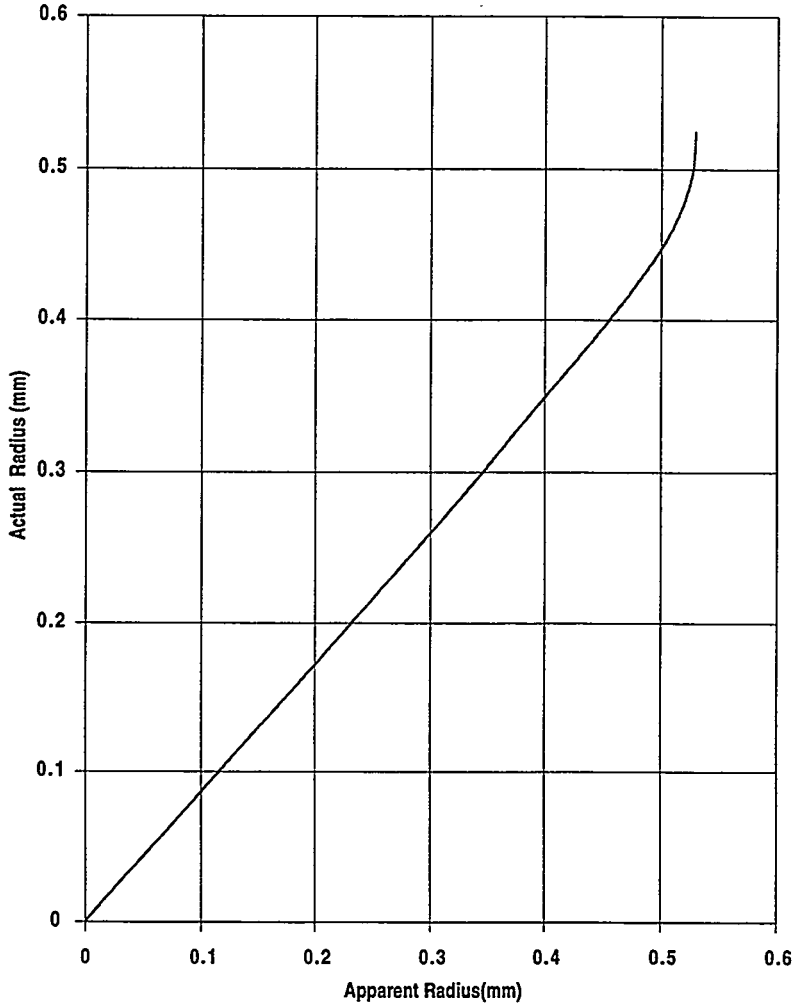

Fig. 5-12. Apparent and actual radii of vapor/solid interface, due to lens effect of shell and ice.

For further information, please contact Dr. J. Sater or Dr. D. Bittner (Schafer Corporation).

5.2. BETA LAYERING SUPPORT AT LANL

Experiments were performed in a 2 mm beryllium lined toroidal cell to examine the surface roughness characteristics of solid DT when layered over a beryllium surface. Several types of experiments were performed to examine the effects of (1) freeze/thaw cycling, (2) slow freeze process, and (3) tritium fraction on the surface roughness of the resulting solid DT layer.

5.2.1. DT SOLID LAYER EXPERIMENTS IN A 2 mm BERYLLIUM TORUS

Experiments were performed in a 2 mm beryllium lined toroidal cell, to examine the surface roughness characteristics of solid DT when layered over a beryllium surface. Several different types of experiments were performed to investigate process stochastics, effects of sudden temperature changes, and the effects of a slow freeze process on the final DT surface roughness.

Figure 5-13 is a graph showing one of the freeze/thaw cycling experiments at an equilibration temperature of 19 K. The graph shows the RMS surface roughness for each of 11 freeze/thaw equilibration cycles, for both raw and normalized data. The normalized data is shown as the lower plots for each cycle. It is determined by dividing the raw RMS roughness by the layer thickness at each point, then multiplying by 80 to get an 80 μm normalized value. For this experiment, the average RMS surface roughness (normalized) is very close to 1 μm. This is essentially the same average roughness that we have observed in a 2 mm copper torus.

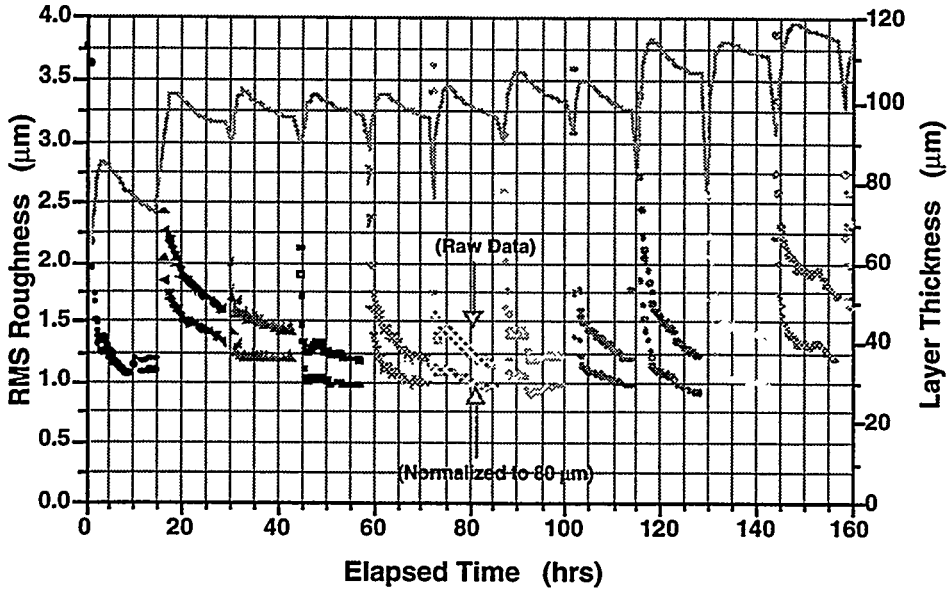

Fig. 5-13. Eleven freeze/thaw cycling experiments performed in a 2 mm beryllium toroidal cell. The solid layer was equilibrated at 19 K and each cycle ran approximately 12 h. The line near the top of the graph shows the evolution of solid layer thickness as the experiment progresses. The surface roughness data shown in the lower half of the graph includes the raw data and data that has been normalized to an80 μm layer thickness.

A number of experiments were performed to examine the effects of sudden temperature changes on the DT solid layer - both temperature increasing and decreasing. Figure 5-14 is a graph of one cycle of a freeze/thaw cycling experiment in which temperature stepping was performed after each equilibration. This is cycle number 9, so that the elapsed time shows the time after the completion of cycles 1–8. This graph is typical of what was observed for each of the sudden temperature transition experiments — that no apparent damage was done to the layer and that in most cases the layer became smoother. The initial equilibration at 19 K shows the kind of rougher layer that was observed with the slow freeze experiments. In cases where the initial equilibration was smoother than that shown here, the smoothing effect of temperature changes was not nearly as dramatic.

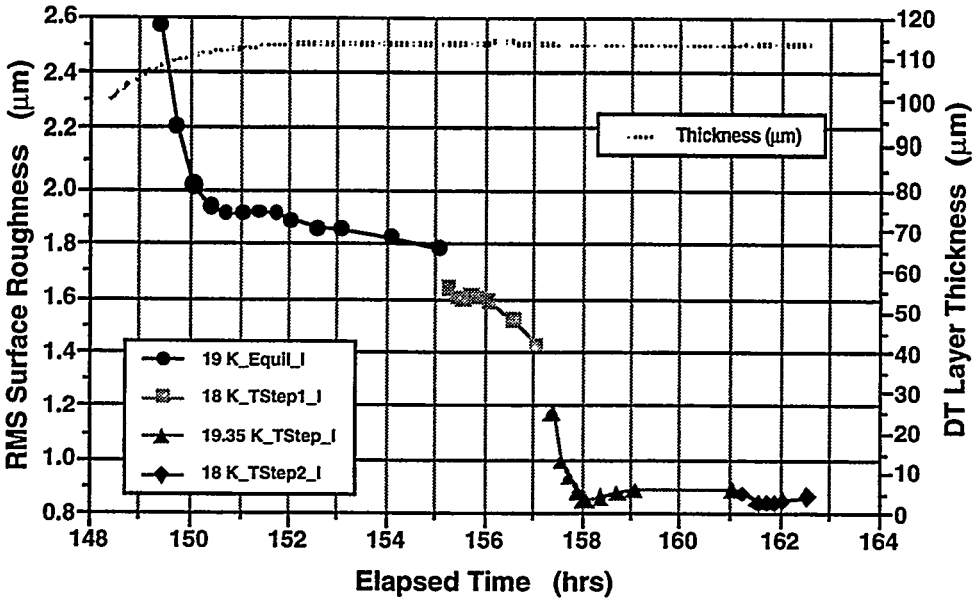

Fig. 5-14. This graph shows the effect of sudden temperature increases and decreases on the DT solid layer in toroidal geometry. This was the 9th cycle of a freeze/thaw cycling experiment of 12 cycles that had begun 150 h earlier. The layer was first equilibrated at 19 K for 6 h, after initial slow freezing at 3.3 mK/min. The temperature was then decreased to 18 K for 2 h, increased to 19.35 K for 4 h, and finally decreased to 18 K again for about 2 h.

A final experiment performed in the 2 mm beryllium torus studied the effect of slow initial freezing. The temperature was stepped through the DT triple point at about 3.3 mK/min. The resulting DT solid layer equilibrated with a solid surface that was an average of 4 to 5 times rougher than that for a normal freeze experiment.

5.2.2. TRITIUM FRACTION EXPERIMENTS IN THE 2 mm BERYLLIUM TORUS

In the second series of experiments performed in FY97, the tritium fraction was progressively reduced from 99% to 40% (further experiments will be performed at 30%, 20%,

and possibly 10% tritium fraction). These experiments were performed to examine the effect of tritium fraction on the surface roughness of the resulting solid layer.

Figure 5-15 shows the resulting smoothing rate for two of these tritium fraction experiments. This graph shows that the solid layer smoothing rate for 99% tritium is about 3 times faster than that for 40% tritium. The rate for 99% tritium is somewhat slower than that previously observed for the P1 mode only ($\tau \approx 15$ min). This is due to the fact that in the present experiments, all modes up to about $l = 100$ are measured. Also the presence of the toroidal waist may slow down the equilibrium between the volumes on each end of the cell.

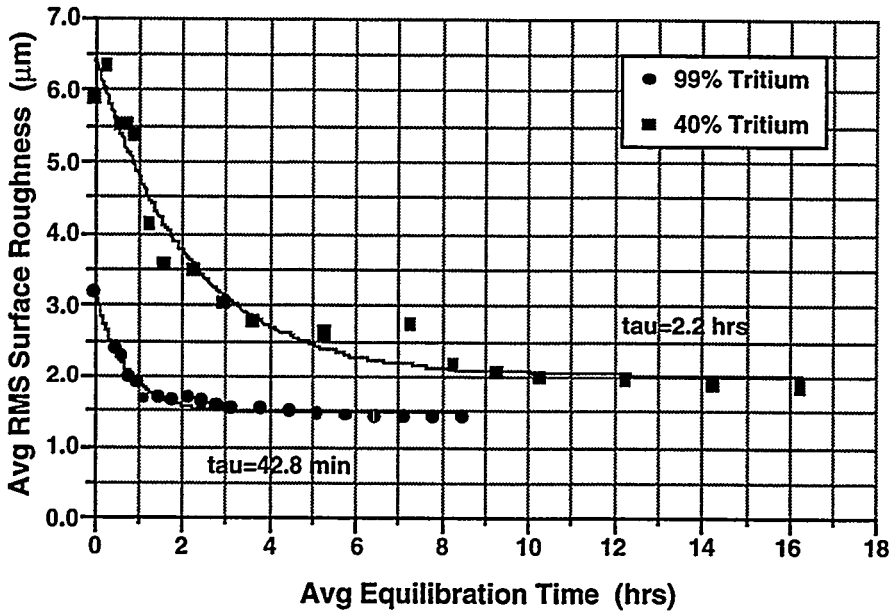

Fig. 5-15 Smoothing rates are shown for DT solid layers equilibrated inside a 2 mm beryllium torus at 0.4 K below the triple point for 99% and 40% tritium. Each data point is the average of the solid surface roughness from 8 to 12 freeze/thaw cycling experiments. RMS value includes l - modes up to 100, so that the time constant differs from the value of 15 min that has previously been measured for mode P1 only.

To date, eight different tritium fractions have been studied. Each experiment was performed at 0.4 K below the mixture triple point. Figure 5-16 shows that there is no significant additional improvement in solid layer smoothness for tritium fractions above 0.5. Below 0.5, the DT solid roughens approximately as predicted by Bernat [5-7]. Additional experiments at still lower tritium fractions will be performed to allow further comparisons with the theory.

For further information, please contact J. Sheliak (GA).

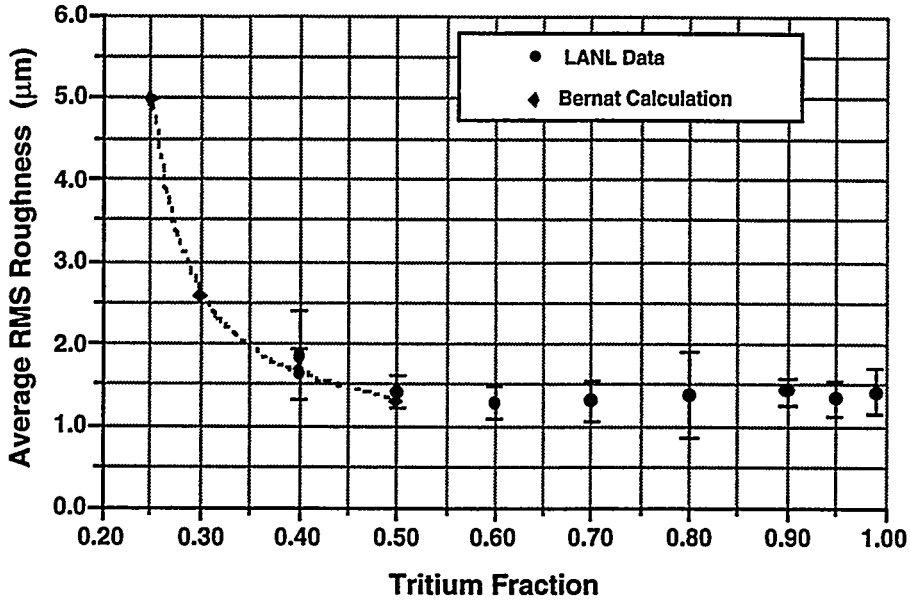

Fig. 5-16. Solid surface roughness is shown as a function of tritium fraction in a DT mixture. The dotted line traces the expected value of DT solid surface roughness for tritium fractions of 0.10 to 0.50, calculated by T. Bernat of LLNL. Each experimental data point is the average of values measured from 8-12 freeze/thaw cyclings.

5.3. REFERENCES FOR SECTION 5

[5-1] E.R. Mapoles, J. Sater, J. Pipes, and E. Monsler, "Smoothing of Deuterium-tritium Ice by Electrical Heating of the Saturated vapor," Phys. Rev. E **55**, 3473 (1997).

[5-2] General Atomics Inertial Confinement Fusion Annual Report, (GA-A22305, UC-712, 1995), p. 5-9.

[5-3] G.W. Collins *et al.*, "Infra-red redistribution of D_2 and HD layers for inertial confinement fusion," J. Vac. Sci. Technol. A **14**, 2897 (1996).

[5-4] General Atomics Inertial Confinement Fusion Annual Report, (GA-A22549, UC-712, 1996), p. 5-10.

[5-5] R.B. Stephens and G. Collins, "Analysis of Integrating Sphere Performance for IR Enhanced DT Layering," Fusion Technol. **31**, 485 (1997).

[5-6] Infragold is an electrochemically plated, diffuse, gold-metallic coating. For information contact Labsphere, North Sutton, NH 03260.

[5-7] T. Bernat, "The Limits to the Smoothness of Solid Hydrogen-Isotope Surfaces," in *Proceedings of the 11th Target Fabrication Specialists' Meeting*, Orcas Island, Washington, September 8-12, 1996.

6. OMEGA TARGET SYSTEM ENGINEERING

During the past year, significant progress was made in the design of the OMEGA Cryogenic Target System (OCTS). In February 1996 a decision had been made to locate the Transfer Station from under "La Cave" to Room 157 and place it into the same glove box as the Fill Station using the Moving Cryostats to transfer individual targets from Room-157 to La Cave. At that time there were still three separate cryostats: the Permeation Cryostat, the Cold Transfer Cryostat, and the Transfer Station, all housed in the same glove box. This system was greatly simplified in 1997 by combining the functions of these three units into one unit: the Fill/Transfer Station. This results in less equipment, fewer operational steps and less floor space required. A disadvantage with this combined design, a higher probability of a tritium release to the room, is mitigated by never docking a Moving Cryostat when targets are being filled.

Great progress was also made toward completing the Cryogenic Target Positioning System (CTPS) design. This system consists of four subunits: the Moving Cryostat, the Moving Cryostat Transfer Cart, the Lower Pylon, and the Upper Pylon. The preliminary design phase was completed, and preliminary design reviews were held for the four major subsystems. Final design work is nearly complete.

A significant amount of effort was spent on thermal analyses of the final design of the MC, both for steady state and transient conditions. This effort was strongly supported by Ido Anteby from UR/LLE. Extensive effort was devoted to minimizing the size of the MCTC. The volume envelope of the final design is now approximately a 5 ft cube with an estimated weight of about 4000 lb. as compared to an earlier version that was 10 ft long.

A detailed Lower Pylon design was developed, including the "drawbridge" area that positions the MC for the characterization process. However, UR/LLE decided that initial characterization will take place in the target fill room and no further work was done on the LP.

The Upper Pylon design was developed, and then significantly revised to reduce capital cost.

The integrated control system design progressed from the conceptual design phase to the preliminary design phase. During that time, a control system architecture was developed and the functions and requirements of these control system hardware components were developed. The Balance of Plant (electrical supply, process air, process water, cooling water) defining the

utilities required for the OCTS was completed. A control system Preliminary Design Review was held at Rochester to review the control system hardware, software, and Hard-Wire Protection System (HWPS).

Because of the high cost of an integrated control system and UR/LLE's requirements for integrated control, they decided to take the lead in designing, fabricating, installing, and testing the control system. GA is assisting UR/LLE during this design phase on an as-needed basis.

The Characterization System of the OCTS is expected to provide information regarding the quality of the cryogenic layer (including the thickness of the layer, its uniformity, and surface finish) to allow shot control to determine if a target is suitable for a laser fusion experiment.

Work began this year on designing the Cryogenic Target Characterization System (CTCS) based on UR's design of a convergent beam interferometer. The CTCS is composed of three systems plus the optical tables. A layout of the CTCS was completed this year and provided to the University of Rochester. UR/LLE has now taken over the final design of the CTCS.

Last year we demonstrated the feasibility of high pressure filling, cooling, and transporting of cryogenic polymer targets with the UR/LLE C-mount in the prototype fill equipment. In FY97, prototype equipment and target filling operations were directed at filling of shells with even thinner walls. Successful demonstration fills and cryogenic verification with wall thicknesses as low as 3.3 mm were accomplished.

During FY97, LANL, in addition to providing design support on issues related to tritium handling, took on responsibility for the design of the OCTS glove boxes, vacuum systems, and tritium removal systems. A preliminary design for two glove boxes was developed, specifications were written, and a contract for construction of the glove boxes was placed in September 1997. The design for the vacuum systems for the OCTS was completed in FY97 and orders for the major vacuum system components was initiated.

6.1. EQUIPMENT TESTING

Last year, the prototype fill equipment was used to demonstrate the feasibility of high pressure filling, cooling, and transporting of cryogenic polymer targets with the UR/LLE C-mount design. In FY97, prototype equipment and target filling operations were directed at filling of shells with even thinner walls. While the equipment was designed to operate with wall thicknesses down to 5 mm, successful demonstration fills and cryogenic verification with wall thicknesses as low as 3.3 mm were accomplished. Equipment component tests were also conducted to support the design of the OMEGA Cryogenic Target System.

6.1.1. D_2 EQUIPMENT TESTING — THIN SHELLS

A summary of the target fill experience with the prototype equipment is provided in Table 6-1. The table shows the number of shells attempted and the percent successful. Nearly 100% success was obtained with wall thicknesses within the design basis of the equipment (≥ 5 μm). As wall thicknesses drop to 3–4 μm, the success rate drops to approximately 50%. None of the four 2.1 μm wall thickness shells that were attempted were successfully filled. (The 2.1 μm wall thickness shells were pressurized to 1100 atm over a time period of 70 hours with a maximum step size of 5 psi, and cooled to 19K over a time period of about 60 hours.)

TABLE 6-1
RECENT TARGET FILL EFFORT WAS DIRECTED AT FILLING OF THINNER WALL SHELLS
(Fill pressure — 1100 atm at room temperature)

Parameter	9-10 μm Wall	5.1 μm Wall	4.3 μm Wall	3.3 μm Wall	2.1 μm Wall
Number of Shells Attempted	20	8	4	6	4
Success Rate	95%	100%	50%	67%	0%

After filling, some of the shells were subjected to measurements of the cryogenic burst temperature. This parameter is an indicator of the cryogenic strength of the shells, and is essential to know as a design basis for cryogenic equipment that handles or transports filled shells.

After initial cooling of the shells to below 20K, they were first removed from the permeation cell and observed for the characteristic deuterium meniscus. To measure the cryogenic burst temperature, the shells were placed once again into the permeation cell (with ~ 50 mtorr of He exchange gas) and the cell temperature was raised to a higher value. After waiting at least 10 minutes for temperature equilibration, the cell was opened and the shells were observed for the meniscus. This was repeated until all the shells had failed. The data from this experiment are given in Table 6-2. The data show a consistent trend of higher failure temperatures with increasing wall thickness. The data also show that the 15K design temperature of the DT equipment should be more than adequate.

TABLE 6-2
BURST TEMPERATURE MEASUREMENTS ARE AN INDICATION OF THE SHELL CRYOGENIC STRENGTH

Wall Thickness	10.1 μm	5.1 μm	4.3 μm	3.3 μm
Failure Temperature (K)	49-54.	41-44	39-40	35-41

6.1.2. COMPONENT TESTS FOR OMEGA CRYOGENIC TARGET SYSTEM DESIGN TASKS

In FY97, a large number of component tests were conducted in support of the OCTS design tasks. These included:

Moving Cryostat Inflatable Seal Performance Testing. The Moving Cryostat requires a seal between the low pressure (~50 mtorr) helium exchange gas and the surrounding cart vacuum. This seal is exposed to the cold thermal shroud as it is reinstalled before undocking from the Fill/Transfer Station. A mockup was constructed to conduct representative cryogenic cycling tests of proposed inflatable seals for this task.

Using a 1/8 in. thick neoprene insert, the inflatable seal system survived demonstration tests with up to ten cycles on one seal. These demonstration tests provided a crucial proof-of-principle for the Moving Cryostat inflatable seal design.

Transport Cart Umbilical Spooler Life Cycle Tests. The Moving Cryostat requires connecting cables that must operate within the spooler assembly, providing a large number of conductors for measurement and control purposes that extend 20 ft into the target chamber. The large number of conductors required precludes cables rated for robotics use (because of their very large size). Proposed cables meeting the conductor and size requirements were tested in a single roll mockup of the spooler: The estimated number of cycles for a cable in-service for five years is ~4000. The cables were cycled for well over 4000 cycles with no degradation in the outer sleeve, no change in the resistance, and no shorting to ground. The conclusion from these tests is that the proposed umbilical cable is more than adequate for the design.

The spooler mockup was also used to test the Moving Cryostat stainless steel flex hose because they have the same service as the umbilical cables. These hoses supply helium to the cryocooler and operate at pressures up to 300 psi. A single hose was pressurized to 300 psi and cycled 4200 times. The outer, braided stainless steel sheath showed some deformation at the point of contact with the roller surface, but there were no detectable leaks in the hose. The rollers showed no significant wear.

Moving Cryostat Elevator Rigid Chain Proof Tests. The Moving Cryostat is transported 20 ft up into the target chamber using a rigid chain drive. A concern is crossing the gap created by the isolation valves. A mockup of the Moving Cryostat rigid chain as it crosses the gap (for the gate valve) in the lower pylon was assembled and operated. The system demonstrated crossing a gap of 6 in. with no difficulty.

Fill/Transfer Station Target Manipulator Operational Tests. The Target Manipulator for the Fill/Transfer Station was received and operational testing was performed. The testing included mock-up of the arm and connection and checkout of the control system.

In addition, the Target Manipulator was used to simulate the movement of a target that would take place within the Fill/Transfer Cryostat. The Target Manipulator successfully picked up a C-mounted target, moved it 90 degrees, and placed it in a simulated stalk.

DT Pressurization System Metering Valve Flow Testing. The Tescom metering valve is being considered for use on the DT Pressurization System. Its purpose is to meter DT from the existing UR/LLE cryogenic intensifier into the permeation cell and intensifier. The metering valve very precisely controls the DT flow into the permeation cell at pressurization rates as low as 0.1 atm/minute (~1.5 psi/min) at pressures up to 125 atm..

The valve was characterized for its flow control characteristics with helium using the existing prototype fill station, intensifier, and permeation cell. At pressure drops of approximately 20 atm (300 psi), the valve provided consistent flow control at pressurization rates as low as 0.4 psi/minute. Smooth controllability was exhibited in all cases. The results show that this valve is a good candidate for the OCTS DT pressurization system.

Transport Cart Air Caster System Testing (by UR/LLE). The MCTC is designed to move about with four air casters. The University of Rochester constructed a mockup of this Moving Cryostat Transfer Cart. The mockup was used to demonstrate movement through the LLE facility.

6.2. DT EQUIPMENT DESIGN

GA's task of designing, fabricating, and testing the OMEGA Cryogenic Target System (OCTS) continued in FY97. Task activities included the completion of the preliminary and final design for the Fill/Transfer Station (FTS) and completion of the preliminary design for the CTPS. Final design of the Cryogenic Target Positioning System (CTPS) is well underway.

6.2.1. DT HIGH PRESSURE SYSTEM

The DT High Pressure System's function is to slowly permeation fill the OMEGA targets with DT fuel gas to densities as high as 0.157 g/cm^3 using at most 1.67 g of DT. An overview of the DT High Pressure System (DTHPS) is given in the simplified piping and instrumentation diagram (P&ID) shown in Fig. 6-1. The DTHPS can be broken up into four main sections: the DT input section, the low pressure filling section, the high pressure filling section, and the DT recovery section. All of these items (except the Syringe Pump) will be housed in a glove box to provide for secondary containment of tritium. The targets are filled in the Permeation Cell.

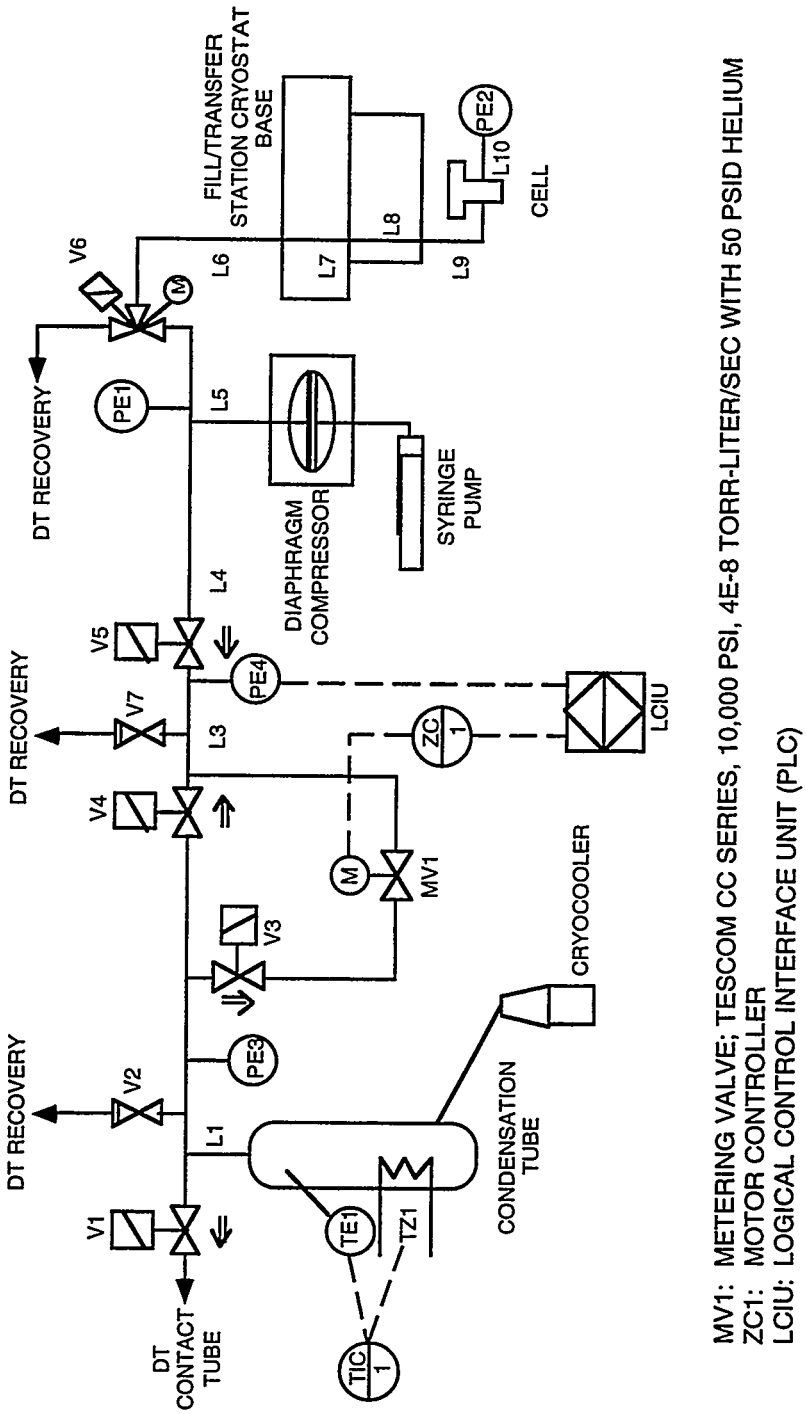

Fig. 6-1. Simplified piping and instrumentation diagram for the DT high pressure system.

The DT input section consists of all of the equipment on the Condensation Tube side of valves V3 and V4. The Condensation Tube, valve V1, and relief valve V2 are already existent as parts of the UR/LLE Tritium Fill Station (TFS). The low pressure filling section consists of all of the equipment in-between valve V3, V4, and V5. The high pressure filling section consists of all of the equipment on the diaphragm compressor side of valve V5. The DT

recovery section is not shown in Fig. 6–1. It consists primarily of piping to connect to the pumps of the UR/LLE Tritium Fill Station.

The target filling process is as follows. The Condensation Tube is filled with liquid DT by condensing DT gas generated out of the uranium beds of the TFS. The tube is isolated by closing V1. The pressure in the tube is raised just above the critical pressure and temperature using the temperature controller TIC1, temperature sensor TE1, heater TZ1, and pressure sensor PE3. Valve V3 is opened to the motor controlled metering valve MV1. The pressure across MV1 (PE3 minus PE4) is controlled by TIC1 to maintain a value of approximately 270 psi. The logical control interface unit (LCIU) controller adjusts the MV1 metering valve to maintain the desired slow pressure ramp rate (as measured on PE4) to the Diaphragm Compressor and Permeation Cell. When the pressure of the Permeation Cell has reached approximately 2000 psi, valve V5 is closed to isolate the high pressure filling section. The Syringe Pump's piston is driven forward at a slow rate. This causes the driven oil to act upon the diaphragms of the compressor to reduce the volume in the compressor from 30 cm^3 to as little as 1 cm^3. This raises the pressure on the targets in the Cell to as much as 22,000 psi. The Cell is then isolated from the compressor by slowly closing the motorized side of valve V6. This will minimize the volume connected to the Cell that is at room temperature when the Cell is cooled to cryogenic temperatures (~20 K) by the Fill/Transfer Station. When the Cell is cold, the excess DT condensed in the Cell, but outside of the targets, is removed by the pumps of the TFS when the pneumatic side of valve V6 is opened.

6.2.2. FILL/TRANSFER STATION

The Fill/Transfer Station's function is to house four targets as they are permeation filled, to cool them to cryogenic temperatures (~20 K), and to transfer them individually to a Moving Cryostat. A sketch of the Fill/Transfer Station is given in Fig. 6-2.

The system has been greatly simplified from the design presented in last year's Annual Report. At that time there were three separate cryostats: the Permeation Cryostat, the Cold Transfer Cryostat, and the Transfer Station. The functions of these three units have been combined into the Fill/Transfer Station. This results in less equipment, fewer operational steps and less floor space required. The major disadvantage with this combined design is a higher probability of a tritium release to the room. This failure mode is mitigated by never docking a Moving Cryostat when targets are being filled.

The Fill/Transfer Station cryostat is of "bell-jar" design and consists of two distinct parts: a fixed base and a removable dome. The joint between the base and the dome is similar to a cryogenic bayonet fitting. For maintenance of equipment on the inside of the cryostat, the dome is simply unbolted and lifted vertically off the base. The cryostat cooling is provided by the cooling module which is located directly below the cryostat. The cooling module is

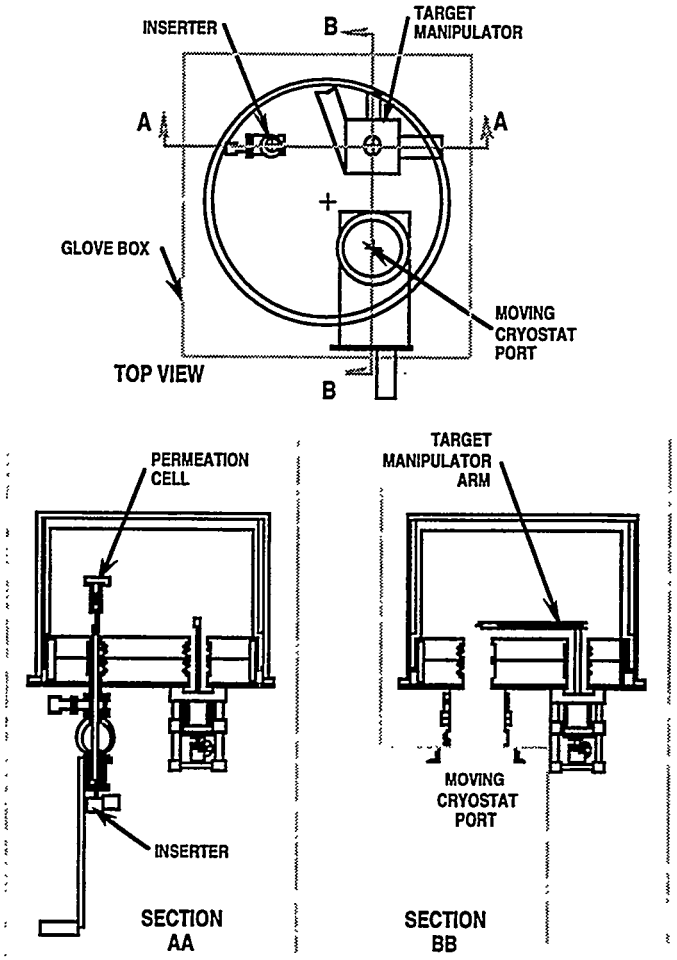

Fig. 6-2. Fill/Transfer Station.

designed around eight closed-cycle cryocoolers grouped into five independent helium circulation loops.

The permeation cell, located inside the cryostat inner volume, is the device in which the targets are permeation filled. During target fill, the permeation cell is warm to allow the DT to permeate through the plastic target wall. Once the DT High Pressure Station reaches the desired pressure, the permeation cell is cooled to approximately 20 K to trap the solid DT inside the target.

Additional equipment, located both inside and underneath the cryostat, are designed to perform various tasks required to fill and transfer targets. The inserter and target manipulator are vacuum manipulators which consist of precision motion stages and bellows feedthroughs. The inserter is used to insert the targets into the permeation cell. The target manipulator moves individual targets between the permeation cell and the Moving Cryostat. The shroud cooler is

designed to remotely remove the thermal shroud from the Moving Cryostat, cool it down to approximately 20K, and then replace the shroud.

6.2.3. CRYOGENIC TARGET POSITIONING SYSTEM (CTPS)

During the past year, great progress was made toward completing the CTPS design. The preliminary design phase was completed, and preliminary design reviews were held for the four major subsystems. Final design work is well underway. A summary for each subsystem follows.

Moving Cryostat (MC). Significant effort was expended in resolving conflicting requirements in the MC final design. Much of this work involved additional analyses and testing. The results of these efforts were incorporated into the final design.

Trade-off-studies were performed to see if modification of the length of the MC shroud could reduce the requirements for the shroud puller. A shorter shroud would be lighter, but would have to accelerate faster; the design length was left unchanged.

The fine positioning assembly was redesigned because the manufacturer of the selected stage ceased production of the selected model.

Thermal analyses of the final design were completed for both steady state and transient conditions. A finite element model was developed and used to evaluate various sets of operating conditions, including the mode in which the cryocooler is cycled on and off to suppress vibration during characterization. The analysis indicated that the inflatable seal needed to be actively heated and this function was added to the design. This effort was strongly supported by Ido Anteby of UR/LLE.

An analysis of vibration of the MC's target mount stalk was performed. Various materials and configurations were evaluated to help finalize the design.

Moving Cryostat Transport Cart (MCTC). A final configuration for the MCTC was selected. Extensive effort was devoted to minimizing its size, and the volume envelope of the final design is approximately a 5 ft cube as compared to an earlier version that was 10 ft long. Its estimated weight is about 4000 lb., most of which can be attributed to the vacuum chamber.

Air casters were selected to provide mobility to the MCTC. These commercially available devices float the MCTC on a thin cushion of air from a compressed air supply. The air casters were evaluated in a test at UR/LLE which showed that a device with the size, weight and weight distribution of the MCTC can be easily moved and maneuvered.

The umbilical spooler design was finalized. A design was developed that relies on the MC elevators for actuation. The spooler passively tracks the elevator movement, which simplifies control of the process. Life cycle tests were performed to confirm the umbilical hose and cables' ability to be repeatedly flexed.

A "short lift" MC elevator was integrated into the MCTC. This system can elevate the MC approximately 3 ft, which is sufficient to lift the MC to the required elevation at the Fill/ Transfer Station and the Prep Station. Incorporating this alternate elevator greatly simplified the MCTC alignment requirements for docking at the various process stations.

Lower Pylon (LP). A detailed LP design was developed, including the "drawbridge" area that positions the MC for the Characterization process. A detailed stress analysis was performed for the enclosure that surrounds the drawbridge area. The design for the support structure for the drawbridge and LP was completed. Subsequently, LLE decided that initial characterization will take place in the target fill room. The drawbridge design was documented such that characterization can be implemented at the lower pylon at a later date.

Upper Pylon (UP). The UP design was developed, and then significantly revised to reduce capital cost. As Fig. 6-3 shows, the UP design consists of a linear motor/carriage, a gripper, a motion / vacuum feed through, and support structures.

The linear motor is a large, high velocity unit operating in atmospheric conditions. It provides the force and speed required to remove the MC shroud in the time available.

The gripper is a mechanism that grabs the top of the MC shroud in preparation for removing it from the MC. It operates inside the Target Chamber under high vacuum conditions. The gripper design was developed to be highly compliant when engaging the MC shroud. After the gripper is in position, a stepper motor is activated which screws the gripper components together, securing the attachment to the MC shroud. The gripper is kept in alignment with the MC via a guide tube that extends into the Target Chamber.

The linear motor carriage and the gripper are connected via a shaft with differentially pumped seals. Commercially available seals were identified that could maintain a vacuum seal at the high shaft velocity required in this application.

6.2.4. CONTROL SYSTEM

The integrated control system design progressed from the conceptual design phase to the preliminary design phase. During that time, a control system architecture was developed to incorporate the various OMEGA Cryogenic Target System (OCTS) sub-systems, their programmable logic controllers, control room displays, and interfaces to external UR/LLE sources. The functions and requirements of these control system hardware components were

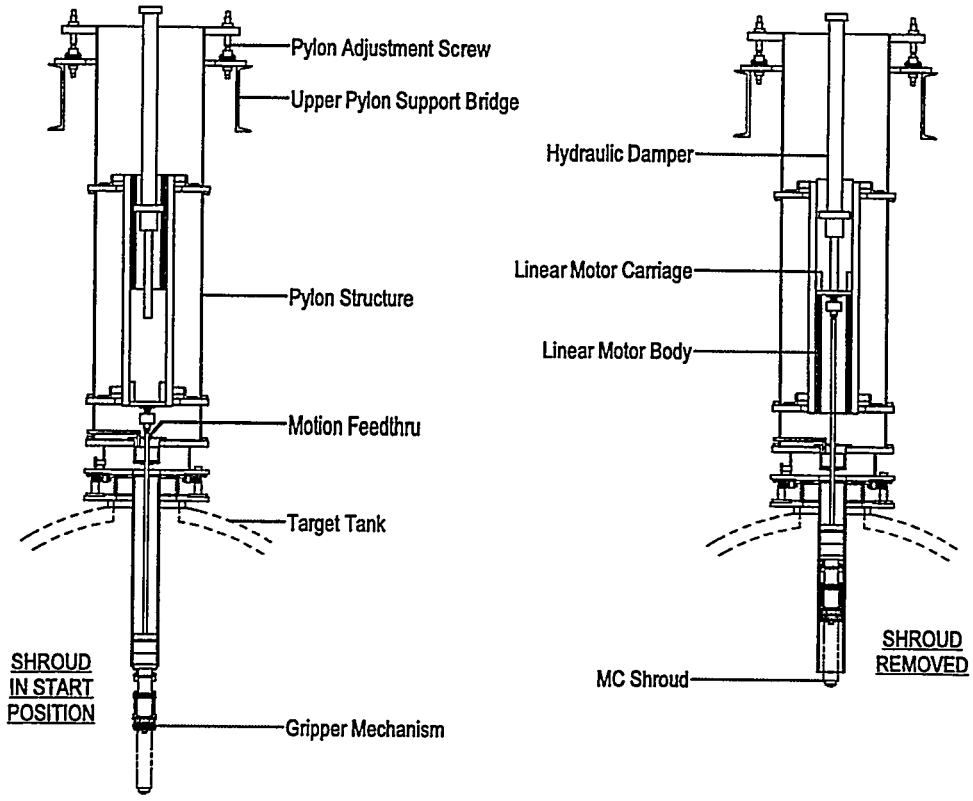

Fig. 6-3. Upper pylon.

developed. A preliminary number of individual input/output channels including the alarms, interlocks, and control loops were determined for control system sizing, response, and data storage. Included in this effort was the definition and development of a Hard-Wire Protection System (HWPS) to enforce safety interlocks and to prevent serious events from occurring. All OCTS sub-systems were tied into the HWPS by means of a logic chain to ensure that the OCTS would not operate without critical systems.

The software scope of the control system was initially defined by the functional flow diagrams. These diagrams defined the step-by-step sequence of operations that the OCTS is to perform. A software architecture diagram was developed to identify the relationship of the software, communication paths, and hardware platforms on which the software operated. The software functions and requirements were based on this diagram.

The Balance of Plant (electrical supply, process air, process water, cooling water) defined the utilities required by the OCTS. Preliminary single line diagrams identifying the electrical supply and equipment users were developed as well as electrical load lists. Finally, a grounding plan along with requirements was developed to assist the overall system design to minimize grounding problems during laser operations.

In April of 1997, a control system Preliminary Design Review was held at Rochester to review the control system hardware, software, and HWPS.

Because of the cost of the integrated control system, various alternate control system concepts were investigated during the summer months. One concept was based on only using small micro-controllers to operate critical loops of the OCTS. Other functions, originally planned to be automatic, were to be manually controlled. This had the attraction of being very cost effective but had obvious limitations. Whereas the integrated control system had much flexibility, data gathering, information exchange with UR/LLE computers, and additional user-defined growth, the limited system only had micro-controllers to perform the critical control loops.

Because of the cost of an integrated control system and UR/LLE's requirements for integrated control, they decided to take the lead in designing, fabricating, installing, and testing the control system. GA is assisting UR/LLE during this design phase on an as-needed basis.

6.2.5. CRYOGENIC TARGET CHARACTERIZATION SYSTEM (SCHAFER CORPORATION)

The characterization system of the OCTS is expected to provide information regarding the quality of the cryogenic layer, including the thickness of the layer, its uniformity, and surface finish, to allow shot control to determine if a target is suitable for a laser fusion experiment.

The University of Rochester has designed a convergent beam interferometer for characterization of the larger millimeter-size targets now required.

Work began this year on designing the Cryogenic Target Characterization System (CTCS). Conceptually, the CTCS is a system using a convergent beam interferometer for collecting quantitative information on the quality of the condensed hydrogen layer inside a spherical capsule (target). Based on the analysis of the CTCS information, a decision will be made as to whether: shoot the target, return it to the layering process, or discard it. A target will be rotated inside the layering shroud while interferometric data is collected. The data from multiple views will be compiled and analyzed to quantitatively determine the quality of the layer.

The Cryogenic Target Characterization System is composed of three systems plus the optical tables which will hold the optical components at the lower pylon windows:

The first system is the convergent beam interferometer. It is defined as the optical train hardware which includes the light source, all the lenses, windows, optical fibers, and associated mounting structures. The interferometer output is an interferometric image (fringe pattern).

The second system is the target alignment system. It will be important to properly align the target in the interferometer through the data collection process and maintain that position as the target is rotated. This requires communication with the Cryogenic Target Positioning System.

The third system is the data collection system. It composes the image capture, phase shifting hardware and software, and minimal data analysis software.

Complete multiple view data analysis will be performed off-line. The plan is to collect the image data and position/rotate the target automatically. One computer captures data, possibly performs some analysis, and provides near term data storage while a second computer controls target alignment and rotation. Communication with the rest of the OCTS is through this second computer.

A layout of the CTCS was completed this year and provided to the University of Rochester. This included CODE V model data files with corresponding optical component layouts and a parts list. The CODE V models were generated to determine optical prescriptions that met the design requirements of the optical system as well as the type, quality, and location of the optical components.

6.2.6. GLOVE BOX (LANL*)

The ability of the OCTS to safely contain tritium is critical to the successful operation of the system. Several major OCTS components will be placed within glove boxes for tritium containment purposes. This year, conceptual and preliminary designs were completed on two OCTS glove boxes. Bid specifications were written for these glove boxes, and bids from qualified vendors were obtained and evaluated. A contract for final design and construction of the glove boxes was placed with Absolute Control Systems of Wheat Ridge, Co.

Figure 6-4 shows the arrangement of the FTS glove box. There are several unique design features of this glove box that are important for operation of the OCTS. The glove box was designed to be capable of structurally supporting the 3700 lb FTS Cryostat. This required careful consideration of the glove box structural aspects to ensure that this load is safely supported. The Moving Cryostat Transfer Cart (MCTC) must move directly under the FTS Cryostat so that the Moving Cryostat (MC) that is contained in the MCTC can pass into the FTS Cryostat. This feature requires that a larger access space be provided under the glove box for the MCTC. Thus, a major support structure on the glove box was designed to allow cantilevering of the glove box over the MCTC.

---

* This work was done by Art Nobile and Joe Nacise of Los Alamos National Laboratory.

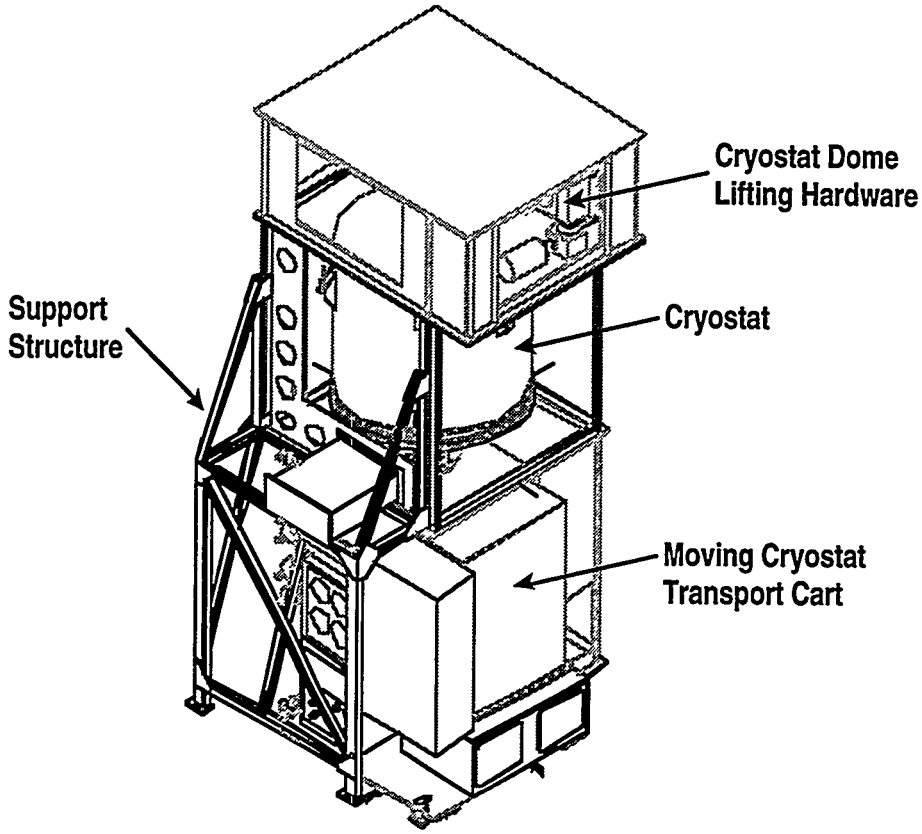

Fig. 6-4. Fill/Transfer Station glove box.

It was important to provide a means to be able to lift the Cryostat Dome to perform maintenance in the interior components of the FTS Cryostat. To accomplish this, lifting hardware was designed into the glove box for lifting of the Cryostat Dome. Lifting of the Cryostat Dome will allow access to Cryostat internal components while working through the glove box gloves. The design of this feature required that the glove box provide structural support all the way to the top of the glove box for the Cryostat Dome

The interfaces between the glove box and the FTS cryostat are critical aspects of the glove box design. In order to transfer the cryogenic target to the MC, the MC is partially moved from the MCTC into the FTS to accept the target. This requires that the MC move across the glove box boundary. To accomplish this, there is a 12 inch gate valve between the cryostat and the glove box. Careful coordination between design personnel at LANL and GA was necessary to assure that the glove box, FTS, and MCTC mechanical interfaces were properly designed. Further careful coordination will be necessary during the construction of the equipment.

Absolute Control Systems has completed preliminary drawings for the FTS Glove box. LANL, GA, and UR/LLE have reviewed these drawings, and comments have been resolved.

Absolute Controls is now proceeding with the final detailed design. When it is complete in March 1998, the glove box will be shipped to UR/LLE for installation into Room 157.

6.2.7. VACUUM SYSTEM (LANL*)

The OCTS will require vacuum for operation of many components of the system. Two vacuum systems will be needed; one for the Room 157 equipment, and one for the La Cave equipment. Two vacuum systems have been designed to provide the necessary vacuum. The vacuum systems will need to handle a wide range of tritium levels, thus the systems have been designed with separate pumping manifolds that allow separation of evacuated gases with different tritium concentrations. Two vacuum manifolds will handle high concentrations of tritium, so these manifolds have been designed with all tritium compatible pumps and vacuum hardware. These manifolds will utilize turbomolecular pumps, Normetex pumps, and Metal Bellows pumps that are compatible with the high concentrations of tritium that will be evacuated with these manifolds.

Several other vacuum manifolds will be necessary for evacuation of components that see only minor levels of tritium. To minimize costs, space, and fabrication expenses these vacuum manifolds were designed with vacuum components that have some elastomeric materials, but will withstand the lower concentrations of tritium.

The Vacuum System Designer II vacuum design code was used to specify the size of the turbomolecular pumps, and perform pumpdown calculations to ensure that the pumpdown times will meet the requirements dictated by cryogenic target production rates for the OCTS.

The preliminary design of the vacuum systems has been completed, and all vacuum system pumps and components have been specified. UR/LLE is in the process of placing orders for the vacuum equipment.

*This work was done by Art Nobile and Joe Nacise of Los Alamos National Laboratory.

7. PUBLICATIONS

Alexander, N., Besenbruch, G., Baugh, W., Beal, C., Boline, K., Brown, L., Egli, W., Follin, J., Gibson, C., Goodin, D., Gram, R., Hansink, M., Hoffman, E., Lee, W., Letzring, S., Mangano, R., McDaniels, J., Nobile, A., Nasise, J., Schultz, K., Stemke, R., Torres, T., "The Cryogenic Target Handling System for the Omega Laser," Paper F1-CN-64/BP-13 in the *Proceedings of the Sixteenth IAEA Fusion Energy Conference*, Montreal, Canada, October 7-11, 1996.

Bernat, D. and Stephens, R., "Algorithm for Better X-Radiography Analyses," Fusion Technol. **31**, 473 (1997).

Boline, Karl, "Testing of a Cryogenic Heat Transfer Joint for Omega," Fusion Technol. **31**, 463 (1997).

Burnham, A.K., Alford, C., Makowiecki, D., Dittrich, T., Wallace, R., Honea, E., King, C., Steinman, D., "Evaluation of B_4C as an Ablator Material for NIF Capsules", Fusion Technol. **31**, 456 (1997).

Gibson, C., Charmin, C., Del Bene, J., Hoffman, E., Besenbruch, G., Anteby, I., "Design of the Fill/Transfer Station Cryostat for the Omega Cryogenic Target System," in the *Proceedings of the Cryogenic Engineering Conference and International Cryogenic Materials Conference,* Portland, Oregon, July 27-August 1, 1997.

Goodin, D. T., *et al.*, "Design of the Omega Cryogenic Target System," in *Proceedings of the 17th IEEE/NPSS Symposium on Fusion Engineering*, San Diego, California, October 6-11, 1997.

Hamilton, K.E., Letts, S.D., Buckley, S., Fearon, E., Wilemski, G., Cook, R., Schroen-Carey, D., "The Role of Reactant Transport in Determining the Properties of NIF Shells Made by Interfacial Polycondensation," Fusion Technol. **31**, 391 (1997).

Hoppe, M.L., Stephens, R.B., and Harding, D., "Characterization of Chemical Dopants in ICF Targets," Fusion Technol. **31**, 504 (1997).

Lambert, S.M., Overturf III, G.E., Wilemski, G., Letts, S.A., Schroen-Carey, D., Cook, R.C., "Fabrication of Low-Density Foam Shells from Resorcinol-Formaldehyde Aerogel," Journal of Applied Polymer Sciences **65**, 2111-2122, 1997.

McQuillan, B.W., Nikroo, A., Steinman, D., Elsner, F., Czechowicz, D., Hoppe, M., Sixtus, M., and Miller, W., "The PAMS/GDP Process for Production of ICF Target Materials," Fusion Technol. **31**, 381 (1997).

Mapoles, E.R., Sater, J., Pipes, J., and Monsler, E., "Smoothing of Deuterium-Tritium Ice by Electrical Heating of the Saturated Vapor," Phys. Rev. E **55**, 473 (1997).

Nikroo, A., "Deposition and Characteristics of Chlorine-Doped Glow Discharge Polymer Films," Fusion Technol. **31**, 431 (1997).

Schultz, K., Kaae, J., Miller, W., Steinman, D., Stephens, R., "Status of Inertial Fusion Target Fabrication in the USA," in *Proceedings of the IAEA Technical Committee Meeting on Drivers and Ignition Facilities for Inertial Fusion* , Osaka, Japan, March 13-14, 1997.

Shih, W.S., James, W., Barr, N., Morosoff, N., Xie, Y., and Stephens, R., "Properties of Beryllium Loaded Plastic Films," Fusion Technol. **31**, 442 (1997).

Stephens, R.B. and Collins, G., "Analysis of Integrating Sphere Performance for IR Enhanced DT Layering," Fusion Technol. **31**, 485 (1997).

Stephens, R.B, McQuillan, B.M.in *Proceedings of the 17th IEEE/NPSS Symposium on Fusion Engineering*, San Diego, California, October 6-11, 1997.